UNIVERSITY OF QUEBEC AT CHICOUTIMI

A DISSERTATION PRESENTED TO THE UNIVERSITY OF

QUEBEC AT CHICOUTIMI IN PARTIAL FULFILLMENT

OF THE REQUIREMENTS FOR THE DOCTOR

OF PHILOSOPHY IN ENGINEERING

BY

KUN LIU

SOLIDIFICATION OF IRON-RICH INTERMETALLIC PHASES

AND THEIR EFFECTS ON TENSILE PROPERTIES

IN AL-CU 206 CAST ALLOYS

September 2012

Abstract

The Al-Cu 206 cast alloys have been widely used in automotive and aerospace industries due to the high strength and good elevated temperature properties. However, this family alloys have an extremely low upper limit for the iron content (usually less than 0.15 wt. %) because the presence of more Fe can cause a great loss of the mechanical properties, particularly the ductility. With the increasing use of the recycled aluminum alloys, the requirement for extremely low iron contents has become a main concern in terms of the manufacturing technique and cost. Therefore, manufacturing premium castings with higher iron contents has become a great challenge.

In this study, the solidification behavior of the iron-rich intermetallics and the effect of alloy composition, cooling rate and solution heat treatment on the iron-rich intermetallics were systematically investigated in 206 cast alloys at 0.15, 0.3 and 0.5 wt. % Fe. The effect of the iron-rich intermetallics on the tensile properties was also evaluated. An optical microscope, a scanning electron microscope and a transmission electron microscope were used to observe the microstructures and analyze the volume fraction of the iron-rich intermetallics as well as the fracture surface. The solidification sequences of 206 cast alloys at 0.15~0.5 wt. % Fe were well established. The experimental results in the present thesis are divided into four parts.

In the first part, the iron-rich intermetallics in 206 cast alloys at 0.15 wt. % Fe were studied. It was found that Chinese script α-Fe and platelet-like β-Fe can precipitate and coexist in the finally solidified alloy and the individual addition of either Mn or Si promotes the formation of α-Fe and hinders the occurrence of β-Fe. The critical cooling rate to effectively suppress the formation of β-Fe depends on the alloy composition. A casting process map is established to correlate the Mn and Si contents with cooling rate for the 206 cast alloys.

In the second part, the iron-rich intermetallics in 206 cast alloys at 0.3 wt. % Fe were investigated. Platelet β-Fe and Chinese script α-Fe were observed in the solidified samples. Both the α-Fe and β-Fe phases can nucleate on the oxide films. In addition, α-Fe can also nucleate on $Al_6(FeMnCu)$ and Al_3Ti particles while the earlier formed α-Fe phase can also nucleate the later formed β-Fe phase. In addition, Either Si or Mn favors the transformation of β-Fe into the α-Fe phase. At a combination of both high Mn and high Si, almost all β-Fe platelets can be converted into Chinese script α-Fe. For a cast Al-4.5Cu-0.3Fe alloy, 0.3% Mn and 0.3% Si are required to completely suppress the β-Fe phase.

In the third part, the iron-rich intermetallics in 206 cast alloys at 0.5 wt. % Fe were studied. In addition to the two typical platelet β-Fe and Chinese script α-Fe phases, two

extra phases, i.e. Chinese script $Al_m(FeMn)$ and platelet $Al_3(FeMn)$ were experimentally observed in the solidified alloys for the first time in the 206 cast alloys. $Al_m(FeMn)$, α-Fe and $Al_3(FeMn)$ are all possible as dominant iron-rich intermetallic phases. The individual addition of Si favors the formation of α-Fe but inhibits the precipitation of β-Fe while the individual addition of high Mn promotes the formation of $Al_3(FeMn)$. The combined addition of both Si and Mn enhances the formation of predominate α-Fe. Furthermore, the formation temperature of each iron-rich intermetallic phase decreases and the stable iron-rich intermetallic is gradually replaced by the metastable phase with increasing cooling rate. There exists a threshold cooling rate to obtain the predominant Chinese script $Al_m(FeMn)$ or α-Fe phases.

Finally, the effect of iron-rich intermetallics on the tensile properties of the 206 cast alloys was performed. It was found that the tensile strengths linearly decrease with increasing iron content but higher strength are obtained for the alloys with dominant Chinese script iron-rich intermetallics than those with dominant platelet ones at similar iron levels. The 206 alloys above an iron level of 0.15% are hard to meet the minimum ductility (7%) in artificial overaging treatment (T7). However, the iron content limitation can be extended to 0.3%, or even to 0.5% to meet the 7% elongation in natural aging treatment (T4) condition under well controlled Mn and Si contents, providing the great potential to cast premium 206 alloys at high iron levels.

Résumé

L'alliage Al-Cu 206 est largement utilisé dans les industries automobile et aéronautique en raison de sa grande résistance et de ses bonnes propriétés à température élevée. Toutefois, ce type d'alliage possède une faible teneur en fer (généralement une fraction massique inférieure à 0,15%), car la présence davantage de fer peut causer une diminution considérable des propriétés mécaniques. Avec l'utilisation de plus en plus croissante des alliages d'aluminium recyclé, l'exigence pour une teneur très basse en fer est devenue une préoccupation majeure en termes de technique de fabrication et de coût. Par conséquent, la fabrication de pièces de haute gamme avec une teneur élevée de fer est un très grand défi.

Dans cette étude, le comportement des composés intermétalliques riches en fer au cours de la solidification et les effets de la composition de l'alliage, de la vitesse de refroidissement et de la mise en solution sur les phases intermétalliques riches en fer dans l'alliage 206 coulé à différentes teneurs massique de fer : 0,15, 0,3 et 0,5% a été étudié. L'effet des composés intermétalliques riches en fer sur les propriétés de traction a également été étudié. Un microscope optique, un microscope électronique à balayage et un microscope électronique à transmission ont été utilisés pour observer les microstructures et analyser la fraction volumique des composés intermétalliques riches en fer ainsi que la surface de rupture. Les séquences de solidification de l'alliage 206 coulé à teneur massique en fer comprise entre 0,15 ~ 0,5% ont été mis en place. Les résultats expérimentaux de la présente thèse sont divisés en quatre parties.

Dans la première partie, les phases intermétalliques riches en fer dans l'alliage 206 coulé avec une teneur en fer de 0,15% ont été étudiées. Il a été constaté que la phase α-Fe à charactère chinois et β-Fe en forme de plaquettes coexistent et peuvent précipiter dans l'alliage solidifié et l'addition individuelle de Mn ou de Si favorise la formation de α-Fe et empêche l'apparition de β-Fe. La vitesse critique de refroidissement pour supprimer efficacement la formation de β-Fe dépend de la composition de l'alliage. Une carfographie du processes de coulée a été établie pour corréler entre la teneur du Mn et du Si avec un taux de refroidissement pour l'alliage 206 coulé.

Dans la deuxième partie, les phases intermétalliques riches en fer dans l'alliage 206 coulé avec une teneur en fer de 0,3% ont été étudiées. Les phases à plaquettes β-Fe et celle à écriture chinoise α-Fe ont été observées dans les échantillons solidifiés. Les deux phases α-Fe et β-Fe peuvent germer sur des films d'oxyde. En outre, α-Fe peut aussi germer sur $Al_6(FeMnCu)$ et sur les particules Al_3Ti, tandis que les phases α-Fe formées plus tôt peuvent également germer sur la phase β-Fe formée plus tard. En plus, ni Si ni Mn ne

iv

favorisent la transformation de la phase β-Fe en celle de α-Fe. À une combinaison du Mn et du Si élevés, presque toutes les plaquettes β-Fe peuvent être converties en phase à caractères chinois α-Fe. Pour une coulée de l'alliage Al-4,5Cu-0,3Fe, 0,3% Mn et 0,3% Si sont requis pour supprimer complètement la phase β-Fe.

Dans la troisième partie, les phases intermétalliques riches en fer dans l'alliage 206 coulé avec une fraction de fer de 0,5% du poids ont été étudiées. En plus des deux phases, celle typiquement à plaquettes β-Fe et celle à écriture chinoise α-Fe, deux phases supplémentaires, c'est-à-dire, à écriture chinoise Alm(FeMn) et à plaquettes Al_3(FeMn) ont été observés expérimentalement dans les alliages solidifiés pour la première fois dans l'alliage 206 coulé. Al_m(FeMn), α-Fe et Al_3(FeMn) sont toutes possibles comme phases intermétalliques riches en fer dominantes. L'addition individuelle de Si favorise la formation de α-Fe mais inhibe la précipitation de β-Fe, tandis que l'ajout individuel d'une grande fraction de Mn favorise la formation de Al_3(FeMn). L'addition combinée de Si et de Mn améliore la formation prédominante de α-Fe. En outre, la température de formation de la phase intermétallique riche en fer diminue et la phase intermétallique riche en fer stable est progressivement remplacée par la phase métastable avec l'augmentation de la vitesse de refroidissement. Il existe un seuil de vitesse de refroidissement pour obtenir une prédominance de la phase à écriture chinoise Al_m(FeMn) ou α-Fe.

Enfin, l'effet des composés intermétalliques riches en fer sur les propriétés de traction de l'alliage 206 coulé a été étudié. Il a été constaté que la résistance ultime à la rupture diminue linéairement avec l'augmentation de la teneur en fer, mais une plus grande résistance à la traction est obtenue pour les alliages contenant des composés intermétalliques à écriture chinoise riches en fer que ceux à dominance de plaquettes à des teneurs similaires de fer. Les alliages 206 à teneur de fer suppérieur à 0,15% traités pas vieillissenent artificiel atteignent difficilement la ductilité minimale (7%) comparés à ceux ayant subi un traitement de type (T7). Cependant, la limitation de la teneur en fer peut être étendue à 0,3%, voire à 0,5% pour répondre à l'allongement de 7% dans le traitement de vieillissement naturel (T4) sous la condition de bien contrôler la teneur en Mn et celle en Si, ce qui fournit un grand potentiel de couler l'alliage 206 à des teneurs de fer élevées.

Acknowledgements

I am deeply indebted to all those people who have helped and supported me throughout the course of this work.

First and foremost, I am extremely grateful to Prof. X. -G. Chen, my university supervisor, for his valuable suggestions and encouragement. It has been a great pleasure to work with him. His originality, experience and contributions in the field of material science have absolutely nourished the value of this thesis. As an extremely busy professor, Prof. Chen has always been available and kind whenever needed. It is my honor to earn my degree under his supervision.

I would greatly acknowledge my co-supervisor, Prof. X. Cao, for his supervision, consistent guidance, constant encouragement, and advice in both science and technology. His deep scientific intuition inspired and helped my growth as a student and a researcher throughout this study.

I also would like to thank Prof. S. Dilip, a member of the doctoral examination and supervision committee, for his valuable comments and suggestions during my seminars.

I gratefully thank Prof. Z. Zhang for the training of SEM and the valuable suggestions for the sample preparation and observations by using SEM and TEM.

I would like to express my thanks to the technicians of Martin Bouchard and Emelie Brideau for their technical support. I have also had many fruitful scientific and technical communications with my colleagues and friends including Jing Lai, Mehand Tebib, Yumei Han, Cangji Shi, Jian Qin, Junfeng Guo, Lei Pan, Peng Shen, Mohammad Shakipa, Emad Elgallad and Ehab Elsharkawy. I thank them for their scientific comments on my project and their encouragements. Special thanks to Monir Baiteche and Mehand Tebib for the support of French language modifications.

Publications

In my Ph. D work, 13 publications in the form of journal articles, conference papers, and posters have been prepared. Full details are provided below.

I. Peer-Reviewed Journal Articles

1. K. Liu, X. Cao, X. -G. Chen, "Solidification of iron-rich intermetallic phases in Al-4.5Cu-0.3Fe cast alloy", Metallurgical and Materials Transaction A, 2011, 42A (7): 2004-2016.

2. K. Liu, X. Cao, X. -G. Chen, "A new iron-rich intermetallic--AlmFe phase formed in Al-4.6Cu-0.5Fe cast alloy", Metallurgical and Materials Transaction A, 2012, 43A (4): 1097-1101.

3. K. Liu, X. Cao, X. -G. Chen, "Precipitation of iron-rich intermetallic phases in Al-4.6Cu-0.5Fe-0.5Mn cast alloy", Journal of Materials Science, 2012, 43 (10): 4290-4298.

4. K. Liu, X. Cao, X. -G. Chen, "Effect of Mn, Si and cooling rate on the formation of iron-rich intermetallics in 206 cast alloys", Metallurgical and Materials Transaction B, 2012, 43B (5): 1231-1240.

5. K. Liu, X. Cao, X. -G. Chen, "Formation and phase selection of iron-rich intermetallics in Al-4.6Cu-0.5Fe cast alloys", Metallurgical and Materials Transaction A, 2012, in press, DOI: 10.1007/s11661-012-1419-7.

6. K. Liu, X. Cao, X. -G. Chen, "Solid transformation of iron-rich intermetallic phases in A206 Al-Cu cast alloy during solution heat treatment", under review, Metallurgical and Materials Transaction A, 2012.

7. K. Liu, X. Cao, X. -G. Chen, "Effect of iron-rich Intermetallics on tensile properties of 206 Al-Cu Cast Alloys", to be submitted to Metallurgical and Materials Transaction A, 2012.

II. Conference Presentations / Proceedings

8. K. Liu, X. Cao, X. -G. Chen, "Effect of Mn and Si on iron-containing intermetallics in cast 206 aluminum alloys", in Conference of Metallurgists 2010, (COM 2010), Vancouver, BC, Canada, October 3–6, 2010, pp.113-120.

9. K. Liu, X. Cao, X. -G. Chen, "Effect of cooling rate on the solidification characteristics of iron-rich intermetallics in 206 Al-Cu cast alloys", TMS 2013, San Antonio, Texas, American, March 3-7, 2013, accepted.

III. Scientific Posters

10. K. Liu, X. Cao, X. -G. Chen, "On the mechanical properties of 206 alloys at high iron contents", The Encyclopaedia of Research on Aluminium in Quebec – 2012 Edition, Les Presses de l'aluminium, in press.

11. K. Liu, X. Cao, X. -G. Chen, "A new iron-rich intermetallic phase -AlmFe formed in 206 type cast alloy with 0.5Fe", The Encyclopaedia of Research on Aluminium in Quebec – 2011 Edition, Les Presses de l'aluminium, p. 43.

11. K. Liu, X. Cao, X. -G. Chen, "The role of oxide films on the nucleation of iron-rich intermetallics in cast 206 alloy", The Encyclopaedia of Research on Aluminium in Quebec – 2010 Edition, Les Presses de l'aluminium, p. 50.

12. K. Liu, X. Cao, X. -G. Chen, "Effect of manganese and silicon on iron intermetallics in 206 foundry alloy", The Encyclopaedia of Research on Aluminium in Quebec – 2009 Edition, Les Presses de l'aluminium, p. 50.

Table of contents

Chapter 8

Conclusions and future work 219

List of figures

List of tables

CHAPTER 1

INTRODUCTION

Chapter 1

Introduction

1.1 Definition of the problems

Precipitation-hardening 206 cast Al-Cu alloys are commonly used as structural castings in heat-treated tempers for automotive, aerospace, and other applications where high strength and moderate elongation are usually required. In addition, they can often be used as cylinder heads for gasoline and diesel motors, turbine and supercharger impellers and other applications where moderate strength but a minimum elongation of 7% are requested [1]. To improve the strength, the 206 Al-Cu cast alloys usually have the solution heat treatment (SHT) to dissolve the Al-Al$_2$Cu eutectic phases into the matrix and then aging to precipitate the strengthening phase θ' or θ. Though the optimal strength can usually be reached at T6 (SHT and artificial peak aging) but with heavy stress corrosion, hence, T4 (SHT and natural aging) or T7 (SHT and artificial over aging) process is often applied to the 206 cast alloys to increase the stress corrosion resistance [2].

Iron has been thought to be one of the most harmful impurities in most of the commercial aluminum alloys. Table 1.1 shows the chemical composition of 206 cast alloys in USA casting alloy specifications. It can be found that the upper limitation of iron is 0.15 %

(206.0) or less than 0.10% (206.2). In the aerospace applications, the iron content is even required below 0.07% (A206.2) [3] (all alloy compositions are in wt. % unless indicated otherwise). However, iron is always present in commercial aluminum alloys. According to Lyakishev [4], the solubility of iron is approximately 1.8 % at 928 K (655 °C) in liquid pure Al but only 0.0052% at 723 K (450 °C) in solid pure Al. Therefore, almost all the iron will precipitate from liquid Al alloys in the form of iron-rich intermetallics which have been thought to be harmful to the mechanical properties, particularly ductility, especially the platelet iron-rich intermetallics. For platelet iron-rich intermetallic phase, it has been thought to be particularly deleterious to the mechanical properties because it is brittle and can act as the stress riser. This platelet phase is usually identified to be Al_5FeSi and can also block the feeding when it is precipitated interdendritically, leading to the formation of shrinkage porosity [5].

Table 1.1 Chemical composition of 206 cast alloys (wt. %) [3]

Alloy	Si	Fe	Cu	Mn	Mg	Ti	Zn	Other	
								Each	Total
A206.0	0.05	0.1	4.2-5.0	0.20-0.50	0.15-0.35	0.15-0.30	0.1	0.05	0.15
A206.2	0.05	0.07	4.2-5.1	0.20-0.51	0.20-0.35	0.15-0.25	0.05	0.05	0.15
206	0.1	0.15	4.2-5.2	0.20-0.52	0.15-0.35	0.15-0.30	0.1	0.05	0.15
206.2	0.1	0.1	4.2-5.3	0.20-0.53	0.20-0.35	0.15-0.25	0.05	0.05	0.15
B206.0	0.05	0.1	4.2-5.4	0.20-0.54	0.15-0.35	0.1	0.1	0.05	0.15
B206.2	0.05	0.07	4.2-5.5	0.20-0.55	0.20-0.35	0.05	0.05	0.05	0.15

Note: Individual value for a given element is the maximum limit.

With the increasing use of the recycled aluminum alloys which has higher iron content, however, the requirement to remove the iron from these sources has become a big concern in terms of the manufacturing technique and cost. Therefore, manufacturing premium Al-Cu alloy castings with high iron contents has become a great challenge. Then the rich recycled aluminum alloys can be directly used to cast premium 206 cast alloys for their wider applications.

To reduce the detrimental effect of iron on material properties, two main measures are usually used: one is to remove the iron from the alloys. Many such methods as the gravity sedimentation [6], centrifuge sedimentation [7, 8] and filtration [8] have been developed and used in recent years. Due to the low volume fractions of the iron-rich intermetallics in Al alloys, the efficiency of the gravity sedimentation and filtration is very low. In addition, there are also many limitations for the use of these methods. For instance, it will be difficult to fully sediment the iron-rich intermetallic particles and separate them from the molten metal due to the small density differences between the intermetallics and the melt.

The other way is to modify the characteristics of the iron-rich intermetallics, such as, the morphology, dimension, and quantity to decrease the detrimental effect, particularly the platelet-like iron-rich intermetallics. This method to modify the characteristics of the

iron-rich intermetallics is usually carried out by adding neutralization elements such as Mn [9-14], Si [11, 15] and Be [16-18], controlling cooling rates [19-21] and superheating temperatures [22, 23] and conducting solution treatment [1, 24-26]

Though much work on iron-rich intermetallics has been performed in Al-Si cast alloys, little has been reported for Al-Cu cast alloys to date. Therefore, this project is aimed to investigate (i) the solidification behaviors of the iron-rich intermetallics, (ii) their modifications by adding neutralization elements, controlling cooling rate, and conducting heat-treatment, and (iii) their effect to the tensile properties of 206 cast Al-Cu alloys.

1.2 Objectives

The main objectives of this study are to investigate the solidification characteristics of the iron-rich intermetallics, the control of the iron-rich intermetallics, and their effect on the tensile properties in 206 cast Al-Cu alloys. This research will mainly concentrate on investigating:

(1) the solidification characteristics of the iron-rich intermetallics in 206 Al-Cu cast alloys at various iron contents (0.15% -0.5%);

(2) the effect of neutralization elements, especially by the addition of Mn and/or Si on the formation and transformation of the iron-rich intermetallics;

(3) the influence of cooling rate during solidification on the formation and transformation of the iron-rich intermetallics; and

(4) the influence of the iron-rich intermetallics on the mechanical properties of the 206 cast Al-Cu alloys at various iron contents.

References

[1] G. K. Sigworth and J. Fred Major: *Light Metals*, Minerals, Metals & Materials Soc (TMS), San Antonio, TX, 2006, pp. 795-799.

[2] H. Baker, *Properties and selection: nonferrous alloys and pure metals*, American Society for Metals, Metals Park, Ohio, 1979.

[3] V. S. Zolotorevsky, N. A. Belov and M. V. Glazoff, *Casting aluminum alloys*, Elsevier Science, Oxford, 2007.

[4] N. P. Lyakishev, Mashinostroenie, Moscow, Russia, 1996.

[5] N. Roy, A. M. Samuel and F. H. Samuel: *Metall. Mater. Trans. A*, 1996, Vol. 27, pp. 415-429.

[6] S. G. Shabestari and J. E. Gruzleski: *Metall. Mater. Trans. A*, 1995, Vol. 26, pp. 999-1006.

[7] Y. M. Liu, L. S. Yang, Q. Xia and D. X. Yang: *Journal of Luoyang Institute of Technology*, 1999, Vol. 20, pp. 55-58.

[8] H. Matsubara, N. Izawa and M. Nakamsbi: *Light metals*, 1998, Vol. 48, pp. 93-95.

[9] P. Ashtari, H. Tezuka and T. Sato: *Mater. Trans., JIM*, 2003, Vol. 44, pp. 2611-2616.

[10] S. Belmares-Perales, M. Castro-Román, M. Herrera-Trejo and L. E. Ramirez-Vidaurri: *Met. Mater. Int*, 2008, Vol. 14, pp. 307-314.

[11] H. Kamguo Kamga, D. Larouche, M. Bournane and A. Rahem: *Metall. Mater. Trans. A*, 2010, Vol. 41, pp. 2844-2855.

[12] L. A. Narayanan, F. H. Samuel and J. E. Gruzleski: *Metall. Mater. Trans. A*, 1994, Vol. 25, pp. 1761-1773.

[13] C. J. Tseng, Ph. D thesis, Engeering college, National Central University Taiwan, China, 2003.

[14] C. J. Tseng, S. L. Lee, S. C. Tsai and C. J. Cheng: *J. Mater. Res.* , 2002, Vol. 17, pp. 2243-2250.

[15] A. Couture: *Int. Cast Met. J.*, 1981, Vol. 6, pp. 9-17.

[16] S. Murali, K. S. Raman and K. S. S. Murthy: *Mater. Sci. Forum*, 1996, Vol. pp. 207-222.

[17] D. A. Granger, R. R. Sawtell and M. M. Kersker: *AFS Transction*, 1984, Vol. 115, pp. 579-586.

[18] S. Nishi and T. Shinoda: *Metals Abstracts*, 1969, Vol. 2.

[19] M. Ceylan, I. Aksoy, V. Kuzucu and Ş. Nevin Balo: *J. Mater. Process. Technol.*, 1997, Vol. 65, pp. 41-51.

[20] G. Kasperovich, T. Volkmann, L. Ratke and D. Herlach: *Metall. Mater. Trans. A*, 2008, Vol. 39 A, pp. 1183-1191.

[21] L. Y. Zhang, Y. H. Jiang, Z. Ma, S. F. Shan, Y. Z. Jia, C. Z. Fan and W. K. Wang: *J. Mater. Process. Technol.*, 2008, Vol. 207, pp. 107-111.

[22] X. F. Bian, G. H. Zhang and S. X. Zhao: *Special Casting and Non-ferrous Metals*, 1992, Vol. 4, pp. 19-25.

[23] X. Cao and J. Campbell: *Int. J. Cast Met. Res.*, 2003, Vol. 15, pp. 595-608.

[24] Y. Awano and Y. Schimizu: *AFS Transction*, 1990, Vol. 176, pp. 889-896.

[25] L. A. Narayanan, F. H. Samuel and J. E. Gruzleski: *Metall. Mater. Trans. A*, 1995, Vol. 26, pp. 2161-2174.

[26] H. K. Kamga, D. Larouche, M. Bournane and A. Rahem: *Int. J. Cast Met. Res.*, 2012, Vol. 25, pp. 15-25.

CHAPTER 2

LITERATURE REVIEW

Chapter 2

Literature review

2.1 Iron in aluminum alloys

Iron is always present in commercial aluminum alloys. On the one hand, iron is one of the major alloying elements in some aluminum alloy systems. For instance, iron is added to improve the die soldering in die cast Al alloys or increase the strength at elevated temperature in Al-Cu-Fe-Ni alloys, such as AA2219 and AA2618 [1, 2]. On the other hand, iron has been thought to be one of the most harmful impurities in most of the other commercial aluminum alloys. According to Lyakishev [3], the solubility of iron is approximately 1.8 wt. % at 928 K (655 °C) in liquid pure Al but only 0.0052 wt. % at 723 K (450 °C) in solid pure Al. Therefore, almost all the iron will precipitate from liquid Al alloys in the form of iron-rich intermetallics.

2.1.1 Sources of element iron in aluminum alloys

As mentioned above, iron can have detrimental influence on most of the aluminum alloys; therefore, it is important to understand where the iron in aluminum alloys comes. Generally speaking, iron is mainly originated from the (i) casting processes, (ii) primary

metal and master alloys, (iii) iron tools and equipment used during melting, transferring and casting, and (iv) recycled materials [4].

During casting, iron may be added as an alloying element if the alloy is intended for high pressure die castings since iron can deter the soldering of the cast part to the die. In low pressure permanent mold casting, the molten metal moves vertically from the crucible through a cylindrical stalk made of cast iron. Then the contamination of the melt by iron occurs as the molten metal in the stalk may run back and mix with the melt in the pot. Then, the melt will gradually be contaminated over times.

The second source of iron is due to the use of primary metal and master alloys. During the melting, master alloys are usually added to optimize the chemical compositions and the iron in the master alloys will enter the resultant alloys.

Another origination of iron is from the iron tools and the equipment containing iron used during the casting. For instance, it is known that the molten aluminum will dissolve iron from the gooseneck portion of the unit in hot chamber die casting process. The use of stirring and transferring equipment such as the ladle made of cast iron will also increase the iron content in the cast aluminum alloys.

Moreover, a major source of the iron contamination, which is becoming more and more important, is the use of some recycled scraps. It was reported that an average of 72 lbs

of secondary aluminum was used for each among the 14.6 million cars produced in 1994 [4]. Nowadays, with the rapidly increasing production of automobiles and consumption products, the use of the recycling scrap such as secondary aluminum has become much more economically. However, these recycled scraps usually contain much higher iron and thus may significantly increase the iron contents in the resultant aluminum cast alloys.

2.1.2   Iron-rich intermetallics in Al-Cu alloys

Due to the extremely low solubility of iron in solid aluminum (only 0.0052 wt. % at 450 °C [3]) almost all the iron will precipitate from liquid Al alloys in the form of iron-rich intermetallics.

In Al-Si foundry alloys, the iron-rich phases can form in different kinds of morphologies, including platelet, Chinese script, spherical or globular, rosette-like, polygonal, hexagonal, polyhedral, star-like, clusters and other indefinite shapes. The most common iron-rich phases in hypoeutectic Al-Si foundry alloys are β-Al$_5$FeSi with a needle or platelet morphology, α-Al$_8$Fe$_2$Si with a Chinese script morphology and π-Al$_8$Mg$_3$FeSi$_6$ formed in the presence of high Mg content with Chinese script morphology [5]. The α-Fe phase can also appear as Al$_{15}$(FeMn)$_3$Si$_2$ or Al$_{15}$(FeMnCr)$_3$Si$_2$ polyhedrons if it solidifies as a primary phase, particularly at high iron equivalent value (IEV = 1 Fe + 2 Mn + 3 Cr [6]).

The volume fraction, size, and morphology of the iron-rich phases are strongly influenced by alloy composition, such as the Fe, Mn, P and Mg contents, cooling rate, Sr modification and melting superheating [7].

The iron-rich phases in Al-Cu alloys depend on the compositions of the alloy systems. Depending on the Cu content and the application, Al-Cu alloys can be divided into four groups [8]:

(a) High-strength and heat-resistant alloys with 5% Cu, and small amounts of Mg and Mn;

(b) High-strength alloys containing 4-5% Cu and Ni (up to 2%);

(c) Alloys possessing improved casting properties with 7-10% Cu and Si (up to 4%); and

(d) Piston alloys with 10-14% Cu.

Based on the alloy chemistries, the following observations can be obtained:

(1) The alloys in the first group have very high mechanical properties because the concentration of copper (about 5%) reaches the maximum solubility in solid aluminum. These alloys have been most widely used and the typical alloy grades include AM5, 204.0 and 206.0. However, these alloys often have much more strict limitation on the contents of

impurity iron than Al-Si alloys, usually no more than 0.1~0.15 wt. % iron. For instance, the iron content in 206.0 cast alloy is usually about 0.05~0.15 wt. %.

In this family of Al-Cu alloys, iron can react with copper to form the Al_7Cu_2Fe or $Al_6(FeCu)$ phases in the absence of some elements such as Mn and Mg. Mn can substitute Fe and Cu, and may lead to the formation of $Al_{12}CuMn_2$, $(AlCu)_6(FeMnCu)$ and $Al_{15}(FeMn)_3Si_2$ [7]. When the impurities, both Fe and Si, are present to some contents, it is more probable to form a complex $Al_{15}(FeMn)_3Si_2$ phase [9], which has a typical skeleton-like morphology. Al_3Fe phase can be found in the slowly solidified alloys at a rather high iron concentration [10].

(2) The difference between the second group and first group Al-Cu alloys is the addition of nickel. In the second family of Al-Cu alloys, alloys 203.0, 242.0 are most often used in industries. Because of the addition of nickel, iron can completely dissolve and react with nickel to form Al_9FeNi and Al_7Cu_4Ni. Due to the less detrimental effect of the Al_9FeNi and Al_7Cu_4Ni phase, the allowable content of iron is somewhat higher (0.4-1.0 wt. %) than that in the first group.

(3) The third group of the Al-Cu alloy is with the addition of silicon, and thus the casting properties will be much better than the first two groups due to the formation of a significant amount of ternary eutectics such as $(Al)+(Si)+Al_2Cu$. Meanwhile, the presence

of silicon which has high diffusion coefficient in aluminum may considerably lower the heat resistance of these alloys as compared to the first two groups. The typical alloys in this group are 213.0 and 218.0. Iron can form the Al_5FeSi phase in the absence of Mn. With the addition of Mn, $Al_{15}(FeMn)_3Si_2$ or Al_8Fe_2Si phase may precipitate.

(4) The fourth group, also called as piston alloys contains more than 10%Cu. The typical alloy is 222.0. This group are characterized by the high levels of allowable iron concentration (up to 1.5%), which is related to the highly hetero-phase structure and the comparatively low mechanical properties; both factors diminish the effect of iron-rich phases. However, this group has not been widely used in modern industries due to the replacement by the heat-resistant 339.0 alloys.

2.1.3   Effect of iron on mechanical properties of cast aluminum alloys

Iron in Al-Cu cast alloys can form ternary and quaternary intermetallic phases, such as Al_7Cu_2Fe, $Al_{15}(FeMn)_3(SiCu)_2$, and $Al_6(MnFeCu)$ in 206 type alloys. These iron-rich intermetallics have different morphologies, structures and properties, and thus will have significant effects on the mechanical properties of the cast Al-Cu alloys. Regarding the effect of iron on the tensile and yield strengths, there exist some inconsistent conclusions: the results of some researchers [11] show that the tensile and yield strengths slightly

increase with the addition of iron while other researchers [12, 13] have observed a decrease in both tensile and yield strengths of the aluminum alloys with increasing iron content. Basically, it is agreed that iron increases hardness and greatly reduces the fracture toughness, ductility, fatigue resistance and impact energy [14-18]. All iron-rich compounds are characterized by high hardness and brittleness; therefore, they can increase hardness but reduce ductility, fracture toughness, fatigue, etc.

To understand the effect of iron-rich phases on the mechanical properties, several factors need to be considered, including the iron content, morphology, volume percentage, and distribution of the iron-rich phases formed. Among these, the morphology of iron-rich phases plays a much more important role in the mechanical properties of the alloys. Generally speaking, globular or Chinese script iron-rich intermetallic phases have less harmful influence on mechanical properties. Because cracks formed in these intermetallics have a relatively compact form. A well known typical example of these intermetallic phases is $Al_4Be_5Fe_2$ which can crystallize in a rounded shape. In addition, $Al_{15}(FeMnCu)_3Si_2$ and $Al_6(FeMnCu)$ in Al-Cu alloys and Al_8Fe_2Si in Al-Si alloys also have typical Chinese script shape, which has been thought to have less detrimental effect on the mechanical properties.

The most harmful iron-rich intermetallic phases to mechanical properties are platelet particles, especially, primary crystals. Though the iron-rich phases in Al-Cu alloys are

usually formed by eutectic or peritectic reactions, primary crystals may also precipitate at high Fe content.

The typical platelet iron-rich phases are Al_7Cu_2Fe in Al-Cu and Al_5FeSi (β-AlFeSi) in Al-Si alloys. The main reason for the detrimental effect of the platelet iron phases is that these phases can cause strong stress concentration and promote the initiation of sharp micro-cracks [10]. The platelet phases have more deleterious effect on mechanical properties due to not only the edges or tips of the platelet but also the high aspect ratio in the platelet Fe-rich phases. At high aspect ratio, there was more chance to block the movement of dislocations in alloys. While more and more locations have been blocked and piled-up on the particles, higher stress concentrations would occur. Therefore, the needle-like or platelet-like phase acted as the stress concentrators. Other researchers also observed [19] that the bonding strength between the aluminum matrix and the β phase was very weak, and this poor bonding strength would cause decohesion. Because of the decohesion, the particles would act as two-dimensional defects. When there were some external tensile stresses, the particles would be the source of cracking.

Recently, a new explanation about the detrimental effect of the iron-rich intermetallics including β phase on the decreasing mechanical properties has been proposed by Cao and Campbell [19-23]. In their researches, they found that the iron-rich phases can

nucleate on the oxide films which have two surfaces: the dry, unbounded inner surface and the wetted exterior surfaces. These oxide films can form during the melting prior to casting, or during the pouring of liquid metal because of the surface turbulence. The unbounded, dry surface was the original surface which contacts with air and become folded into the bulk liquid by the entrainment event. In contrast, there would be good atomic contact between the wetted side of the film and the liquid. Then the iron-rich phase would nucleate on these wetted outside surfaces of the bifilms. However, the two dry, unbounded surfaces would be the gap (obstacle for the diffusion of atom) and constitute the crack which would be responsible for the decreasing mechanical properties. Miller *et al.* [24] have further confirmed this mechanism.

2.2 Control of the detrimental effect of iron in cast alloys

As discussed above, there exist many approaches from which iron can be present in cast aluminum alloys. It is generally agreed that iron can have harmful effects on mechanical and casting properties. Therefore, it is necessary to control the effect of iron on the properties of cast Al-Cu alloys. Generally speaking, there are two main approaches to reduce the detrimental effect of iron on alloy properties: one is to remove iron-rich intermetallics from the alloy. Here, the iron-rich intermetallics to be removed are mainly

the primary iron-rich particles. The density difference between the iron-rich intermetallics and the liquid aluminum is the driving force to sediment primary iron-rich intermetallic particles.

The other way is to modify the iron-rich phases, including the phase transformation in morphology from platelet to Chinese script. The latter has been thought to have much less detrimental effect on the properties of the alloys. In addition, controlling the dimensions and the volume fraction of the iron-rich phase can also minimize their negative effect. These methods can be grouped into approaches to control the detrimental effect of iron in casting aluminum alloys.

2.2.1 Methods to remove the iron from melt

The principle of the physical methods are as follows: First, the iron-rich phases precipitate from the molten alloy, and then the iron-rich phases can sediment when the particles of iron-rich phase have grown to some sizes due to the density difference between the iron-rich phases and the molten metal. In addition, filtering technique can be used to separate iron-rich intermetallic particles from aluminum melts. Based on this principle, some methods have been developed, i. e. gravity sedimentation, centrifuge separation and electromagnetic separation.

Gravity sedimentation can be grouped into two ways: gravity sedimentation and chemical sedimentation. When some primary iron-rich intermetallics form at high temperature, the melt will be held at certain temperature for a long time so that the iron-rich intermetallics can settle to the bottom of the molten metal. This way is called gravity sedimentation. On the other hand, some elements, such as Mn, Cr, Ni, Zr and Si will be added to the liquid. These elements can react with iron to form new iron-rich intermetallics. Then these iron-rich intermetallics will settle or sediment to the bottom due to their higher density and this way is called chemical sedimentation.

Gravity sedimentation is related to the solid fraction and there is a critical value, which is about 0.2~0.6 [25]. If the solid fraction is higher than the critical value, the formation of matrix skeleton phase will restrain the sedimentation effect.

Shabestari *et al.* [26] studied the kinetics of settling of iron-rich intermetallic compounds in a melt of Al-12.5% Si with 1.2% Fe, 0.3% Mn, and 0.1% Cr and found that the volume percent of the intermetallics increases with distance from the melt surface and the settling speed of the intermetallics reaches the terminal velocity at very short times and very close to the liquid surface. Cao *et al.* [27] have investigated the effect of iron and manganese contents on convection-free precipitation and sedimentation of primary α-Al(FeMn)Si phase in liquid Al-11.5Si-0.4Mg alloy and it is found that almost all the

primary α-Al(FeMn)Si particles seem to completely settle to the base of the melts when the melt is held at 600 °C. Additionally, particle volume fraction, weight, number and size increase with the increasing iron equivalent values or Mn/Fe ratio at a given iron level. Unuvar et al. [28] found that some new iron-rich intermetallics will form in the liquid aluminum with the addition of Si. When the liquid is settled at 585 °C, the iron-rich intermetallics can be separated because of the density difference and then the content of iron in aluminum can decrease from 2% to 0.5%.

However, due to the low volume fraction of the iron-rich intermetallic particles in the alloy, the efficiency of sedimentation and filtration is very low. Besides, there are some limitations for the use of these methods. For instance, the molten metal should be held at a comparatively low temperature for a long time in order to favor the precipitation and growth of iron-rich phases. When these iron-rich phases have been separated from molten metal, it needs to heat the molten metal again to a higher temperature for the casting or other operations. Due to the extensive existence of convection caused by the differences in temperature or density, the iron-rich particles are difficult to fully sedimentations separate from the melt by gravity sedimentation.

Centrifuge separation is similar to the gravity sedimentation. In centrifuge separation, the iron-rich intermetallics with higher density will be swung to the wall because of the

centrifugal effect. Then the rotation rate can be changed to adjust the centrifugal force and control the separation of iron-rich intermetallics.

Liu et al. [29] studied the effect of centrifugal and filtering on the Al-Si-Ti alloy and found that the iron can be efficiently removed using the combined way. Matsubara et al. [30] also found that the iron content can decrease from 2.07% to 0.27% under the centrifugal force. Fang et al. [31] have studied the composite method of sinking and filtering of iron-rich intermetallics for aluminum alloy and found that this combination is efficient to remove the iron-rich intermetallics. The tensile strength of aluminum alloy increased by 25% while the elongation increased by 144% after the combined treatments of the sedimentation and filtrations.

For centrifugal separation, the time for sedimentation will be shorter compared with gravity sedimentation. However, before the separation, the molten metal should be poured into a mold first and the iron-rich phases can segregate on the wall of mold at the function of centrifugal rotation. The remaining liquid metal can be transferred into the oven before the solidification. Therefore, this process will be complicated and may lose some liquid metal.

Electromagnetic separation is also used to remove the iron-rich intermetallics in aluminum industries. The conductivity difference between the impurity and aluminum melt

is the most important factor for electromagnetic separation. The driving force has no relation with the density, chemical composition and states between the iron-rich intermetallics and molten alloy. This method can be used to separate the particles with similar density to aluminum melt. Compared with the gravity sedimentation and centrifugal separation, electromagnetic separation has some advantages, such as high efficiency, no pollution and high process stability. But the high cost is the shortcoming for this method.

Zhang *et al.* [32] have analyzed the force acting on the magnetic impurities in alternative magnetic field and compared the magnetic forces formed in alternative and steady magnetic field. They found that electromagnetic force is mainly responsible to move impurity particles to inner side at a magnetic induction intensity of more than 145 mT while magnetic force is dominant in moving the impurities to the outer side of the separator at a magnetic induction intensity of less than 120 mT.

However, there are many limitations for physical methods to remove the iron from the melt and the technology is not so mature. Besides, this will increase the cost of casting. Therefore, physical methods are not widely used in modern industries in terms of the technology and cost.

2.2.2 Approaches to control the detrimental effect of iron

As discussed above, different measures are often used in modern industries to control the detrimental effect of iron in casting aluminum alloys. However, there are many factors affecting the characteristics of the iron-rich phases, including alloy composition, cooling rate, neutralization elements, molten superheat and heat-treatment. Therefore, the effect of these factors on the formation and transformation of the iron-rich phases will be dealt with in this part.

2.2.2.1 Effect of cooling rate on iron-rich intermetallics

Cooling rate plays a significant role in the final structure of castings. Up to date, much work has been carried out to investigate the effect of cooling rate on iron-rich phases. Samuel *et al.* [33] studied the effect of cooling rate on the formation of iron-rich intermetallics in Al-6.5% Si-3.5% Cu-Fe alloy. They found that there was a strong linear relationship between the dendrite arm spacing (DAS) and the average β-platelet length at a given iron level, indicating that the DAS can be used as a reliable indicator of the average β-platelet length. The average β-platelet length decreases with increasing cooling rate. Belmares-Perales *et al.* [34] also investigated the effect of cooling rate on the volume fractions of α-AlFeSi and β-AlFeSi phases in Al-7.3% Si-3.4% Cu alloy. However, they

found that the β-AlFeSi would disappear at both very low and high cooling rates. In their

opinion, the suppression of the β-AlFeSi resulted from the decrease in micro-segregation at

low cooing rate. At high cooling rate, the growing difficulties led to the disappearance of

this phase. Gustaffon *et al.* [35] found that the iron-rich phases with platelet and acicular

shapes would decrease and the Chinese script type phase would increase with increasing

cooling rate. Besides, the maximum average length of total iron-rich phases would become

smaller at higher cooling rate. Sigworth *et al.* [36] pointed out that high cooling rate would

help the distribution of iron-rich phases much more uniformly, which would have less

detrimental effect on the properties of the alloy. Vorren *et al.* [37] discussed the effect of

cooling rate on the formation of α-Al_8Fe_2Si in Al-Si cast alloy and found that the volume

fraction of α-Al_8Fe_2Si phase would reduce with decreasing cooling rate and this phase may

even disappear at a rather low cooling rate.

2.2.2.2   Effect of neutralization elements on iron-rich intermetallics

Some elements can be added to the cast aluminum alloys to react with iron to form

some less detrimental intermetallic phases. Mn and Sr are the two most widely used

neutralization elements in Al-Si cast alloys. Cr, Co, Be, S, and Mo are also used.

(1) Mn

Mn, up to 1.0 wt. %, can be presented in many Al-Cu alloys, and it is usually able to completely dissolve into the Al matrix after solidification. The most important is that Mn can act as the neutralizer to change the morphology of the iron-rich intermetallics. Many researches [7, 34, 38, 39] have studied the effect of Mn on the iron-rich intermetallics in Al-Si cast alloys and they found that Mn can reduce the detrimental effect of the β phase by replacing it with the less-detrimental Chinese script α-Al$_{15}$(FeMn)$_3$Si$_2$ phase.

Ashtai et al. [38] suggested that the addition of Mn or Mn and Sr can refine the β-Fe phase or even transform the β-Fe phase into α-Fe phase. Hwang et al. [6] investigated the effect of Mn additions on the microstructure and mechanical properties of Al-Si-Cu cast alloys. Their results had proved the conclusions of Ashitai et al [38]. Besides, they also found that Mn/Fe ratio had an important effect on the transformation of iron-rich intermetallics from plate-like β intermetallic phase to Chinese script α phase and a threshold of 1.2 for Mn/Fe was recommended for the effective modification

Belmares-Perales et al. [34] also investigated the Mn/Fe ratio on the volume fractions of α-AlFeSi and β-AlFeSi phases in Al-7.3Si-3.5Cu alloy. They found that the volume fraction decreased for β-AlFeSi but increased for α-AlFeSi when Mn increased to the same level of the Fe content, indicating that the transformation from β-AlFeSi to α-AlFeSi increased with increasing Mn/Fe ratio. However, the threshold value for Mn/Fe ratio is

about0.8, which is lower than that of Hwang *et al.* [6]. The reason for this difference is probably due to the different cooling rate used in the experiments. Narayanan *et al.* [39] had done some works on the cooling rate at different Mn/Fe ratios. They found that in alloys with no addition of Mn, both the temperature for the onset of β-AlFeSi formation and its length decreased with increasing cooling rate. In the presence of Mn, α-AlFeSi was favored at low cooling rates, whereas both α-AlFeSi and β-AlFeSi phases appeared at high cooling rates.

Lu *et al.* [7] have investigated the effect of Mn on the iron-rich intermetallics in hypoeutectic Al-Si alloys and found that the addition of Mn leads to the considerable decrease in both the volume fraction and the size of the β phase. The reason is that part of the Fe in the melt precipitates as a new Chinese script-like (or polyhedral) α-Fe phase prior to the appearance of eutectic Si and thus less free Fe is available to form the platelet β-Fe. As a result, the amount of the β-Fe phase decreases. Therefore, Mn can suppress the formation of β-Fe and promote the more compact, less harmful α phase. Some reports [40, 41] also pointed out that Mn is effective in suppressing the β platelets and helping the transformation β phase into α phase but the total amount of the Fe-rich precipitates was increased and the excessive Mn addition would cause severe sludge problems.

Tseng *et al.* [42, 43] have studied the effect of Mn on the microstructure and mechanical properties of A206 alloys. It was found that the dominant iron-rich intermetallics is Chinese script Mn-bearing phase when Mn is added to 0.66-0.67% at 0.05-0.30% Fe, in which the Mn/Fe ratio is about 2-13, which is much higher than the reported Mn/Fe ratio to suppress the formation of platelet β-Fe being about 1 in Al-Si cast alloys [6, 7, 38]. The volume fraction of iron-rich intermetallics increases with increasing. Besides, increasing the Mn solution level retarded the precipitation of the strengthening phase (θ' or θ-Al2Cu) and the small grain size induced by $Cu_2Mn_3Al_{20}$ particles is one of the factors that determine the hardness of 206 alloys.

In summary, Mn can cause the transformation of iron-rich intermetallics form β phase to α phase. However, the mechanism is still not fully understood and the threshold Mn/Fe ratio still needs to be further investigated.

(2) Mg and Si

In 206alloy, Mg is usually present and can influence the characteristics of iron-rich intermetallic phases. Samuel *et al.* [44] reported that smaller size and lower volume fraction of β platelet were obtained in Mg-containing B319 alloys, as a result of the transformation of the β-Al_5FeSi phase into $Al_8Mg_3FeSi_6$. However, Zak *et al.* [45] found that no transformation of β-Al_5FeSi intermetallics into $Al_8Mg_3FeSi_6$ was observed at 0.5% Mg in

Al-Si-Cu alloy but the increase of Mg content led to the preferential precipitation of $Al_8Mg_3FeSi_6$ and Mg_2Si phases. The 0.8% difference in Mg content for two 319 alloys resulted in only slight changes in the predicted β-Al_5FeSi phase mole fraction, so no significant transformation fromβ-Al_5FeSi intermetallics into $Al_8Mg_3FeSi_6$ can be expected.

Though Si is thought to be an impurity element in casting Al-Cu alloys, it is found that the iron-rich phases may change in the presence of Si. Usually, two ternary phases, cubic α-$Al_{12}Fe_3Si$ and monoclinic β-$Al_9Fe_2Si_2$, form by a eutectic reaction in Al-Si cast alloys [4]. At low silicon contents, first the α-Al-Fe-Si and then the β-Al-Fe-Si phases appear. Lu *et al.* [7] investigated the effect of addition of Si on the iron-rich intermetallic phases and they found that Si, like Mn, was expected to suppress the coarse binary β-Fe phase. But unlike Mn, it would not increase the total amount of the intermetallics. With further addition of Mn above 0.3 wt. %, both α-Fe and β-Fe phases were observed to precipitate prior to the eutectic Si. In the study of Kamga *et al.* [9] and Couture [10], it is reported that Fe/Si ratio plays a significant role in inhibiting the formation of platelet β-Al_7Cu_2Fe in Al-Cu cast alloys and found that the ratio should keep between 1 and 1.2 in Al-Cu cast alloys.

(3) Sr

Sr is often used as the modifier in Al-Si cast alloys to get finer eutectic silicon particles. However, many researchers have found that Sr also has some effect on iron-rich phases. Rathindra [46] found that in 356 alloy with 0~0.65% iron content, the addition of Sr could suppress the formation of β-AlFeSi phase and change the morphology of β-AlFeSi phase from platelet to star. Shabestari *et al.* [47] also investigated the effect of Sr and they found that with 0.02% addition of Sr to 413 alloy at1.18% Fe, the iron-rich phases obtained became fine global shape and both the size and amount of the iron-rich phase decreased and. However, they also found that if the addition of Sr exceeded 0.08%, the size of the iron-rich phase would become bigger instead of smaller.

Samuel *et al.* [44] compared 319 alloys after different treatments and found that the alloy after degassing and with the addition of Sr contained the least β-AlFeSi phase. Samuel *et al.* [48] also found that when the Sr content was about 300 ppm, the best morphology of the iron-rich phases could be obtained. At a given cooling rate, about 55% β-AlFeSi phase had sizes in the range of 0~40 μm with no addition of Sr in 319 alloy but about 90% β-AlFeSi phase is within 0~40 μm after the addition of 300 ppm of Sr,

Espinoza-Cuadra *et al.* [49] have studied the effect of Sr and solidification conditions on the intermetallics in Al-Si 319 alloy and found that the formation of β or α phase is related to the undercooling and overheating temperatures, as well as Sr modification which

can reduce the formation temperature of iron-rich intermetallics. They found that the good combination of these three factors will inhibit the formation of β-Fe phase and lead to the precipitation of α-Fe phase.

Cao *et al.* [50] also have investigated the effect of Sr on primary α-Fe in liquid Al-11.5Si-0.4Mg cast alloy. It was found that Sr could refine the primary α-Fe particles, which led to the increase of the number of primary α-Fe particles. Besides, Sr could cause a decrease in the particle volume fraction but an increase in the number of the sediment particles and a great increase in the depth of the sediment in the mould at higher superheating temperatures. Mahta *et al.* [51] proposed that Sr poisoned the oxide film substrate which can nucleate β-Al5FeSi. Then less effective oxide film available led to the decrease in the number of β-Al5FeSi.

(4) Cr and Co

Cr and Co are also used in industries to modify the iron-rich intermetallics. Gustaffon *et al.* [35] have investigated the effect of Cr on the iron-rich phases in Al-7Si-0.3Mg alloy. They found that $β-Al_5FeSi$ and coarse $π-Mg_3Al_8FeSi_6$ would be present without the addition of Cr and the acicular $β-Al_5FeSi$ phase would transform to the fine $π-Mg_3Al_8FeSi_6$ or Chinese script $α-Al_8Fe_2Si$ with the addition of Cr, which would improve the mechanical properties. Murali *et al.* [18] also pointed out that with the addition of Cr, the Chinese script

Cr-Fe phase would replace the acicular β-Al$_5$FeSi phase, which would be more likely to happen at higher cooling rate.

Furthermore, Crepeau [52] pointed out that the amount of addition of Co would be more than Mn in order to form the global-like iron-rich phase. In the research of Murali *et al.* [18], it was found that Co could react with iron to form Chinese script Co-Fe phase. The Co-Fe phase would have perfect Chinese script and distributed uniformly when the iron content was 0.33% with the addition of 0.24% Co. At higher iron content, more Co should be added. For example, at 0.67% iron content, the addition of Co would be 0.78~0.93% to get uniformly distributed Co-Fe phase.

(5) Be

As early as in 1960s, some researchers [53] found that with appropriate addition of Be to Al-Si alloys, the detrimental influence of iron-rich phase could be reduced. Gowri *et al.* [54] found that in Al-Si alloys, 0.05%~ 0.5% addition of Be could form global-like iron-rich phase. In the research of A357 alloy by Granger *et al.* [55], it was concluded that the main reason for the detrimental effect of the iron-rich phase was the presence of Al$_{10}$Mg$_4$Si$_4$Fe. With the addition of Be, the morphology will change to Chinese script, which results in the improvement of the mechanical properties. Eijikato [56] has investigated the influence of Be, Mn, Cr on the iron-rich phases. They found that Mn, Cr

and Be all could form the iron-rich phases in Al-Si alloys. With the increase of iron content in the alloy, the amount of Mn, Cr and Be required also would be higher, which would form coarse iron-rich phases and had harmful effect on the ductility of the alloy. However, with the multiplex addition of Mn, Cr and Be, the amount required would be less compared with a single addition of Mn for the full formation of Chinese script. For example, in Al-Si alloy with 1.0% iron, the 0.2% addition of both Mn and Be would have a good effect.

Murali *et al.* [18, 57-59] have systematically investigated the influence of Be on iron-rich phases. They found that in Al-Si alloys, with appropriate addition of Be, the iron-rich phase could be polygon, hexagonal and Chinese script shapes. When the Fe and Be contents were both very high (Fe> 1.0%, Be >0.2%), the iron-rich phase with hexagonal shape could be more likely to form. When the iron content is high (>0.7%) and Be content is somewhat low (<0.2%), almost all the iron-rich phase would be Chinese script shape. However, when the Fe and Be contents were both very low, it was difficult to distinguish the iron-rich phases [59].

Tan *et al.* [16] investigated the behavior of Be and Fe in A357 alloy. It was found that with the addition of Be, the platelet β-Al_5FeSi had been replaced by phases with Chinese script or global shape. It was concluded that not only the morphology but also the amount and distribution of the iron-rich phases had changed with the addition of Be.

(6) Other elements

Besides these neutralizers as discussed above, some other elements are also reported to have similar effect on iron-rich intermetallics, such as, Mo, S, and RE.

Khudokormov et al. [60] found that Mo could be an effective neutralizer for Al-Si alloy. In their research, it was observed that with addition of 0.2% Mo to the alloy containing 1.2% Fe, the tensile properties and ductility would be improved.

Zhu et al. [61] investigated the effect of S on the iron-rich phase in ZL-108 alloy and they found that with the addition of S, most of the iron-rich phases changed into Chinese script shape and the effect would be more positive with the combined addition of Mo and S. However, there is little effective way to add S to the alloy. Besides, the addition of S may lead to the contamination, and thus S is unlikely to be used as an effective neutralizer.

Li et al. [62] have done some researches about the effect of RE on the iron-rich intermetallics and found that with the addition of RE, the formation of platelet iron-rich phase would be retarded. In the research of Zhu et al. [61], it was found that the addition agent (8% Cr, 3% Mn, 10% RE, and 79% Al) would have a positive effect. With this addition agent being added, the platelet and acicular phases would change to the phases with global, Chinese script or rosette shapes.

Besides, some researchers have investigated the use of the agent for spheroidization of iron compounds in aluminum alloys. Liu *et al.* [63] have investigated the effect of spheroidization agent on the aluminum alloy with high iron content (1.0%~4.0%) and they found that with the addition of the spheroidization agent, the global iron-rich phase had replaced the acicular phase, which made the tensile strength increased by 20%~90% while the elongation increased by 40%~100%. Others [64] also found that adding the spheroidization agent to the alloy at 750 °C would make the formation of $TiAl_3$ and $Al_{34}Ti_{20}Si_{12}Fe_{15}Mn_8$ compounds, which would act as the nucleation site for iron-rich phases.

2.2.2.3   Effect of superheat on iron-rich intermetallics

As early as in 1975, it was reported that with the increase of superheating temperature, the morphology of the iron-rich phase will be changed. When the liquid is heated above the liquids temperature, some changes may appear, including the purity of the alloy, the melting of high-melting point compounds and so on. Cao *et al.* [65] have investigated the effect of superheating in Al-11.5Si-0.4Mg alloy and found that a superheating temperature of approximately 850 °C may facilitate the nucleation of primary α-Al(FeMn)Si phase but hinder its growth, causing sufficient increase in particle weight

and number, and a decrease in particle size. Superheating at 900 °C caused no significant variations in the precipitated weight, number and size of the primary α-AlFeSi phase compared to 760 °C.

Some researchers [66, 67] have studied the effect of superheat with the addition of Mn on the iron-rich phases. They found that adding Mn to the melt at superheating temperature would improve tensile strength by 40~80 MPa and the elongation by 6%~7% compared with traditional melting temperature with Mn additions in Al-Si alloys. They also found that superheating with addition of Mn would refine the iron-rich phases to about 10~40 μm.

Nafisi *et al.* [68] investigated the effect of electromagnetic stirring with the superheating in Al-Si-Fe alloy and found that electromagnetic stirring reduced the size of the primary α-Al particles but favored the formation of β-AlFeSi phase.

Bian *et al.* [69] pointed out that in Al-Si alloy with 0.8%~1.0% iron content, the morphology of the iron-rich phase would change form acicular to rosette and global with the increase of the melting temperature. In their report, it was observed that when the melting temperature was 840 °C, the iron-rich phase would be acicular shape. However, when the melting temperature was above 920 °C, all the iron-rich phases would be global shape. When the temperature was between 840 °C and 920 °C, the morphology would be

almost rosette but acicular and global phases would also appear. Awano *et al.* [70] have investigated the relationships between the iron content and the minimum temperature at which the Chinese script iron-rich phase began to form. They found that the minimum temperature would be higher with the increase of iron content. For example, in Al-6% Si alloy, when the iron content was 0.4%, the minimum temperature would be 790 °C. However, the temperature would be above 950 °C when the iron content was 0.55%. They also found that thermal histories had little effect on the change of the iron-rich phases. Liu *et al.* [64] also found that the transformations of the iron-rich phases to global morphologies in an Al-12.5% Si secondary metal alloy appear at high temperature. It was observed that the treatment temperature required to promote this morphological change was directly related to the iron content in the alloy.

However, there are different views on the effect of superheat on the iron-rich intermetallics. Narayanan *et al.* [39] found that the application of high temperature melt treatments before casting favored the formation of the α phase over β phase. When the temperature was above 750 °C, the γ-Al_2O_3 oxide presented in 319 alloys, which would act as the preferred nuclei for β-Al_5FeSi platelets, transformed to α-Al_2O_3. The α-Al_2O_3 oxide suppressed the nucleation of the β-Al_5FeSi phase and thus the α-Al_8Fe_2Si phase was preferred.

Sun *et al.* [71] found that with the increases of the superheating temperature, the finer FeAl$_3$ would precipitate. They explained that the high superheating temperature had changed the phase structure. It was deduced that there were many clusters containing iron and aluminum in melt under 900 °C. However, these clusters had been damaged when the temperature was higher than 900 °C and iron distributed randomly and uniformly in the aluminum melt. Besides, the undercooling would be bigger with the increase of the superheating temperature, and then the FeAl$_3$ would be refined.

In the research of Zhou *et al.* [72], it was also observed that the finer acicular iron-rich phase appear at higher superheating temperature. In their opinions, there were some high-melting point particles presented in the melt at the traditional melting temperature, and the new precipitates would form on these particles. However, when the melting temperature was about 1600 K, which was above the nucleation temperature of FeAl$_3$, the FeAl$_3$ would dissolve into the melt completely. Besides, the high temperature also eliminated the heredity of iron compound. Therefore, the refined structure would be obtained when the metals were cast at somewhat high superheat temperature.

However, there are still some issues to overcome for the application of superheating. One is that some elements will be burnt at high temperature. Besides, the condition will be stricter for the equipment because the high temperature will reduce the life of ovens.

2.2.2.4   Effect of heat-treatment on iron-rich intermetallics

Another way to modify the iron-rich intermetallic phases is to apply proper

heat-treatment, especially the solution treatment, in which the solution temperature is much

higher than the aging temperature. The conventional solution treatment is to heat the alloy

to a temperature below the final solidification temperature. At such a solution treatment

temperature, however, Griger *et al.* [73] found that acicular β-AlFeSi phase would not

dissolve to the matrix in Al-Si cast alloy, similar result also is found in 206 cast alloy [74].

However, Gustafsson *et al.* [35] found the solution treatment at a solution temperature

higher than the final solidification temperature would lead to the dissolution, break-up and

spheroization of the iron-rich phases. Narayanan *et al.* [75] also have done some researches

on the solution treatment. They found that under normal heat treatment conditions, the iron

intermetallics did not undergo any change. In their experiments, they used the

non-equilibrium solution treatment. The non-equilibrium solution treatment consists of

three steps, the quenching and T6 aging treatment which would be the same as equilibrium

treatment but the solution treatment would be different, which had a higher solution

temperature than equilibrium treatment. For example, the temperature higher than the

eutectic Al-Al$_2$Cu temperature was often used. In equilibrium solution treatment, because

of the lower temperature, most of the eutectic phases would not dissolve into the matrix.

However, it was possible for these eutectic phases to dissolve into the matrix; even 100% of these phases could dissolve into the matrix in non-equilibrium solution treatment.

In the experiments of Narayanan *et al.* [75], it was found that the appropriate temperature of non-equilibrium solution treatment was about 520 °C and 515 °C for the samples initially solidified at 10 °C/s and 15 °C/s, respectively. At the same time, they found that the strength of the 319 alloy with high iron would increase more than with the low iron after non-equilibrium solution treatment. Besides, it was observed that solution temperature played a much more important role in the dissolution of iron intermetallics than solution time did. It was found that the volume percentage of the iron-rich phases and average length of the β-AlFeSi phase did not show any appreciable variation with times longer than 8 hours. Liu *et al.* [76] have also done some researches about the effect of solution time on the iron-rich phases in A357 alloy. They found that after 1 hour, there was no significant change of the iron-rich phases because of the insufficient dissolution. However, 100 hours-solution treatment would refine the iron-rich phases with the coarser eutectic silicon particles. When the solution time was 10 hours, the optimum combination of small iron-rich phases and eutectic silicon particles would be obtained.

In summary, iron is usually regarded as the impurity element in casting aluminum alloys, and it can lead to the detrimental effect on casting and mechanical properties of

casting aluminum alloys. To reduce the harmful effect of iron, physical and chemical measures have been utilized, such as gravity sedimentation, addition of neutralization elements, high cooling rate, super-heating, and solution heat-treatment.

2.3 Investigations of iron-rich intermetallics in Al-Cu 206 cast alloys

206 cast aluminum alloys have been widely used in the automotive and aerospace industries due to its high strength and good elevated temperature properties. However, this alloy suffers a great loss of the mechanical properties in the presence of small amounts of Fe. In the 206 cast alloy family, the maximum iron content is usually limited to 0.15 wt. % (206.0) or even lower than 0.10 wt. % for (206.2) [77] for general purpose use. In the aerospace applications, the iron content is even required below 0.07 wt. % (A206.2) [77]. However, with the increasing use of the recycled aluminum alloys, the requirement for low iron contents becomes a big concern in terms of the manufacturing technique and cost. Therefore, manufacturing premium castings at higher iron contents has become a great challenge.

Due to its low solubility in solid Al, iron usually precipitates as the iron-rich intermetallics during solidification. For the iron-rich intermetallics in 206 family cast alloys with low iron content, Backerud *et al.* [78] investigated the solidification sequence for

42

A206 cast alloy with 0.03% Fe as early as in 1980's, as shown in Table 2.1 and found that Al_6(FeMnCu) was the first intermetallic phase formed and it was then transformed completely into β-Fe (Al_7Cu_2Fe) which had been thought to be the only iron-rich intermetallic phase present in the fully solidified A206 cast alloy at 0.03% Fe. Similar results were reported in A206 cast alloys at an iron level of ~ 0.10% [10, 79]. At higher iron contents, however, very limited work has been carried out for the study on the iron-rich intermetallics in 206 alloys. Although it is found that both α-Fe and β-Fe phases can coexist in 206 alloys at 0.05-0.3% Fe [13] and 0.1-0.3% Fe [9], the solidification sequence and the possible nucleation mechanisms are seldom addressed. Al_mFe is one of the most widely observed iron-rich intermetallics in AA1xxx and AA5xxx wrought aluminum alloys [80-83]. It was reported to precipitate at high cooling rate compared with other iron-rich intermetallics, such as Al_3Fe and Al_6Fe in Al-Fe-Si ingots [80, 81, 84]. To date, Al_mFe has never been reported in 206 cast aluminum alloys at higher iron content (0.5% Fe). In this family alloys, Mondolfo [11] once mentioned that Chinese script Al_3(FeMn) phase was possible to appear in the Al-Cu cast alloy with 5% Cu and 0.55% Fe if the Si level was much lower than the Fe content but no evidence was given.

Table 2.1 Solidification reactions for A206.2 alloy at 0.03 wt. % Fe [78]

No.	Reaction	Suggested Temp. (°C)
1	Development of dendritic network	651-649
2	Liq. $\rightarrow$ Al+Al$_6$(MnFeCu)	649
3	Liq. + Al$_6$(MnFeCu)$\rightarrow$ Al+Al$_{20}$Mn$_3$Cu$_2$	616
4	Liq. $\rightarrow$ Al+Al$_2$Cu+Al$_{20}$Mn$_3$Cu$_2$+Al$_7$Cu$_2$Fe	537
5	Liq. $\rightarrow$ Al+Al$_2$Cu+Al$_2$MgCu+Mg$_2$Si	500

The phase selection among iron-rich intermetallic Al$_3$Fe, Al$_6$Fe and Al$_m$Fe (i.e. Al$_3$(FeMn), Al$_6$(FeMn) and Al$_m$(FeMn) in the presence of Mn, respectively) has been frequently encountered in the Al-Fe binary alloy system, such as AA1XXX alloys during Direct Chill (DC) casting [81, 85, 86]. To date, the very limited investigations have indicated that the existence of diverse iron-rich intermetallics including α-Fe, β-Fe, Al$_m$Fe/Al$_m$(FeMn), Al$_3$(FeMn), and Al$_6$(FeMn) in 206 alloys at a high Fe level of 0.5%. The formation and phase selection of these intermetallics will certainly depend on the alloy chemistry and solidification conditions but little work has been carried out.

In order to improve the mechanical properties, the platelet-like iron-rich intermetallics are usually modified into Chinese script which has been thought to be less harmful to the mechanical properties due to the compact and globular morphology. To this end, the addition of neutralization elements such as Mn and/or Si [9, 10, 42] is one of the most widely used approaches to modify the platelet-like iron-rich intermetallics. It has been reported that the Mn/Fe and Si/Fe ratios are critical for the efficient transformation of

platelet β-Fe into Chinese script α-Fe [9, 10]. The critical Mn/Fe and Si/Fe ratios that can

completely suppress the formation of the platelet β-Fe vary with the Fe level. Up to date,

the thresholds of Mn/Fe and Si/Fe ratios have not been well established for the commercial

Al-Cu cast alloys with an iron level up to 0.5%. As early as in 1980's, Backerud et al. [78]

studied the solidification path of a 206 cast alloy with 0.03% Fe-0.05% Si-0.26% Mn and

found that β-Fe is the only iron-rich intermetallic phase in this alloy although the Si/Fe and

Mn/Fe ratios were as high as 1.7 and 8.5, respectively. In the study of Tseng et al. [13, 42,

43], β-Fe was also reported to be the dominant iron-rich intermetallic phase in the 206 cast

alloy with 0.05% Fe-0.01% Si-0.3% Mn and the β-Fe could almost be completely

transformed to Chinese script when Mn was added up to 0.66%, in which the Mn/Fe ratio

was as high as 13. Talamantes-Silva et al. [79] studied the characterization of a 206 cast

alloy with 0.07% Fe-0.05% Si-0.24% Mn with Si/Fe of 1 and Mn/Fe of 3.5. They also

found that β-Fe was the only iron-rich intermetallic phase. In the work of Kamga et al. [9],

β-Fe was reported to be the only iron-rich intermetallic phase in a 206 alloy with 0.11%

Fe-0.06% Si-0.23% Mn with Si/Fe and Mn/Fe ratios of 0.5 and 2.2, respectively. These

materials reported are typically 206 alloys with Fe, Si and Mn contents up to 0.11%, 0.1%

and 0.3%, respectively. Based on these data reviewed above, β-Fe is the dominant Fe-rich

phase for Si/Fe of 0.5–1.7 and Mn/Fe of 2.2–8.5. The full transformation from β-Fe into α-Fe appears at Mn/Fe and Si/Fe ratios up to 13 and 2, respectively.

In addition, increasing the cooling rate is also considered to be one of the efficient methods to hinder the formation of platelet iron-rich intermetallics. In the work of Kamga et al. [9, 87], they found that a moderate high cooling rate is helpful for the formation of Chinese script α-Fe in 206 cast alloys.

Furthermore, there is little literature on the effect of the iron-rich intermetallics on the mechanical properties in 206 cast alloy, especially at high iron content. Tseng et al. [13, 43] studied the effect of Fe on the mechanical properties of 206 cast alloy with 0.05-0.25% Fe and found that the tensile strength decreased linearly with increasing iron content. Kamga et al. [74] also investigated the mechanical properties of 206 cast alloy and found that it is hard to reach the 7% elongation at an iron content higher than 0.2% after solution and artificially aged (T7) while it is possible to extend the present limit of 0.1% Fe up to 0.3% in solution and natural aging condition (T4) to meet the industrial requirements. Sigworth et al. [88] has studied the factors influencing the mechanical properties of the 206 cast alloy and found that Fe and Mn will decrease the properties in T4 condition while Fe, Mn, Mg and Si all reduce them in the T7 condition. However, the iron content is limited to

0.05%-0.3% and the effects of Mn and Si on the mechanical properties were seldom discussed.

Therefore, it is necessary and important to systematically investigate the solidification behaviors of the iron-rich intermetallics and the effects of the addition of neutralization elements such as Mn and/or Si, cooling rate and heat treatment on the formation of the iron-rich intermetallics as well as the effect of the iron-rich intermetallics on the tensile properties in Al-Cu 206 cast alloy, especially at high iron content.

References

[1] K. Yu, S. Li and W. Li: *Rare Met. Mater. Eng.*, 2000, Vol. 29, pp. 177-181.

[2] J. H. Wang, D. Q. Yi, Y. Cao, K. H. Cheng, H. W. Liu, B. Wang, B. Lu and S. Liu: *IJMMME*, 2001, Vol. 25, pp. 8-15.

[3] N. P. Lyakishev, Mashinostroenie, Moscow, Russia, 1996.

[4] M. L. Philbin: *MODERN CASTING*, 1996, Vol. 86, pp. 30-33.

[5] Q. G. Wang and C. J. Davidson: *J. Mater. Sci.*, 2001, Vol. 36, pp. 739-750.

[6] J. Y. Hwang, H. W. Doty and M. J. Kaufman: *Mater. Sci. Eng., A*, 2008, Vol. 488, pp. 496-504.

[7] L. Lu and A. K. Dahle: *Metall. Mater. Trans. A*, 2005, Vol. 36, pp. 819-835.

[8] N. A. Belov, A. A. Aksenov and D. G. Eskin, *Iron in aluminum alloys: impurity and alloying element*, Taylor & Francis, London, 2002.

[9] H. Kamguo Kamga, D. Larouche, M. Bournane and A. Rahem: *Metall. Mater. Trans. A*, 2010, Vol. 41, pp. 2844-2855.

[10] A. Couture: *Int. Cast Met. J.*, 1981, Vol. 6, pp. 9-17.

[11] L. F. Mondolfo, *Aluminum alloys: Structure and properties*, Butterworths, London, 1976.

[12] J. E. Hatch, *Aluminum: properties and physical metallurgy*, American Society for Metals, Metals Park, Ohio, 1984.

[13] C. J. Tseng, S. L. Lee, T. F. Wu and J. C. Lin: *Mater. Trans., JIM*, 2000, Vol. 41, pp. 708-713.

[14] G. Atxaga, A. Pelayo and A. M. Irisarri: *Mater. Sci. Technol.*, 2001, Vol. 17, pp. 446-450.

[15] Y. H. Tan, S. L. Lee and H. Y. Wu: *Int. J. Fatigue*, 1996, Vol. 18, pp. 137-147.

[16] Y. H. Tan, S. L. Lee and Y. L. Lin: *Metall. Mater. Trans. A*, 1995, Vol. 26, pp. 2937-2945.

[17] Y. Wang and Y. Xiong: *Mater. Sci. Eng., A*, 2000, Vol. 280, pp. 124-127.

[18] S. Murali, K. S. Raman and K. S. S. Murthy: *Mater. Sci. Forum*, 1996, Vol. pp. 207-222.

[19] X. Cao and J. Campbell: *Can. Metall. Q.*, 2005, Vol. 44, pp. 435-448.

[20] X. Cao and J. Campbell: *Metall. Mater. Trans. A*, 2003, Vol. 34, pp. 1409-1420.

[21] X. Cao and J. Campbell: *Metall. Mater. Trans. A*, 2004, Vol. 35 A, pp. 1425-1435.

[22] X. Cao and J. Campbell: *Mater. Trans., JIM*, 2006, Vol. 47, pp. 1303-1312.

[23] A. C. Venetti, *Progress in materials science research*, Nova Science Publishers, New York, 2008.

[24] D. N. Miller, L. Lu and A. K. Dahle: *Metall. Mater. Trans. B*, 2006, Vol. 37, pp. 873-878.

[25] Q. G. Wang, D. Apelian and D. A. Lados: *J. Light Met.*, 2001, Vol. 1, pp. 85-97.

[26] S. G. Shabestari and J. E. Gruzleski: *Metall. Mater. Trans. A*, 1995, Vol. 26, pp. 999-1006.

[27] X. Cao, N. Saunders and J. Campbell: *J. Mater. Sci.*, 2004, Vol. 39, pp. 2303-2314.

[28] C. Unuvar, D. M. Fredrick, U. Anselmi-Tamburini, B. D. Shaw, A. Manerbino, J. Y. Guigne and Z. A. Munir: *Acta Mater.*, 2007, Vol. 55, pp. 2965-2975.

[29] Y. M. Liu, L. S. Yang, Q. Xia and D. X. Yang: *Journal of Luoyang Institute of Technology*, 1999, Vol. 20, pp. 55-58.

[30] H. Matsubara, N. Izawa and M. Nakamsbi: *Light metals*, 1998, Vol. 48, pp. 93-95.

[31] W. B. Fang, Y. H. Geng and R. M. Ye: *Foundry Technology*, 1996, Vol. 2, pp. 42-44.

[32] L. Zhang and W. Jiao: *Tezhong Zhuzao Ji Youse Hejin/Special Casting and Nonferrous Alloys*, 2006, Vol. 26, pp. 5-7.

[33] A. M. Samuel, A. Pennors, C. Villeneuve, F. H. Samuel, H. W. Doty and S. Valtierra: *Int. J. Cast Met. Res.*, 2000, Vol. 13, pp. 231-253.

[34] S. Belmares-Perales, M. Castro-Román, M. Herrera-Trejo and L. E. Ramirez-Vidaurri: *Met. Mater. Int*, 2008, Vol. 14, pp. 307-314.

[35] G. Gustafsson, T. Thorvaldssons and G. L. Dunlop: *Metall. Mater. Trans. A*, 1986, Vol. 17 A, pp. 45-52.

[36] G. K. Sigworth, S. Shivkumar and D. Apelian: *AFS Trans.*, 1989, Vol. 97, pp. 811-824.

[37] O. Vorren, J. E. Enenson and T. B. Pederson: *AFS Trans.*, 1984, Vol. pp. 459-466.

[38] P. Ashtari, H. Tezuka and T. Sato: *Mater. Trans., JIM*, 2003, Vol. 44, pp. 2611-2616.

[39] L. A. Narayanan, F. H. Samuel and J. E. Gruzleski: *Metall. Mater. Trans. A*, 1994, Vol. 25, pp. 1761-1773.

[40] A. N. Lakshmanan, S. G. Shabestari and J. E. Gruzleski: *Mater. Res. Adv.Tech.*, 1995, Vol. 86, pp. 457-464.

[41] S. G. Shabestari, M. Mahmudi, M. Emamy and J. Campbell: *Int. J. Cast Met. Res.*, 2002, Vol. 15, pp. 17-24.

[42] C. J. Tseng, S. L. Lee, S. C. Tsai and C. J. Cheng: *J. Mater. Res.* , 2002, Vol. 17, pp. 2243-2250.

[43] C. J. Tseng, Ph. D thesis, Engeering college, National Central University Taiwan, China, 2003.

[44] F. H. Samuel, P. Ouellet, A. M. Samuel and H. W. Doty: *Metall. Mater. Trans. A*, 1998, Vol. 29, pp. 2871-2884.

[45] H. Zak and B. Tonn: *International Aluminum Alloy Conference*, German, 2008, pp. 279-284.

[46] D. G. Rathindra: *Die casting engineer*, 1996, Vol. pp. 65-67.

[47] S. G. Shabestari: *AFS Trans.*, 1995, Vol. 26, pp. 285-293.

[48] A. M. Samuel, F. H. Samuel and H. W. Doty: *J. Mater. Sci.*, 1996, Vol. 31, pp. 5529-5539.

[49] J. Espinoza-Cuadra, P. Gallegos-Acevedo, H. Mancha-Molinar and A. Picado: *Mater. Des.*, 2010, Vol. 31, pp. 343-356.

[50] X. Cao and J. Campbell: *Mater. Sci. Technol.*, 2004, Vol. 20, pp. 514-520.

[51] L. V. Olivante, Nova Science Publishers, New York, 2008.

[52] P. N. Crepeau: *Mater. Eng.*, Georgia Institute of Technology, USA, 1989.

[53] S. Nishi and T. Shinoda: *Metals Abstracts*, 1969, Vol. 2.

[54] S. Gowri and F. H. Samuel: *Metall. Mater. Trans. A*, 1994, Vol. 25, pp. 437-448.

[55] D. A. Granger, R. R. Sawtell and M. M. Kersker: *AFS Transction*, 1984, Vol. 115, pp. 579-586.

[56] E. KATO and S. MURAKAWA: *Casting*, 1994, Vol. 66, pp. 10-14.

[57] S. Murali, T. N. G. Row, D. H. Sastry, K. S. Raman and K. S. S. Murthy: *Scripta Metall. Mater.*, 1994, Vol. 31, pp. 267-271.

[58] S. Murali, K. S. Raman and K. S. S. Murthy: *Mater. Sci. Eng., A*, 1995, Vol. 190, pp. 165-172.

[59] S. Murali, K. S. Raman and K. S. S. Murthy: *AFS Transactions*, 1996, Vol. 104, pp. 1175-1181.

[60] D. N. Khudokormov, A. M. Galashko and S. N. Lekakd: *Russian Casting Production*, 1975, Vol. 5, pp. 198-199.

[61] H. L. Zhu, J. Jia and X. F. Bian: *Special casting and non-ferrous Metals*, 1996, Vol. 4.

[62] Z. F. Li, R. Y. Zhang and D. Mei: *Journal of Inner Mongolia University of Technology*, 2004, Vol. 23, pp. 209-212.

[63] X. F. Liu and X. F. Bian: *Special Casting and Non-ferrous Metals*, 1994, Vol. 5, pp. 13-16.

[64] X. Liu, X. Bian, Y. Liu, G. Zhang and J. Ma: *Jinshu Xuebao/Acta Metallurgica Sinica*, 1997, Vol. 33, pp. 1068.

[65] X. Cao and J. Campbell: *Int. J. Cast Met. Res.*, 2003, Vol. 15, pp. 595-608.

[66] L. Zhang, W. L. Jiao, H. J. Yu and G. C. Yao: *Zhongguo Youse Jinshu Xuebao/Chinese Journal of Nonferrous Metals*, 2005, Vol. 15, pp. 368-373.

[67] L. Zhang: *Technology of Light Metals*, 2007, Vol. 35, pp. 20-23.

[68] S. Nafisi, D. Emadi, M. T. Shehata and R. Ghomashchi: *Mater. Sci. Eng., A*, 2006, Vol. 432, pp. 71-83.

[69] X. F. Bian, G. H. Zhang and S. X. Zhao: *Special Casting and Non-ferrous Metals*, 1992, Vol. 4, pp. 19-25.

[70] Y. Awano and Y. Schimizu: *AFS Transction*, 1990, Vol. 176, pp. 889-896.

[71] Y. M. Sun and J. Y. Qin: *Shandong Metallurgy*, 2008, Vol. 30, pp. 35-36.

[72] Z. P. Zhou, J. C. Ma, Y. H. Bai, H. P. Yu and R. D. Li: *Foundry* 2002, Vol. 51, pp. 343-345.

[73] A. Griger, V. Stefaniay, A. Lendvai and T. Turmezey: *Aluminium*, 1989, Vol. pp. 1049-1056.

[74] H. K. Kamga, D. Larouche, M. Bournane and A. Rahem: *Int. J. Cast Met. Res.*, 2012, Vol. 25, pp. 15-25.

[75] L. A. Narayanan, F. H. Samuel and J. E. Gruzleski: *Metall. Mater. Trans. A*, 1995, Vol. 26, pp. 2161-2174.

[76] R. Q. Liu, X. W. Jia, J. M. Liu, L. Q. Yang and S. J. Yang: *Special casting and non-ferrous Metals*, 2001, Vol. 2, pp. 107-108.

[77] Aluminum Association, *Designations and chemical composition limits for aluminum alloys in the form of castings and ingot*, Aluminum Association, Arlington, VA, 2009.

[78] L. Bäckerud, *Solidification characteristics of aluminum alloys*, Skanaluminium, Universitetsforlaget AS, Oslo, Norway, 1986.

[79] M. Talamantessilva, A. Rodriguez, J. Talamantessilva, S. Valtierra and R. Colas: *Mater. Charact.*, 2008, Vol. 59, pp. 1434-1439.

[80] C. A. Aliravci and M. O. Pekguleryuz: *Calphad*, 1998, Vol. 22, pp. 147-155.

[81] C. M. Allen, K. A. Q. O'Reilly, B. Cantor and P. V. Evans: *Prog. Mater. Sci.*, 1998, Vol. 43, pp. 89-170.

[82] X. G. Chen: *Light Metals*, Minerals, Metals & Materials Soc (TMS), San Antonio, TX, USA, 1998, pp. 1071-1076.

[83] Y. J. Li and L. Arnberg: *Acta Mater.*, 2004, Vol. 52, pp. 2673-2681.

[84] P. Skierpe: *Acta Cryst.*, 1988, Vol. B44, pp. 480-486.

[85] P. Gilgien, A. Zryd and W.Kurz: *Acta Metall. Mater.*, 1995, Vol. 43, pp. 3477-3487.

[86] W. Khalifa, F. H. Samuel and J. E. Gruzleski: *Metall. Mater. Trans. A*, 2003, Vol. 34, pp. 807-825.

[87] H. Kamguo Kamga, D. Larouche, M. Bournane and A. Rahem: *Mater. Sci. Eng., A*, 2010, Vol. 527, pp. 7413-7423.

[88] G. K. Sigworth and J. Fred Major: *Light Metals*, Minerals, Metals & Materials Soc (TMS), San Antonio, TX, 2006, pp. 795-799.

CHAPTER 3
EXPERIMENTAL

Chapter 3

Experimental

3.1 Experimental alloy design and sample preparation

There are two main parts in the investigation. In part I, the effects of alloy compositions (i.e. Fe, Mn and Si contents) and cooling rates on the solidification characteristics of the iron-rich intermetallics were studied. A series of 206 cast Al-Cu alloys with various levels of Fe, Mn and Si were cast in different molds to obtain various cooling rates. In part II, the influences of heat treatment on the solid-state transformation of the iron-rich intermetallics and alloy compositions on the mechanical properties were investigated. Two or Three alloys with different compositions at each iron contents were selected to perform the heat treatment to investigate their effect on the mechanical properties. The experimental details were described as follows:

3.1.1 Alloys for Part I: effect of alloy compositions and cooling rates on the solidification of iron-rich intermetallics

In this part, the experimental alloys with various compositions (i.e. Fe, Mn, and Si contents) were cast in different molds to obtain various cooling rates. The level of Fe was from 0.15% to 0.50% while both Mn and Si varied from 0.10% to 0.50%. Commercially

pure Al (99.7%) and pure Mg (99.9%), Al-50% Cu, Al-25% Fe, Al-50% Si and Al-25%

Mn master alloys were used to prepare the experimental alloys. Tables 3.1-3.3 show the

chemical compositions of the designed alloys used in this project.

Table 3.1 Chemical compositions of the designed alloys at 0.15% Fe used in the work

Alloy #	Elements (wt. %)					
	Cu	Fe	Mn	Si	Mg	Al
1	4.59	0.15	0.11	0.09	0.27	Bal.
2	4.58	0.16	0.21	0.11	0.29	Bal.
3	4.61	0.14	0.49	0.11	0.31	Bal.
4	4.59	0.16	0.11	0.18	0.27	Bal.
5	4.62	0.16	0.09	0.48	0.28	Bal.
6	4.64	0.17	0.21	0.19	0.27	Bal.
7	4.58	0.14	0.28	0.31	0.29	Bal.

Table 3.2 Chemical compositions of the designed alloys at 0.3% Fe used in the work

Alloy #	Element (wt. %)						
	Cu	Mg	Fe	Si	Mn	Ti	Al
1	4.46	0.27	0.33	0.08	0.11	0.02	Bal.
2	4.48	0.31	0.31	0.21	0.19	0.02	Bal.
3	4.51	0.32	0.32	0.31	0.31	0.02	Bal.
4	4.45	0.29	0.31	0.11	0.19	0.02	Bal.
5	4.52	0.28	0.29	0.11	0.41	0.02	Bal.
6	4.51	0.29	0.29	0.19	0.09	0.02	Bal.
7	4.59	0.31	0.31	0.31	0.11	0.02	Bal.

Table 3.3 Chemical compositions of the designed alloys at 0.5% Fe used in the work

Alloy #	Elements (wt. %)						
	Cu	Mg	Fe	Si	Mn	Ti	Al
1	4.58	0.28	0.51	0.07	0.003	0.01	Bal.
2	4.60	0.32	0.49	0.09	0.11	0.01	Bal.
3	4.61	0.32	0.49	0.19	0.22	0.01	Bal.
4	4.65	0.30	0.51	0.31	0.30	0.01	Bal.
5	4.62	0.28	0.50	0.48	0.10	0.01	Bal.
6	4.59	0.30	0.52	0.49	0.51	0.01	Bal.
7	4.68	0.31	0.51	0.11	0.53	0.01	Bal.

In each test, approximately 3 kg material was prepared in a clay-graphite crucible using an electric resistance furnace. The temperature of the melt was maintained at ~1023 K (750 °C) for 30 minutes and gently stirred to homogenize the molten metal and avoid entrainment of any surface oxide films. Then it was cast into a small preheated stainless steel crucible coated with a BN aerosol for Thermal Analysis (TA). Fig. 3.1 shows the schematic illustration of the thermal analysis setup and the size of the crucible used. This setup is designed to obtain various cooling rates through spraying with compressed air at different flow rates and pressures to obtain the different cooling rates (0.2 K/s, 1.4 K/s, 2.0 K/s). During the cooling, two K-type thermocouples (Chromel-alumel) were positioned in both the center and the near-wall regions of the crucible to measure the temperature. The temperature-time data were recorded by a data acquisition system (National Instruments NI SCXI-1531).
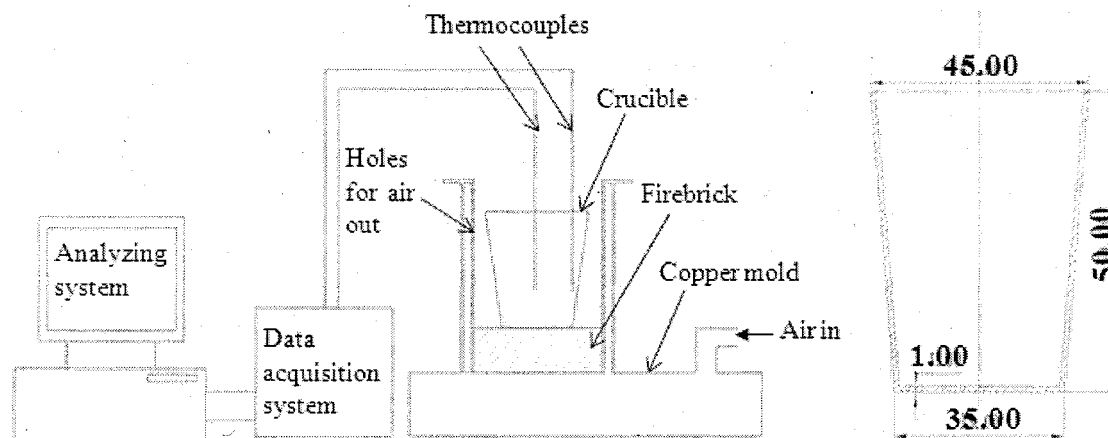
Fig. 3.1 Schematic illustration of the thermal analysis setup (a)
and the stainless steel crucible (b) (all dimensions in mm)

To obtain higher cooling rates, the samples were cast into a wedge shaped copper

mold which was coated using a BN aerosol and preheated to 523 K (250 °C). The

schematic illustration of the wedge shape copper mold is shown in Fig. 3.2. Three K-type

thermocouples were located in positions A, B and C to record the time and temperature.

The cooling rates in positions A, B and C calculated over the solidification interval are 3.5

K/s, 5.0 K/s and 7.5 K/s, respectively. In the present work, all the cooling rates were

calculated based on the temperature difference over the solidification interval.

After the solidification, the samples were sectioned, mounted and polished for the

metallographic observations. In order to observe clearly the oxide films in the Fe

intermetallics and Al matrix, magnesia powder with an average size of 0.05 μm was used to

finally produce a mirror surface finish [1]. Additionally, some metallographic specimens

were deeply etched in a 10% NaOH solution at 333~338 K (60~65 °C) for 1-1.5 minutes to

reveal the three-dimensional morphologies of the intermetallic phases.
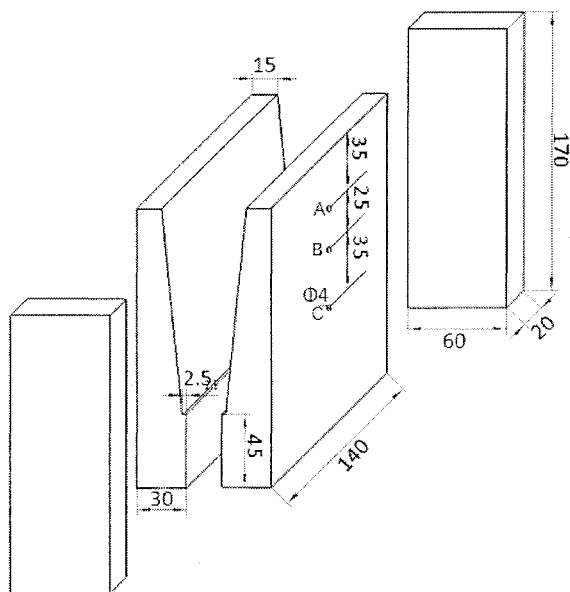
Fig. 3.2 Schematic illustration of the wedge shaped copper mold (all dimensions in mm)

3.1.2   Alloys for Part II: tensile property testing

In this part, two or three alloys with various Mn and Si levels at each iron content

were cast for the tensile test bars. Table 3.4 shows the chemical compositions of the

experimental alloys used for tensile testing in this project. The contents of Cu and Mg were

about 4.6 wt. % and 0.3 wt. %, respectively. In each test, approximately 30 kg material was

prepared in a clay-graphite crucible using an electric resistance furnace. The temperature of

the melt was maintained at ~1023 K (750 °C) for 30 minutes and gently stirred to

homogenize the molten metal and avoid entrainment of any surface oxide films. Then it

was cast into a standard ASTM B-108 permanent mold for tensile test bars [2]. Fig. 3.3

shows the standard ASTM B-108 permanent mold and casting samples.

Table 3.4 Chemical compositions of the alloys used for tensile testing

Alloys	Elements（wt. %)						
	Cu	Mg	Fe	Si	Mn	Ti	Al
B11	4.64	0.27	0.14	0.12	0.12	0.21	Bal.
B33	4.61	0.29	0.16	0.29	0.32	0.21	Bal.
311	4.66	0.27	0.30	0.11	0.12	0.19	Bal.
333	4.62	0.28	0.29	0.29	0.33	0.19	Bal.
511	4.69	0.29	0.51	0.11	0.11	0.20	Bal.
515	4.68	0.29	0.49	0.09	0.51	0.18	Bal.
533	4.64	0.28	0.49	0.30	0.31	0.19	Bal.

Fig. 3.3 Standard ASTM B-108 permanent metal mold (a) and cast samples (b)

For each alloy in part I and part II, two coins were cast for the chemical analysis. Fig.

3.4 shows the coin mold and the castings for chemical analysis.
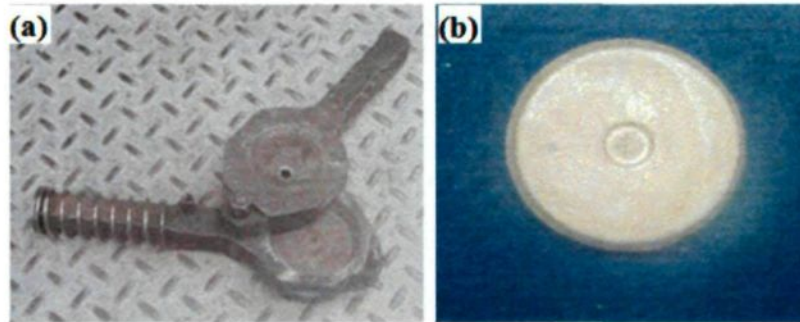
Fig. 3.4 Coin old (a) and the castings (b) used for chemical analysis

3.2 Heat treatment

The castings were cut into tensile test bars and then loaded into the furnace at room temperature for the following solution treatment:

(1) ramping up from room temperature to 505 °C in 1.5 hours;

(2) holding at 505 °C for 2 hours;

(3) ramping up from 505 °C to 525 °C in 0.5 hour;

(4) holding at 525 °C for 2, 8, 12 and 24 hours, respectively; and

(5) quenching into 65 °C hot water.

For the aging treatment, T4 (natural aging) and T7 (over aging) were performed in this project:

T4 -naturally aged for 7 days at room temperature in air after solution treatment; and

T7-artificially aged in the furnace after solution treatment in the following procedures:

(1) ramping up from room temperature to 180 °C in 1 hour;

(2) holding at 180 °C for 5 hours; and

(3) air cooling to room temperature.

3.3 Microstructure observation

3.3.1   Optical Microscopy (OM)

Optical microscopy (Nikon Eclipse ME600, as shown in Fig. 3.5a) was used to examine the microstructures of the experimental alloys in both as-cast and heat treated conditions. The samples were mounted and metallographically polished down to 0.05 micron diamond suspension. The image analyzer equipped with optical microscopy was used to measure the size, distribution and volume fraction of the iron-rich intermetallics.

3.3.2   Differential Scanning Calorimeter (DSC)

A Differential Scanning Calorimeter (DSC) (DSC, Perkin Elmer DSC 8000, as shown in Fig. 3.5b) was used to identify and confirm the solidification and the type of the iron-rich intermetallics during the solidification the heat treatment process

The samples were ground about 1 mm in depth and pounced into a plate with a diameter of 3 mm. The weight of each sample is about 15-25 mg. Then the sample was loaded into a DSC chamber to perform the DSC experiments.

The heating and cooling rates were set at 10 K/min during the DSC testing. In addition, extra DSC analyses at cooling rates of 1 K/min, 5 K/min and 50 K/min were also carried out to investigate the phase selection of the iron-rich intermetallics during solidification in alloys at 0.5% Fe.

3.3.3   Scanning electron microscopy (SEM)

A scanning electron microscope (SEM, JSM–6480LV, as shown in Fig. 3.5c) equipped with energy-dispersive X-ray spectroscopic (EDS) facilities was used to identify the iron-rich intermetallics and quantify the alloying elements in their on-rich intermetallics. To reveal a three-dimensional morphology of the phase constituents, some metallographic samples were deeply etched with 2.5% HF for 10 minutes. In addition, SEM was also performed to investigate the fracture surface after the tensile testing. The fracture surface was cut from the tensile testing bar with a height of 1.5cm under protection to avoid the contamination.

3.3.4 Electron backscatter diffraction (EBSD)

EBSD was used to further identify and confirm the types of the iron-rich intermetallics. The specimens for EBSD analysis were the same as those used in the SEM-EDS analysis. An HKL Channel 5 EBSD system equipped on the SEM (JSM–6480LV) was employed for this investigation.

3.3.5 Transmission electron microscopy (TEM)

Specimens for TEM observation were prepared in order to identify the iron-rich intermetallics, and measure their compositions and distribution of the elements in iron-rich intermetallics. The samples were prepared in a Focus Ion Beam (FIB) workstation in École Polytechnique de Montréal.

TEM samples were examined in a JEM–2100 electron microscope equipped with an EDS system at 200 kV, as shown in Fig. 3.5d. The selected area diffraction patterns (SADPs) were captured and indexed to confirm the iron-rich intermetallics in micro-scale. Both the dark and bright field images were taken to study the detail in the iron-rich intermetallics. In addition, TEM-EDS was performed to measure the compositions of the iron-rich intermetallics and distribution of elements in these iron-rich intermetallics.
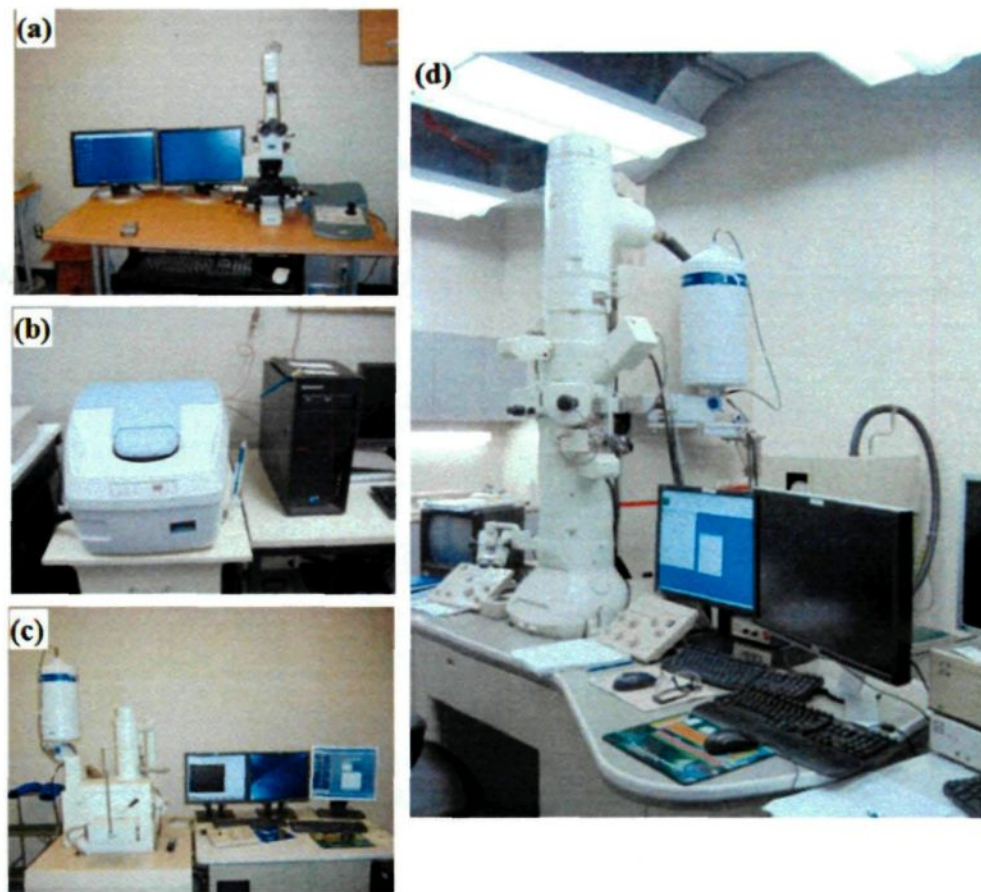
Fig. 3.5 Experimental equipment used in this work
(a) Optical microscope, (b) Differential Scanning Calorimeter (DSC),
(c) Scanning electron microscopy (SEM),
and (d) Transmission electron microscopy (TEM)

3.4 Evaluation of mechanical properties-tensile testing

The tensile testing bars were solidified in the permanent mold (Fig. 3.3) at a cooling

rate of 2-3 K/s. Then the tensile testing bars were performed the T4 and T7 heat treatment,

as mentioned in 3.2. After aging treatment, the bars were machined according to ASTM E8/E8M standards [3] after aging treatment to avoid the hot tearing in the connection part. The machined bars were taken from the center part of the origin tensile testing bars. The tensile test bar before and after machining is shown in Fig. 3.6a while the size of bars after machining was shown in Fig. 3.6b.

The tensile testing was performed on the heat treated testing bars at room temperature at a cross head speed of 0.5 mm/min by using a 100 kN capacity electromechanical testing machine (Instron 8801 tensile test system, as shown in Fig. 3.7). During the testing, an extensometer with a gauge length of 25 mm was attached to the testing bars to measure the displacement. Both the yield strength (YS) and ultimate tensile strength (UTS) were obtained from the data acquisition system of the tensile test machine. The YS was computed at 0.2% offset strain and UTS at the maximum stress. For each alloy, the average values of YS, UTS and elongation were obtained from 6 tests.
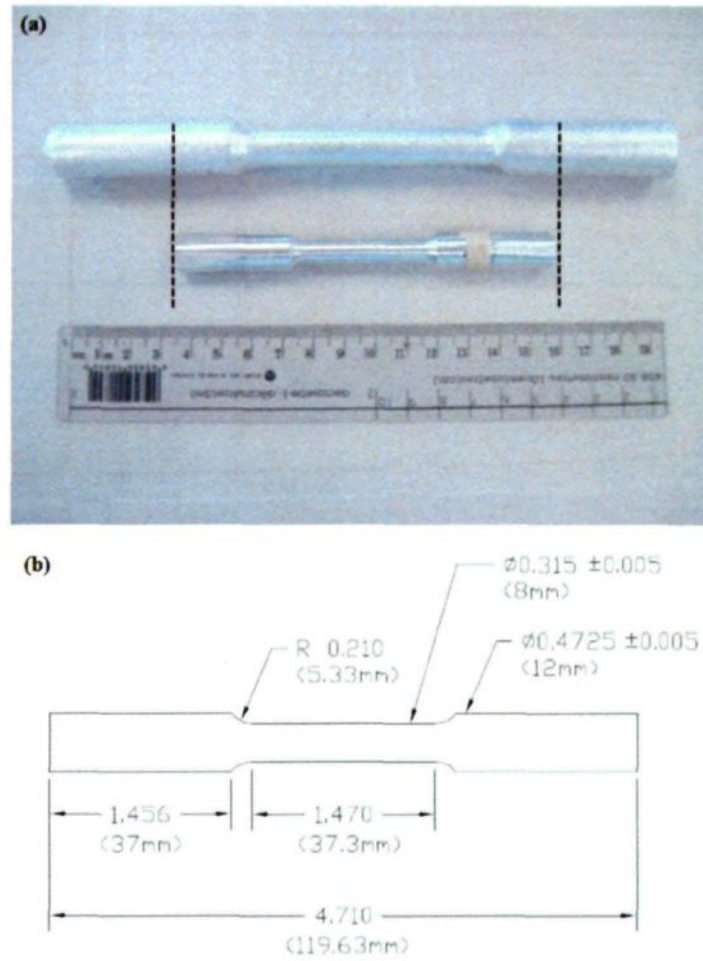
Fig. 3.6 Original cast bars and machined tensile test bars (a) and dimensions of tensile

test bars after machining (b) (unit in inch unless indicated otherwise)

Fig. 3.7 Instron 8801 tensile test system

References

[1] X. Cao and J. Campbell: *Metall. Mater. Trans. A*, 2004, Vol. 35 A, pp. 1425-1435.

[2] American Society for Testing Materials, *ASTM standards on light metals and alloys. Aluminum and aluminum alloys, cast and wrought; magnesium and magnesium alloys, cast and wrought; methods of testing light metals*, American Society for Testing Materials, Philadelphia, 1959.

[3] ASTM International, *Standard test methods for tension testing of metallic materials*, ASTM, West Conshohocken, Pa, 2009.

CHAPTER 4

IRON-RICH INTERMETALLICS

IN 206 CAST ALLOYS AT 0.15% FE

Chapter 4

Iron-rich intermetallics in 206 cast alloys at 0.15% Fe

4.1 Introduction

As reviewed in the introduction and literature review section, some neutralization elements and cooling rate play significant roles in the formation of the iron-rich intermetallics.

Adding the neutralization elements, such as Mn and/or Si [1-5] is one of the most widely used methods to modify the platelet-like iron-rich intermetallics. It was reported that the Mn/Fe and Si/Fe ratios were critical for the efficient transformation of platelet β-Fe into Chinese script α-Fe [5]. The critical Mn/Fe and Si/Fe ratios, at which the platelet β-Fe can be completely transformed to Chinese script α-Fe, vary with the Fe level. However, the thresholds of Mn/Fe and Si/Fe ratios have not well been established for the commercial Al-Cu cast alloys with lower iron level than 0.15%. As early as 1980's, Backerud et al. [6] have studied the solidification path of 206 cast alloy with   0.03% Fe-0.05% Si-0.26% Mn and found that β-Fe is the only iron-rich intermetallics in this alloy although the Si/Fe and

Mn/Fe ratios were as high as 1.7 and 8.5., respectively. In the study of Tseng *et al.* [4, 7], β-Fe was also reported to be the dominant iron-rich intermetallics in 206 family cast alloy with 0.05% Fe-0.01% Si-0.3% Mn and the β-Fe could almost be completely transformed to Chinese script when Mn was added up to 0.66%, in which the Mn/Fe ratio was as high as 13. Talamantes-Silva *et al.* [8] have studied the characterization of a 206 cast alloy with 0.07% Fe-0.05% Si-0.24% Mn with Si/Fe of 1 and Mn/Fe of 3.5. They also found that β-Fe was the only one iron-rich intermetallic phase. In the work of Kamga *et al.* [1], β-Fe was reported to be the only iron-rich intermetallic phase in a 206 alloy with 0.11% Fe-0.06% Si-0.23% Mn with Si/Fe and Mn/Fe of 0.5 and 2.2, respectively. These materials reported are typical 206 alloys with Fe, Si and Mn contents up to 0.11%, 0.1% and 0.3%, respectively. Based on these data reviewed above, β-Fe is the dominant Fe-rich phase for Si/Fe of 0.5–1.7 and Mn/Fe of 2.2–8.5. The full transformation from β-Fe into α-Fe appears at Mn/Fe and Si/Fe ratios up to 13 and 2, respectively.

In addition, increasing the cooling rate [9-11] is also considered to be one of the efficient methods to hinder the formation of platelet iron-rich intermetallics in Al-Si cast alloys. However, litter work about the effect of cooling rate on the formation of iron-rich intermetallics has been reported in Al-Cu 206 cast alloys.

To better control the microstructures and optimize the mechanical properties, the solidification of the iron-rich intermetallics and the effects of the individual and combined additions of Mn and/or Si as well as the cooling rate on the formation of the iron-rich intermetallics for 206 cast alloys at a maximum tolerable iron level of 0.15% Fe will be dealt with in this section.

The chemical compositions of the experimental alloys used in this part are listed in Table 4.1. In order to cast the experimental alloys at various cooling rates, two methods have been used. One was to pour the molten metal into a small preheated stainless steel crucible which was coated using a BN aerosol. Then the samples were solidified to room temperature in compressed air with various pressures to achieve at different cooling rates (0.2 K/s, 1.4 K/s and 2.0 K/s), as shown in Fig. 3.1. The other method for a higher cooling rate was to cast the samples into a wedge shaped copper mold which was also coated using a BN aerosol and preheated to 523 K (250 °C). The schematic illustration of the wedge shape copper mold is shown in Fig. 3.2. Three K-type thermocouples were located in positions A, B and C to record the time and temperature. The cooling rates in positions A, B and C calculated over the solidification interval are 3.5 K/s, 5.0 K/s and 7.5 K/s, respectively.

OM and SEM were used to observe the microstructures and identify the iron-rich

intermetallics while TA and DSC were performed to distinguish and confirm the

solidification sequences of iron-rich intermetallics. Details of solidification and

experimental methods can be found in Chapter 3

Table 4.1 Chemical compositions of the experimental alloys at 0.15% Fe

Alloy #	Elements (wt. %)					
	Cu	Fe	Mn	Si	Mg	Al
Standard 206.0*	4.2-5	0.15 max	0.2-0.5	0.1 max	0.15-0.35	Bal.
1	4.59	0.15	0.11	0.09	0.27	Bal.
2	4.58	0.16	0.21	0.11	0.29	Bal.
3	4.61	0.14	0.49	0.11	0.31	Bal.
4	4.59	0.16	0.11	0.18	0.27	Bal.
5	4.62	0.16	0.09	0.48	0.28	Bal.
6	4.64	0.17	0.21	0.19	0.27	Bal.
7	4.58	0.14	0.28	0.31	0.29	Bal.

* According to the Aluminum Association specification [12].

4.2 Iron-rich intermetallics and solidification reactions

To identify and confirm the iron-rich intermetallics, the combined use of both EDS

and EBSD on a SEM are performed, which can improve the phase identification by

collecting both chemical information from EDS and crystallography information from

EBSD [13]. The morphologies of two typical iron-rich intermetallics formed in the

experimental 206 cast alloys are shown in Fig. 4.1a and 4.1c while the EDS maps of the two iron-rich intermetallics are shown in Fig. 4.1b and 4.1d. The chemical compositions with one standard deviation obtained from EDS are shown in Table 4.2. According to the morphology and the atom ratio from the EDS results, as shown in Table 4.2, platelet A is probably $Al_7Cu_2(FeMn)$ (β-Fe) and Chinese script B is most likely $Al_{15}(FeMn)_3(SiCu)_2$ (α-Fe), which is similar to that reported in 206 type alloys at 0.3% Fe [2, 3].
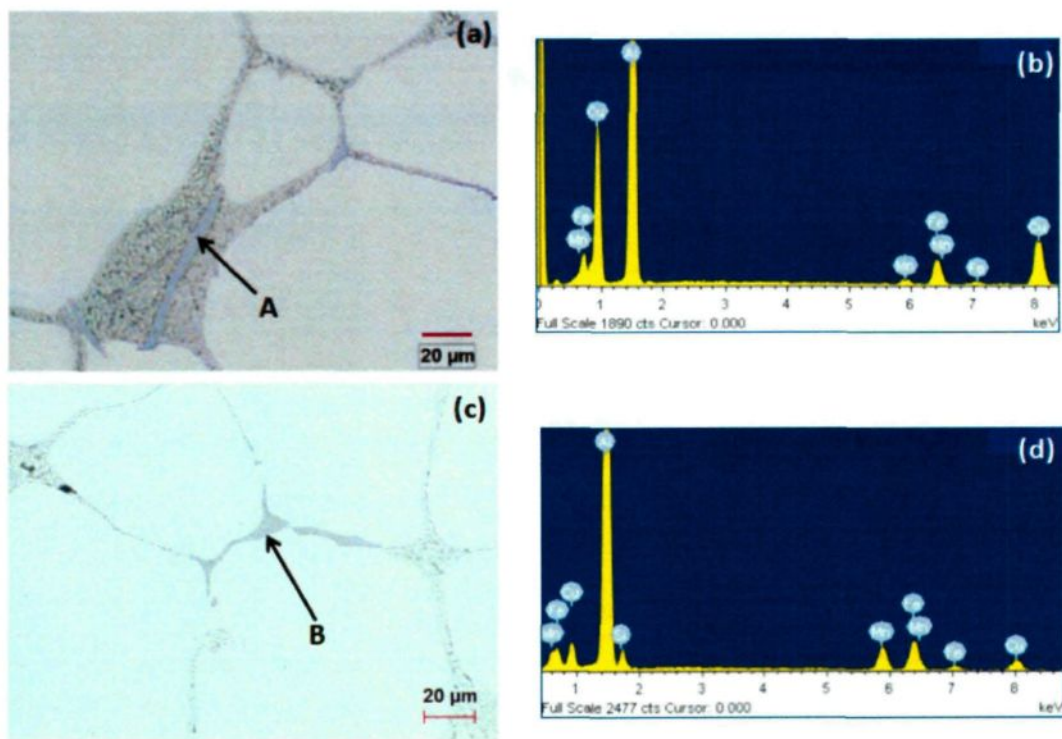
Fig. 4.1 Morphologies of two typical iron-rich intermetallics and their EDS results

Table 4.2 SEM-EDS results of the two iron-rich intermetallics shown in Fig. 4.1

Phase	Elements (at. %)					Al:(Fe+Mn):(Si+Cu)
	Al	Si	Mn	Fe	Cu	
A	70.58±0.68	0	1.51±0.28	8.51±0.23	19.5±0.65	7 : 1 : 2
B	74.78±0.62	5.31±0.32	6.15±0.34	8.76±0.24	5.01±0.48	15 : 3 : 2

The EBSD patterns and their simulation results of the two iron-rich intermetallics are shown in Fig. 4.2. Fig. 4.2b and Fig. 4.2e are the experimental EBSD patterns while Fig. 4.2c and Fig. 4.2f are the simulation results calculated by the Channel 5 software. In EBSD, the Mean Angular Deviation (MAD) between the experimental and calculated patterns represents the accuracy of the solution provided by the software, where a smaller value indicates a closer match between the experimental and simulated Kikuchi bands. Normally, a value for MAD, lower than 0.7, is considered desirable for an accurate solution [14]. As shown in Fig. 4.2, the MAD values are 0.129 and 0.254 for β-Fe and α-Fe, respectively, indicating that the accurate solutions are obtained for the two phases, confirming the presence of both β-Fe and α-Fe in the 206 cast alloy.
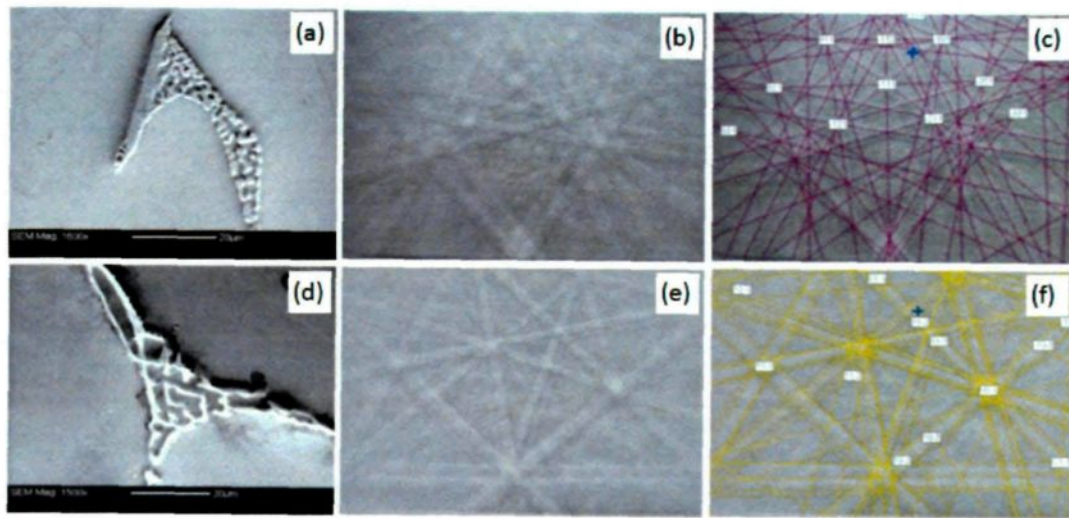
Fig. 4.2 Phase morphologies, EBSD patterns and simulation results for
(a-c) β-Fe (MAD = 0.129) and (d-f) α-Fe (MAD = 0.254)

TA and DSC were performed to detect the formation of the iron-rich intermetallics

during the solidification. Since the dominant iron-rich intermetallic phases are β-Fe for

Alloys 1, 2, and 4 but α-Fe for Alloys 3, 5-7, the results of Alloys 1 and 6 are mainly

presented and discussed, respectively for the β-Fe or α-Fe dominant materials. As an

example, the TA cooling curves of Alloys 1 and 6 solidified at 0.2 K/s are shown in Fig 4.3

while the corresponding DSC heating and cooling curves are shown in Fig. 4.4. It can be

found that there are 4 peaks in Alloy 1 with 0.1% Si and 0.1% Mn while 5 peaks are

present in Alloy 6 with 0.2% Si and 0.2% Mn in both the TA and DSC curves, indicating

that the formation of iron-rich intermetallics varies with alloy compositions. According to

the metallographic observations in this study combined with the reactions reported in

literatures [2, 3, 6], the iron-rich intermetallics precipitated in Peak 2-4 for the experimental

alloys investigated.
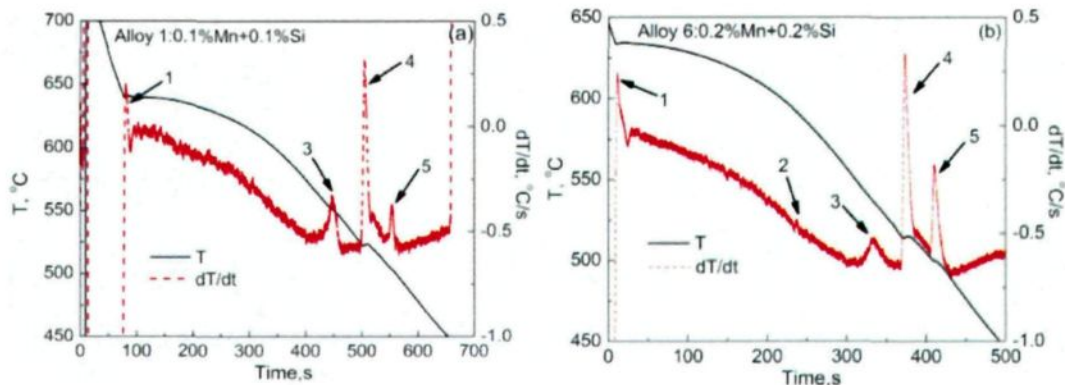
Fig. 4.3 TA cooling curves of Alloys 1 (a) and 6 (b)
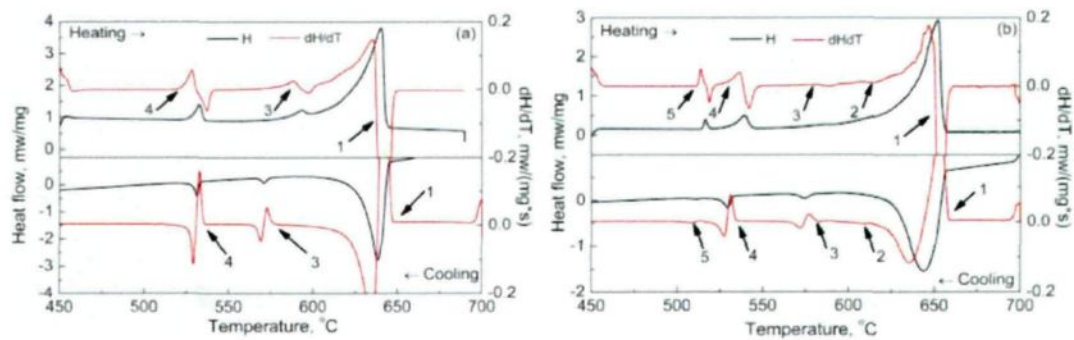
Fig. 4.4 DSC heating and cooling curves of Alloys 1(a) and 6 (b)

In order to clarify the solidification reactions and sequence as well as the resultant

precipitation of iron-rich intermetallics, the interrupt water quenching technique was

carried out and the microstructures of Alloys 1 and 6 quenched at different temperatures

(after Peaks 1, 2 and 3) are shown in Fig. 4.5 and Fig. 4.6, respectively. It is determined

that Al_6(FeMnCu) is present in Alloy 1 with 0.1% Si and 0.1% Mn when water quenched at

893 K (620 °C) and 873 K (600 °C) but Al$_6$(FeMnCu) disappears and β-Fe precipitates when water quenched at 823 K (550 °C), indicating the possibility of the peritectic formation of β-Fe from Al$_6$(FeMnCu). However, as shown in Fig. 4.6, for Alloy 6 with 0.2% Si and 0.2% Mn Al$_6$(FeMnCu) is the first iron-rich intermetallic phase to precipitate but α-Fe precipitates after water quenching at 873 K (600 °C) while both α-Fe and β-Fe coexist in the sample after water quenching at 823 K(550 °C).
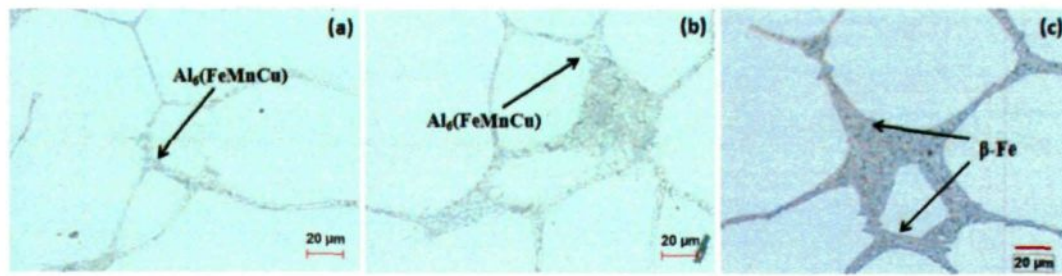
Fig. 4.5 Microstructures of Alloy 1 water quenching at
(a) 893 K (620 °C), (b) 873 K (600 °C) and (c) 823 K (550 °C)
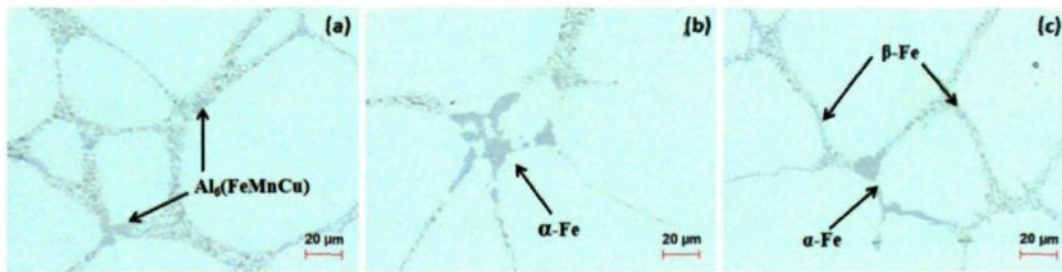
Fig. 4.6 Microstructures of Alloy 6 water quenching at
(a) 893 K (620 °C), (b) 873 K (600 °C) and (c) 823 K (550 °C)

Based on the present systematic metallographic observations with TA and DSC curves, as well as those reported by Backerud et al. [6] and Mondolfo [15], and the ternary

Al-Cu-Fe phase diagram [16], the possible solidification reactions and their sequence occurring in the present experimental alloys are listed in Table 4.3.

As shown in Table 4.3, it can be found that the solidification reactions are quite similar to those reported for 206 cast alloy at 0.3% Fe [3]. $Al_6(FeMnCu)$ is found to be the first iron-rich intermetallic phase to precipitate and then it transforms into α-Fe and/or β-Fe, depending on the compositions of the alloy. In addition, α-Fe can precipitate through the eutectic reaction as shown in Fig. 4.6b (i.e. Reaction 2b in Table 4.3) and β-Fe can precipitate through the peritectic reactions from $Al_6(FeMnCu)$ and α-Fe (i.e. Reactions 3a and 3b in Table 4.3). Additionally, it is also possible to form β-Fe through the eutectic reaction according to that reported in literature [17, 18], though metallographic evidence for this sequence is not observed in this study.

Table 4.3 Possible solidification reactions in experimental 206 cast alloys

Peak	Reactions	Suggested Temp. K (°C)*	Alloys
1	Aluminum dendrite network forms Liq.$\rightarrow$Al+Al_6(FeMnCu)	923~918 (650~645)	1-7
2**	a): Liq.+Al_6(FeMnCu)$\rightarrow$Al+α-Fe b): Liq.$\rightarrow$Al+α-Fe	893~883 (620~610)	3,5-7
3**	a): Liq.+Al_6(FeMnCu)$\rightarrow$Al+β-Fe b): Liq.+α-Fe$\rightarrow$Al+β-Fe c): Liq.$\rightarrow$Al+β-Fe	863~848 (590~575)	1-4,6
4	Liq.$\rightarrow$Al+Al_2Cu+$Al_{20}Mn_3Cu_2$+β-Fe	813~803 (540~530)	1-7
5	Liq.$\rightarrow$Al+Al_2Cu+Al_2CuMg+Mg_2Si	783~773 (510~500)	1-7

Notes: The peak numbers are corresponded to those as indicated in Figs. 4.3 and 4.4.
* Temperatures are determined from the DSC heating curves, which eliminate the

undercooling effect.

      ** Some reactions may depend on the alloy compositions, as discussed in the following subsection.

4.3   Effect of Mn and Si on the formation of iron-rich intermetallics

As shown in Figs. 4.3 and 4.4, it can be found that the number of peaks in Alloys 1 and 6 are different. In addition, the intensity of Peak 3 for Alloy 1 is higher than that for Alloy 6. Moreover, α-Fe has become the dominant iron-rich intermetallic phase in Alloy 6 as observed through the metallographic analysis. These phenomena indicate that the contents of Mn and/or Si influence the formation of the Fe-rich intermetallics. This has been further observed by the metallographs, as shown in Fig. 4.7 that presents all the samples solidified at 0.2 K/s.
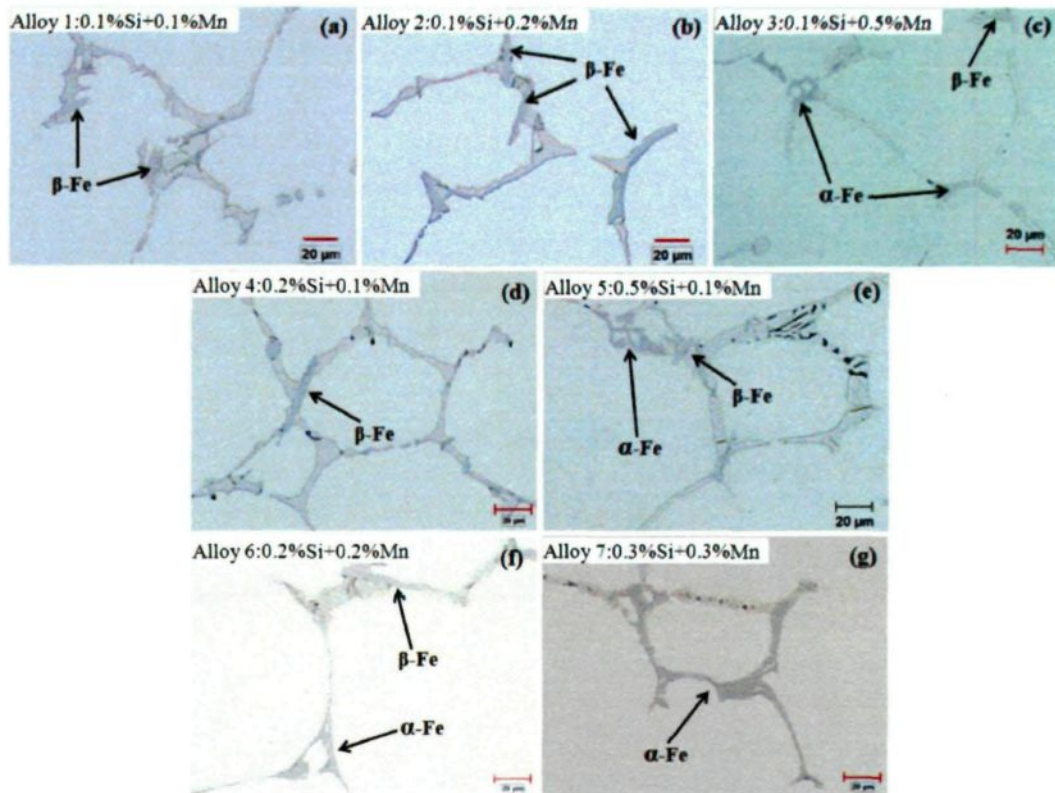
Fig. 4.7 Microstructures of the experimental alloys
with individual or combined additions of Mn and/or Si

It can be seen that all the iron-rich intermetallics in the base alloy (Alloy 1 with 0.1%

Si and 0.1% Mn) are found to be platelet β-Fe (Fig. 4.7a). Similarly, as shown in Figs. 4.7b

and 4.7d, almost all the iron-rich intermetallics are still platelet β-Fe in Alloys 2 and 4,

respectively, in which either the Mn or Si content is individually increased to 0.2%. With

further increase of either the Mn or Si up to 0.5%, as shown in Fig. 4.7c (Alloy 3) and Fig.

4.7e (Alloy 5), the Chinese script α–Fe begins to dominate but there still exists some

platelet β-Fe. The formation of α–Fe in Alloys 3 and 5 indicates that the addition of either

Mn or Si can promote the formation of α–Fe and suppress the occurrence of β-Fe, which was also reported in 206 alloy at 0.3% Fe [1, 2]. Fig. 4.7f and Fig. 4.7g illustrate the influence of the combined addition of both Mn and Si on the formation of iron-rich intermetallics. It can be found that both Chinese script α–Fe and β-Fe coexist in Alloy 6 with 0.2% Mn and 0.2% Si but almost all the iron-rich intermetallics are Chinese script α–Fe in Alloy 7 with 0.3% Mn and 0.3% Si, indicating that the combined addition of both Mn and Si is more influential than the individual addition of either Mn or Si. It was reported that Mn can accelerate the peritectic transformation rate to form α–Fe [19] and both Mn and Si are the important alloying elements for α-Fe. Therefore, the formation of α-Fe will be promoted with the addition of Mn and/or Si. Due to the fact that the formation temperature of α-Fe is higher than that for β-Fe in the experimental alloy, less free iron is available for the formation of β-Fe after the precipitation of α-Fe. Therefore, β-Fe is much more difficult to precipitate with increasing addition of Mn and/or Si.

To quantify the iron-containing intermetallics, the volume percent of the total iron-rich intermetallics and α–Fe phase have been measured using image analysis, as shown in Fig. 4.8a, in which the difference between the volume percent of the total iron-rich intermetallics and the α–Fe phase represents the amount of the β-Fe. The contour plot for the effect of Mn and Si on the relative volume percent of the α–Fe is shown in Fig. 4.8b.
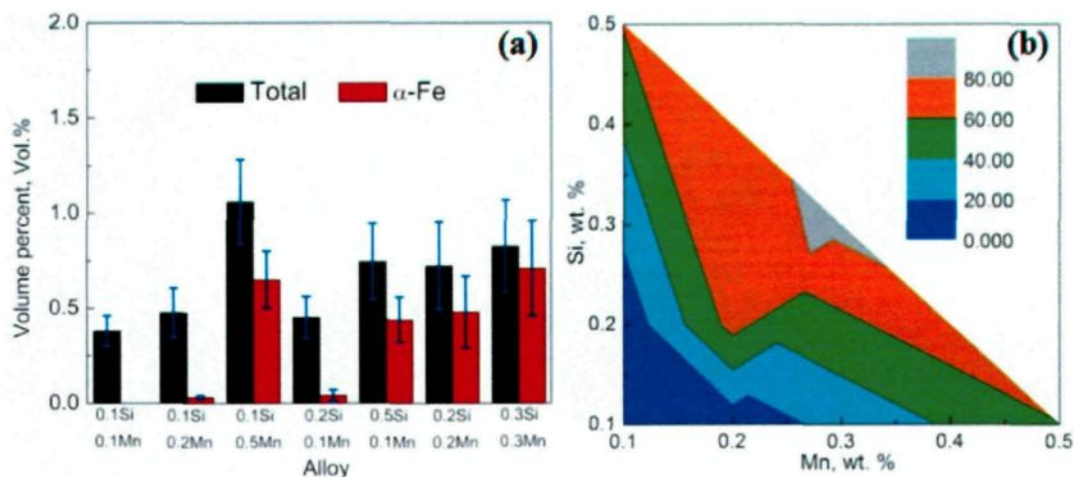
Fig. 4.8 Volume percent of total iron-rich intermetallics and α-Fe (a)
and contour plot of the relative volume percent of α-Fe (b)

As shown in Fig. 4.8a, the volume percents of both the total iron-rich intermetallics

and α–Fe increase with increasing Mn and/or Si contents, confirming their ability to

promote the formation of α–Fe. Meanwhile, the volume percent of β-Fe decreases with

increasing Mn and/or Si contents due to the less free iron available after the precipitation of

α–Fe. In addition, Mn has been found to increase the amount of the α-Fe and the total

iron-rich intermetallics more significantly than Si, especially above an individual addition

of 0.2%, similar to that reported in Al-Si-Cu cast alloys [20]. The individual addition of Mn

is more efficient than Si for the α-Fe phase above a content of 0.2% but their individual

effects on the relative volume percents of the α–Fe phase is similar (Fig. 4.8b), indicating

that the individual addition of either Mn or Si behaves similar for the transformation of

β-Fe into α-Fe phases. For instance, the relative volume percent of α–Fe increases from 0 to

8.8 vol. % to 61.3 vol. % when the Si content is increased from 0.1% to 0.2% to 0.5% , while it changes from 0 to 6.3 vol. % to 59.1 vol. % when Mn is added from 0.1% to 0.2% to 0.5% (Fig. 4.8a). As shown in Fig. 4.8b, the contour curve is concave towards the zero point, indicating the more efficient role of the combined addition of both Mn and Si to transform β-Fe into α-Fe. The highest volume percent for α-Fe, 85.7 vol. %, is found in Alloy 7 with 0.3%Si and 0.3%Mn followed by 66.2 vol. % in Alloy 6 with 0.2%Si and 0.2%Mn, 61.3 vol. % in Alloy 5 with 0.5% Si and 0.1% Mn and 59.1 vol. % in Alloy 3 with 0.1% Si and 0.5% Mn. Therefore, the combined addition of both Mn and Si has a synergistic effect on the formation of α–Fe than the individual addition of either Mn or Si.

In Al-Cu cast alloys, Mn and Si are the effective neutralization elements and Mn/Fe [1-3, 5] and Si/Fe [1, 5] ratios play an important role to modify the Fe-rich phases. It is reported that β-Fe can completely be converted to α–Fe when both the Mn/Fe and Si/Fe are about 1 in 206 type alloys at 0.3% Fe [1-3]. In this work, both Si/Fe and Mn/Fe ratios are up to 3.3. Though the majority of the platelet β-Fe has been converted into Chinese script α–Fe, a small amount of β-Fe is still present in the alloys even at an individual high Mn/Fe ratio (3.3 in Alloy 3 with 0.1% Si and 0.5% Mn) and Si/Fe ratio (3.3 in Alloy 5 with 0.5% Si and 0.1% Mn), or combined Mn/Fe and Si/Fe ratios (2 and 2 in Alloy 7 with 0.3% Si and 0.3% Mn). Compared with the work of Tseng et al. [4, 7], in which the platelet β-Fe was

completely modified into α-Fe when 0.66% Mn was added to 206 alloy at 0.05% Fe-0.01% Si with a Mn/Fe ratio as high as 13.2, it seems that the critical Mn/Fe and Si/Fe ratios for the efficient transformation of β-Fe into α-Fe phases increase with decreasing Fe content in 206 Al-Cu cast alloys. Similar results are also reported in Al-Si cast alloys. The critical Mn/Fe ratio is reported to be about 0.5 in Al-Si alloys with the Fe level higher than 0.5% [9, 10, 21] but about 1.2 at 0.4-0.5% Fe [20, 22] and 2 at 0.3% Fe [9].

4.4   Influence of cooling rate on the formation of iron-rich intermetallics

Fig. 4.9 shows the TA cooling curves of Alloy 4 with 0.2% Si and 0.1% Mn at various cooling rates, and the formation of β-Fe is indicated by the arrows. It can be found that the formation temperature decreases with increasing cooling rate. Besides, the peak intensity of the β-Fe is higher in Fig. 4.9a than that in Fig. 4.9b, while it completely disappears or overlap with the peak of the Al_2Cu eutectic reaction in Fig. 4.9c, indicating that the quantity of the β-Fe decreases with increasing cooling rate.
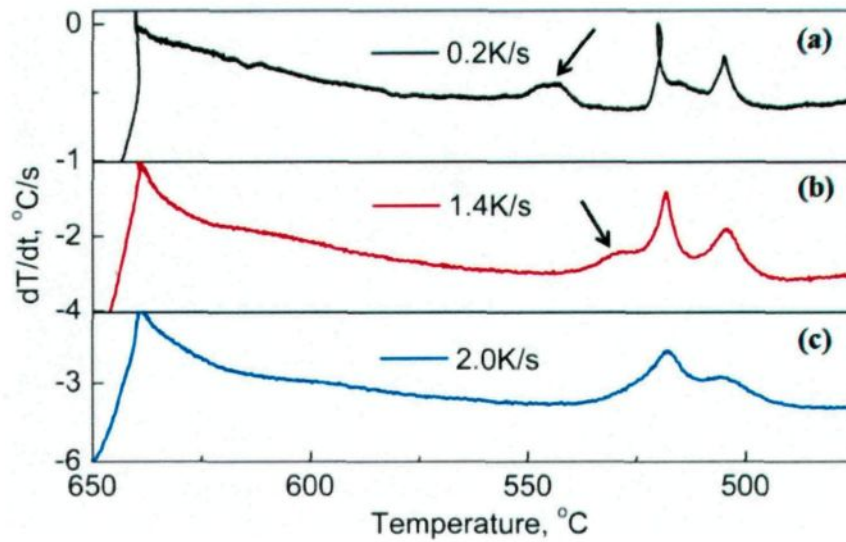
Fig. 4.9 TA cooling curves of Alloy 4 with 0.2% Si and 0.1% Mn at various cooling rates

In Fig. 4.9, α-Fe is not detected in the TA curves due to the low amount of α-Fe

formed in the 0.15% Fe-0.1% Mn-0.2% Si 206 alloy. DSC was also performed to verify the

formation of both phases in Alloy 4 and the heating curves in the enlarged zone between

858 K (585 °C) and 898 K (625 °C) using the cast samples obtained at different cooling

rates are shown in Fig. 4.10. It can be seen that the peak intensity of the β-Fe decreases

with increasing cooling rate, further confirming the results of the TA curves. Therefore, a

higher cooling rate reduces the precipitation temperature and volume percent of the β phase,

i.e. hinders its formation. In contrast, the formation of α-Fe is more obvious in Alloy 4 at

higher cooling rates (1.4 K/S and 2.0 K/S, as shown in Fig. 4.10b). The peak intensity and

formation temperature of the α-Fe phase increase with increasing cooling rate, confirming

the enhancing effect of the cooling rate on the formation of α-Fe. Therefore, higher cooling

rate increases the precipitation temperature and the volume percent of the α-Fe phase, i.e.

favors the formation of α-Fe phase.
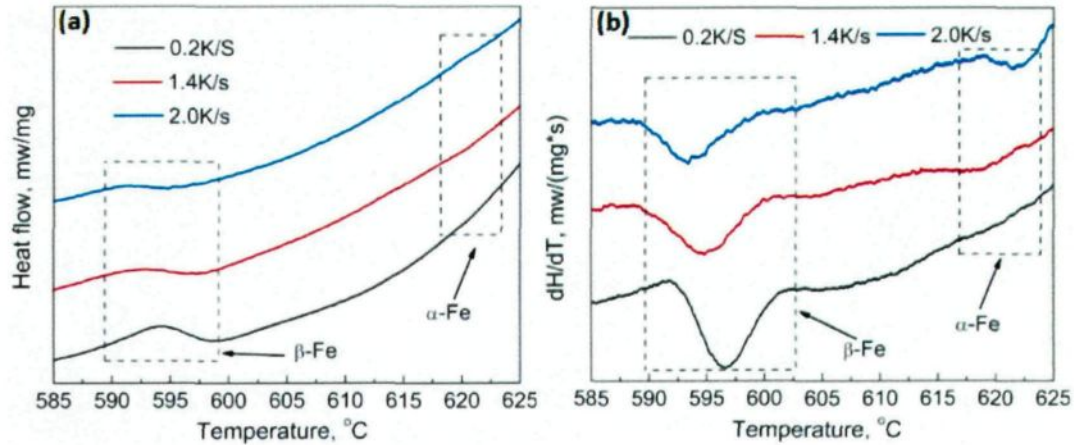
Fig. 4.10 DSC heating curves (a) and their first derivate (b)
of Alloy 4 at various cooling rates

As shown in Figs. 4.9 and 4.10, it can be found that the formation temperature

decreases for β-Fe but increases for α-Fe with increasing cooling rates. Thus, α-Fe is easier

to precipitate than β-Fe, particularly at higher cooling rate. The "early" formed α-Fe

consumes the Fe and the amount of free iron available for β-Fe is reduced. Furthermore,

β-Fe phase precipitates at a temperature more closely to the Al-Cu eutectic reaction at

higher cooling rate, as shown in Fig. 4.9. With the fine eutectic microstructure obtained at

higher cooling rate, the growth of β-Fe can also be expected to be hindered and refined [10,

23]. Therefore, the formation of β-Fe is much more difficult at higher cooling rate.

Table 4.4 shows the relative volume percent of α-Fe at various cooling rates measured using image analysis. It is found that the relative volume percent of the α-Fe rises with increasing cooling rate for each experimental alloy. The cooling rate at which the β-Fe can fully be suppressed depends on the chemical composition. Overall, a lower cooling rate is required to fully suppress the β-Fe phase at higher Mn/Fe and/or Si/Fe ratios. For instance, a high cooling rate of 7.5 K/s is needed to completely inhibit the formation of β-Fe for Alloy 2 with 0.1% Si and 0.2% Mn while it only requires a low cooling rate of 3.5 K/s for Alloy 3 with 0.1% Si and 0.5% Mn. In addition, the relative volume percent of the α-Fe phase varies with alloy composition at a given cooling rate. It is higher in Alloys 3, 5, 6 and 7 than that in Alloys 1, 2 and 4, further confirming the positive effect of the addition of Mn and/or Si on promoting the formation of α-Fe phase.

Table 4.4 elative volume percent of α-Fe at various cooling rates

Alloy #	Elements (wt. %)		Relative Volume Fraction (%)					
	Si	Mn	0.2 K/s	1.4 K/s	2.0 K/s	3.5 K/s	5.0 K/s	7.5 K/s
1	0.1	0.1	0	3.2	4.7	8.5	21.2	66.8
2	0.1	0.2	6.3	11.6	17.8	44.2	76.1	100
3	0.1	0.5	59.1	72.4	89.2	100	100	100
4	0.2	0.1	8.8	14.1	38.3	56.2	96.3	100
5	0.5	0.1	61.3	76.5	97.4	100	100	100
6	0.2	0.2	66.2	78.2	89.9	96.1	100	100
7	0.3	0.3	85.7	96.9	100	100	100	100

Based on the results in Table 4.4, a casting process map to correlate the iron-rich intermetallics to the alloy chemistry and cooling rate is established as shown in Fig. 4.11. It

has been observed that the relative volume percent of the α-Fe phase increases with increasing cooling rate at a given alloy composition. For a given alloy, there exists a threshold cooling rate above which β-Fe can be effectively suppressed. In addition, the relative volume percent of the α-Fe increases with increasing contents of Mn and Si at a given cooling rate and there also exists a critical content of Mn and Si above which β-Fe can be effectively suppressed at a given cooling rate. The critical cooling rate to fully suppress β-Fe phase depends on the alloy chemistry (in particular, the Mn, Si and Fe levels). Generally speaking, a lower critical cooling rate is required at higher contents of Mn and Si. At a cooling rate of 1.5 K/s, almost all Fe-rich phases can precipitate in α-Fe for the alloys with 0.2% Si and 0.2% Mn, 0.1% Si and 0.5% Mn, or 0.5% Si and 0.1% Mn. At a combined addition of 0.3% Mn and 0.3% Si, almost all the iron-rich phases can precipitate in α-Fe at any cooling rates studied in this work. Therefore, the casting process map provides a useful guide for selecting the casting process conditions, controlling the cooling rate, and adjusting the alloy chemistry to obtain the favored iron-rich phase structure and thus optimize the associated mechanical properties of the castings.
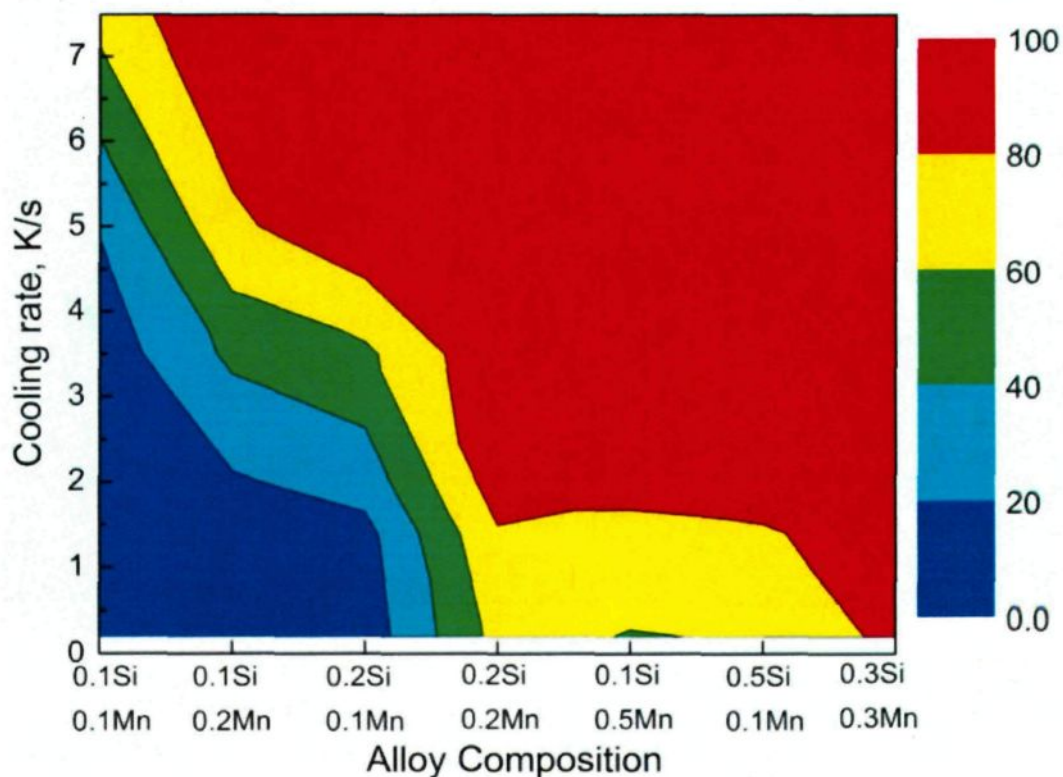
Fig. 4.11 Relative volume percent of α-Fe at various cooling rates
in the experimental 206 cast alloys

As shown in Table 4.1, the AA standard 206.0 cast alloys have Fe up to 0.15% and Si

at about 0.1%, both of which are very low content. A Mn content of 0.2%~0.5% is added to

modify the platelet β-Fe. However, it is found in the present work that the individual

addition of either Mn or Si is less efficient than the combined addition of both Mn and Si

on promoting α-Fe and hindering β-Fe, as similarly reported in 206 type alloys at 0.3% Fe

[1-3]. In addition, it has also been reported that Si can increase the fluidity and hot tearing

resistance for Al-Cu cast alloys [24-26]. Therefore, a higher Si content limit of 0.2-0.3% is

recommended for the 206 cast alloys. For example, the combined addition of 0.2% Mn and 0.2% Si at a cooling rate above 1.5 K/S, which is similar to that in permanent mould casting, can fully suppress β-Fe and Chinese script α-Fe becomes the dominant iron-rich intermetallics. At a combined addition of 0.3% Mn and 0.3% Si, almost all iron-rich phases can precipitate in α-Fe in any casting process. Recently, it was reported that the similar mechanical properties to those for B206 alloy can still be obtained in 206 cast alloys containing 0.21-0.31% Fe, 0.21-0.34% Si and 0.24% Mn, indicating the potential of developing 206 cast alloys with higher allowable contents of Fe and Si [27]. However, some more testing for mechanical properties may still need to define the allowable content of Si.

4.5 Summary

(1) Chinese script α-Fe and platelet-like β-Fe can precipitate and coexist in the finally solidified 206 cast alloy, depending on the alloy composition. The full solidification sequence of the 206 cast alloys has been established.

(2) The individual addition of either Mn or Si promotes the formation of α-Fe and hinders the occurrence of β-Fe. However, the combined addition of both Mn and Si has a synergistic effect on this phase modification.

(3) The volume fraction and formation temperature increase for α-Fe but decrease for β-Fe with increasing cooling rate. There exists a critical cooling rate to effectively suppress the formation of β-Fe for a given alloy composition. The threshold cooling rate depends on the alloy composition but a lower value is needed at the higher Mn/Fe and Si/Fe ratios.

(4) The platelet β-Fe can effectively be suppressed in 206 cast alloys by controlling the alloy chemistry and cooling rate. A casting process map is established to correlate the Mn and Si contents with cooling rate for the 206 cast alloys.

References

[1] H. Kamguo Kamga, D. Larouche, M. Bournane and A. Rahem: *Metall. Mater. Trans. A*, 2010, Vol. 41, pp. 2844-2855.

[2] K. Liu, X. Cao and X. G. Chen: *Light Metal – Advances in Materials and Processes*, Met. Soc, Vancouver, BC, Canada, 2010, pp. 113-120.

[3] K. Liu, X. Cao and X. G. Chen: *Metall. Mater. Trans. A*, 2011, Vol. 42, pp. 2004-2016.

[4] C. J. Tseng, S. L. Lee, S. C. Tsai and C. J. Cheng: *J. Mater. Res.* , 2002, Vol. 17, pp. 2243-2250.

[5] A. Couture: *Int. Cast Met. J.*, 1981, Vol. 6, pp. 9-17.

[6] L. Bäckerud, *Solidification characteristics of aluminum alloys*, Skanaluminium, Universitetsforlaget AS, Oslo, Norway, 1986.

[7] C. J. Tseng, S. L. Lee, T. F. Wu and J. C. Lin: *Mater. Trans., JIM*, 2000, Vol. 41, pp. 708-713.

[8] M. Talamantessilva, A. Rodriguez, J. Talamantessilva, S. Valtierra and R. Colas: *Mater. Charact.*, 2008, Vol. 59, pp. 1434-1439.

[9] S. Seifeddine, S. Johansson and I. L. Svensson: *Mater. Sci. Eng., A*, 2008, Vol. 490, pp. 385-390.

[10] S. Belmares-Perales, M. Castro-Román, M. Herrera-Trejo and L. E. Ramirez-Vidaurri: *Met. Mater. Int*, 2008, Vol. 14, pp. 307-314.

[11] L. Y. Zhang, Y. H. Jiang, Z. Ma, S. F. Shan, Y. Z. Jia, C. Z. Fan and W. K. Wang: *J. Mater. Process. Technol.*, 2008, Vol. 207, pp. 107-111.

[12] Aluminum Association, *Designations and chemical composition limits for aluminum alloys in the form of castings and ingot*, Aluminum Association, Arlington, VA, 2009.

[13] C. L. Chen and R. C. Thomson: *J. Alloys Compd.*, 2010, Vol. 490, pp. 293-300.

[14] M. Kral: *Scripta Mater.*, 2004, Vol. 51, pp. 215-219.

[15] L. F. Mondolfo, *Aluminum alloys: Structure and properties*, Butterworths, London, 1976.

[16] N. A. Belov, A. A. Aksenov and D. G. Eskin, *Iron in aluminum alloys: impurity and alloying element*, Taylor & Francis, London, 2002.

[17] N. A. Belov, D. G. Eskin and A. A. Aksenov, *Multicomponent phase diagrams applications for commercial aluminum alloys*, Elsevier, Amsterdam; Boston, 2005.

[18] V. S. Zolotorevsky, N. A. Belov and M. V. Glazoff, *Casting aluminum alloys*, Elsevier Science, Oxford, 2007.

[19] M. Warmuzek, J. Sieniawski, A. Gazda and G. Mrówka: *Adv. Mater. Sci.*, 2003, Vol. 4, pp. 81-91.

[20] J. Y. Hwang, H. W. Doty and M. J. Kaufman: *Mater. Sci. Eng., A*, 2008, Vol. 488, pp. 496-504.

[21] S. S. Sreeja Kumari, R. M. Pillai, T. P. D. Rajan and B. C. Pai: *Mater. Sci. Eng., A*, 2007, Vol. 460-461, pp. 561-573.

[22] S. G. Shabestari: *Mater. Sci. Eng., A*, 2004, Vol. 383, pp. 289-298.

[23] L. A. Narayanan, F. H. Samuel and J. E. Gruzleski: *Metall. Mater. Trans. A*, 1994, Vol. 25, pp. 1761-1773.

[24] S. Q. Dong, J. E. Zhou and W. Yan: *Rare Met. Mater. Eng.*, 2005, Vol. 34, pp. 1721-1725.

[25] Y. Han, C. Ban, Q. Ba, S. Guo, S. Wang and J. Cui: *Mater. Lett.* , 2006, Vol. 60, pp. 1884-1887.

[26] H. Kamguo Kamga, D. Larouche, M. Bournane and A. Rahem: *Mater. Sci. Eng., A*, 2010, Vol. 527, pp. 7413-7423.

[27] H. K. Kamga, D. Larouche, M. Bournane and A. Rahem: *Int. J. Cast Met. Res.*, 2012, Vol. 25, pp. 15-25.

CHAPTER 5

IRON-RICH INTERMETALLICS

IN 206 CAST ALLOYS AT 0.3% FE

Chapter 5

Iron-rich intermetallics in 206 cast alloys at 0.3% Fe

5.1 Introduction

In Chapter 4, the formation of iron-rich intermetallic in 206 cast alloys at 0.15% Fe, the maximum tolerable iron content in commercial 206 cast alloys, has been dealt with. However, little work on the solidification of the iron-rich intermetallics in A206 aluminum cast alloys at higher iron content has been reported.

Many researchers [1-6] have completed abundant work on iron-rich intermetallics in Al-Si cast alloys. Generally speaking, iron-rich intermetallics can be grouped into three kinds of morphologies: polyhedral or star-like, Chinese script and platelet. Hwang *et al.* [7] reported that the polyhedral iron intermetallics usually form at high Mn contents. These polyhedral iron intermetallic particles are also called α-Fe phase. Shabestari [8] found that

---

The major content of this chapter were publishes as:

5.2: K. Liu, X. Cao, X.-G. Chen, "Solidification of iron-rich intermetallic phases in Al-4.5Cu-0.3Fe cast alloy", Metallurgical and Materials Transaction A, 2011, 42A (7): 2004-2016;

5.3: K. Liu, X. Cao, X.-G. Chen, "Effect of Mn and Si on iron-containing intermetallics in cast 206 aluminum alloys", in Conference of Metallurgists 2010, (COM 2010), Vancouver, BC, Canada, October 3–6, 2010, pp.113-120.

this polyhedral α-Fe phase is detrimental to the mechanical properties because of the formation of "sludge" in the presence of excessive Mn and/or Cr. In addition, α-Fe phase can also precipitate in Chinese script. Cameron *et al.* [9] reported that the Chinese script phase is Al_8Fe_2Si at low Mn contents and high cooling rates but $Al_{15}(FeMn)_3Si_2$ phase at high Mn contents and low cooling rates. For platelet iron-rich intermetallic phase, it's been thought to be particularly deleterious to the mechanical properties because it is brittle and can act as the stress riser. This platelet phase is usually identified to be Al_5FeSi and can block the feeding when it is precipitated interdendritically, leading to the formation of shrinkage porosity [10].

To date, Backerud *et al.* [11] studied the solidification sequences and reactions of A206 cast alloy and only one iron-rich intermetallic phase, named as Al_7Cu_2Fe, was found in the final solidified structure of the A206.2 alloy with 0.03% Fe and 0.26% Mn. This only Al_7Cu_2Fe phase was further observed in the Al-Cu alloy with 0.07% Fe and 0.24% Mn by Talamantes-Silva *et al.* [12].

To investigate the effect of Mn and Fe on the microstructure of A206 cast alloy, Tseng *et al.* [13, 14] found that Al_7Cu_2Fe phase appeared in the A206 alloy up to 0.29% Mn but a Mn-bearing Chinese script iron-rich intermetallics formed at higher Mn. Moreover, Al-Cu-Fe-Mn and Al-Cu-Fe-Mn-Si phases were also reported in A206 alloy

with 0.2 wt. % Fe and 0.2 wt. % Mn by Sigworth [15]. However, the characteristics of the

Mn-bearing or Al-Cu-Fe-Mn-Si phases, such as their precipitation temperatures and

nucleation mechanisms, have never been investigated.

In summary, the solidification of the iron-rich intermetallics in 206 cast alloys is

still not well understood and hence more work is needed, especially at higher contents of

iron. This chapter is aimed at studying the solidification of the iron rich intermetallic phases

in Al-4.5Cu-0.3Fe alloys, including their precipitation temperatures, solidification reactions,

and nucleation mechanisms. Meanwhile, effect of both Mn and Si additions on the

formation and transformation of the iron-rich intermetallics will also be dealt with.

Table 5.1 shows the chemical compositions of the experimental alloys used in this

work. A standard A206 alloy with 0.1% Fe and some alloys with 0.3% Fe at various levels

of Mn and Si were prepared. In each test, approximately 3 kg material was prepared in a

clay-graphite crucible using an electric resistance furnace. The temperature of the melt was

maintained at ~1023 K (750 °C) for 30 minutes. The melt was then poured into a thin shell

crucible made of stainless steel, which had been preheated to the melt temperature (Fig.

3.1). The cooling rate measured in the mushy zone is about 0.2 K/s. OM and SEM were

used to observe the microstructures and identify the iron-rich intermetallics while TA and

DSC were performed to distinguish and confirm the solidification sequences of iron-rich

intermetallics. Details of solidification and experimental methods can be found in Chapter 3

Table 5.1 Chemical compositions of 206 alloys at 0.3% Fe used in this work

Alloy #	Element (wt. %)								
	Cu	Mg	Fe	Si	Mn	Zn	Ti	Ni	Al
A206 base	4.52	0.27	0.09	**0.08**	**0.35**	0.05	0.02	0.02	Bal.
1	4.46	0.27	0.33	**0.08**	**0.11**	0.05	0.02	0.02	Bal.
2	4.48	0.31	0.31	**0.21**	**0.19**	0.05	0.02	0.02	Bal.
3	4.51	0.32	0.32	**0.31**	**0.31**	0.05	0.02	0.02	Bal.
4	4.45	0.29	0.31	**0.11**	**0.19**	0.05	0.02	0.02	Bal.
5	4.52	0.28	0.29	**0.11**	**0.41**	0.05	0.02	0.02	Bal.
6	4.51	0.29	0.29	**0.19**	**0.09**	0.05	0.02	0.02	Bal.
7	4.59	0.31	0.31	**0.31**	**0.11**	0.05	0.02	0.02	Bal.

5.2 Solidification behaviors of iron-rich intermetallics

5.2.1 Iron-rich intermetallics present in the experimental alloys

Fig. 5.1 shows the microstructures of the A206 base alloy and Alloys 1-3 with

various Mn and Si contents at 0.3% Fe. It is found that most of the iron-rich intermetallics

are platelet phases (A and B) with some Chinese script iron-rich intermetallics (C) in the

206 base alloy. In contrast, only platelet iron-rich intermetallics (A and B) present in Alloy

1 with 0.1 Mn and 0.1 Si. In addition to the platelet iron-rich phase, the Chinese script

iron-rich intermetallic phase (C) is observed in Alloy 2 with higher Mn and Si contents (0.2

Mn and 0.2 Si) than Alloy 1. In Alloy 3 with 0.3 Mn and 0.3 Si, however, almost all the

iron-rich intermetallic particles are Chinese script phase.
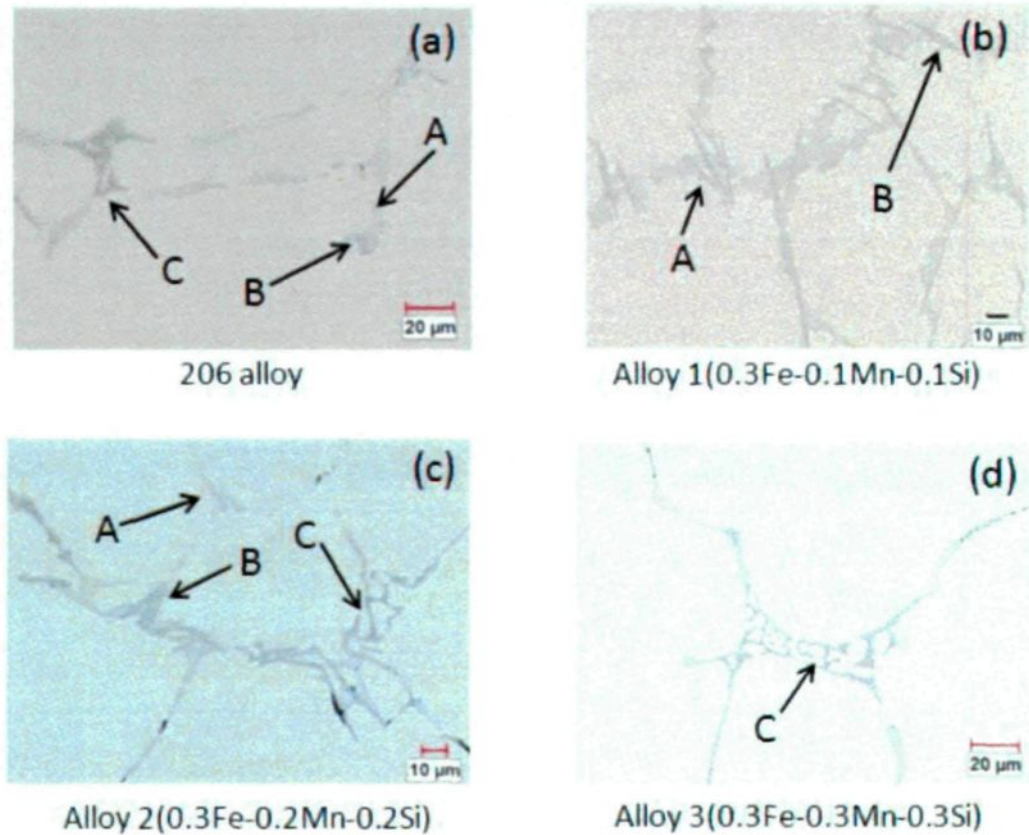
Fig. 5.1 Microstructures of alloys with various Mn and Si

The SEM-EDS results of phases A, B and C as indicated in Fig. 5.1 are shown in

Table 5.2. The platelet iron-rich intermetallics are Al_7Cu_2Fe or $Al_7Cu_2(FeMn)$ commonly

termed as β-Fe, and the Chinese script iron-rich phase is $Al_{15}(FeMn)_3(SiCu)_2$, which is

generally named as α-Fe. $Al_7Cu_2(FeMn)$ is the same phase as Al_7Cu_2Fe but some iron

atoms are replaced by Mn. Compared with the results of Backerud et al. [11], one more

iron-rich intermetallic phase $Al_{15}(FeMn)_3(SiCu)_2$ is observed in addition to

$Al_7Cu_2Fe/Al_7Cu_2(FeMn)$ in A206 cast alloy.

Table 5.2 Average compositions of the iron-rich intermetallics phases (SEM-EDS)

No.	Elements (at. %)					Iron-rich intermetallics
	Al	Mn	Fe	Cu	Si	
A	71.33±0.78	0.28±0.08	8.35±0.28	20.03±0.14	0	Al_7Cu_2Fe
B	71.28±0.66	1.57±0.14	6.50±0.16	20.65±0.22	0	$Al_7Cu_2(FeMn)$
C	74.19±0.75	3.36±0.28	13.1±0.22	3.10±0.11	6.25±0.22	$Al_{15}(FeMn)_3(SiCu)_2$

In order to investigate the formation of the iron-rich intermetallics in detail,

interrupted water quenching technique was used to observe the iron-rich intermetallics

formed at different temperatures. Figs. 5.2-5.4 show the microstructures of the samples

which were water quenched at 873 K (600 °C) and 843 K (570 °C) for Alloys 1-3.

As shown in the microstructures of the water quenched samples, an iron-rich

intermetallic phase with Chinese script type morphology is observed in all the samples

water quenched at 873 K (600 °C). However, the SEM-EDS results show that little Si is

detected in this phase for alloy 1 (Fig. 5.2a) but Si is present in the iron-rich intermetallic

particles for Alloy 2 (Fig. 5.3a) and Alloy 3 (Fig. 5.4a). The SEM-EDS results indicate that

the iron-rich intermetallic phase shown in Fig. 5.2a is $Al_6(FeMnCu)$ but

$Al_{15}(FeMn)_3(SiCu)_2$ (α-Fe) in Fig. 5.3a and Fig. 5.4a. Significant differences are also

observed in the samples water quenched at 843 K (570 °C). It can be seen that only platelet

β-Fe phase appears in Alloy 1 with 0.1 Mn and 0.1 Si but both platelet β-Fe and Chinese

script α-Fe phases exist in Alloy 2 with 0.2 Mn and 0.2 Si. In Alloy 3 with 0.3 Mn and 0.3

Si, however, platelet β-Fe is seldom observed and most of the iron-rich intermetallic

particles are Chinese script α-Fe.
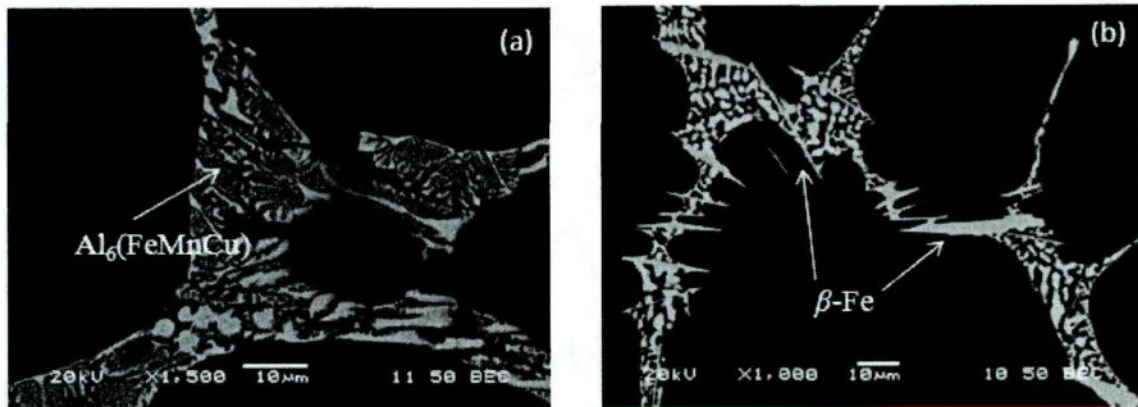
Fig. 5.2 Microstructures of Alloy 1 (0.1Mn+0.1Si) water quenched
at (a) 873 K (600 °C) and (b) 843 K (570 °C)
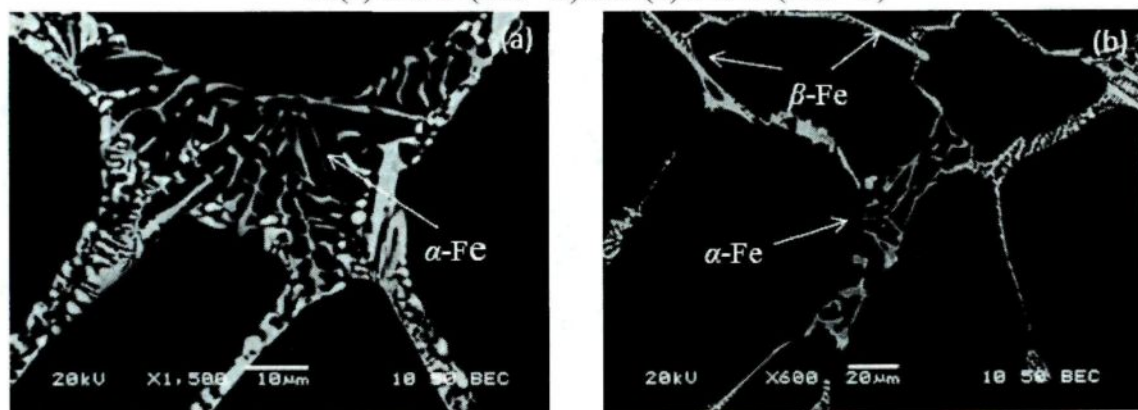
Fig. 5.3 Microstructures of Alloy 2 (0.2Mn+0.2Si) water quenched
at (a) 873 K (600 °C) and (b) 843 K (570 °C)
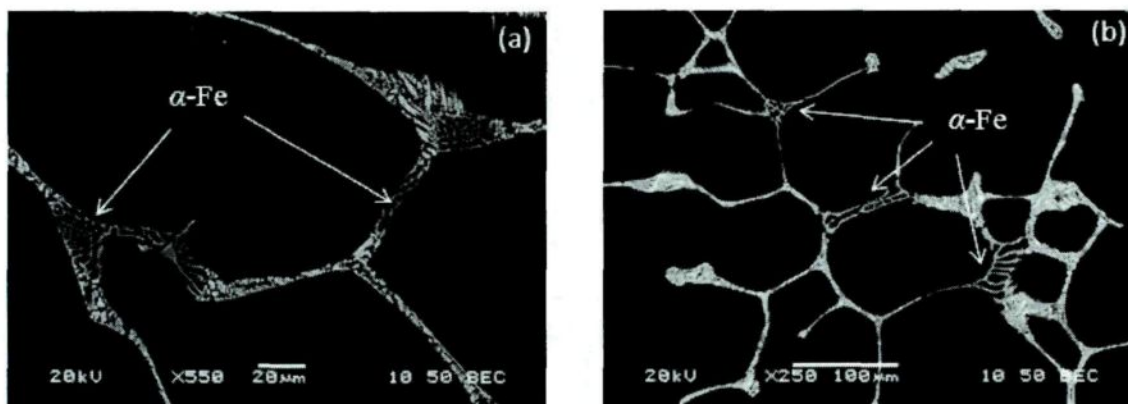
Fig.5.4 Microstructures of Alloy 3 (0.3Mn+0.3Si) water quenched
at (a) 873 K (600 °C) and (b) 843 K (570 °C)

Combined with the microstructures obtained in the final solidified and water quenched samples, it can be summarized that there are three iron-rich intermetallic phases: $Al_6(FeMnCu)$, platelet $Al_7Cu_2(FeMn)$ or Al_7Cu_2Fe, and Chinese script $Al_{15}(FeMn)_3(SiCu)_2$. The $Al_7Cu_2(FeMn)$ phase contains some Mn which replaces some Fe atoms in Al_7Cu_2Fe. Therefore, both Al_7Cu_2Fe and $Al_7Cu_2(FeMn)$ have a platelet morphology. In contrast, $Al_{15}(FeMn)_3(SiCu)_2$ has a Chinese script morphology. However, $Al_6(FeMnCu)$ is formed at relatively high temperature (around 645-650 °C) and can be observed in the water quenched structures but disappears in the final microstructure. Therefore, the β-Fe (Al_7Cu_2Fe or $Al_7Cu_2(FeMn)$) and the α-Fe ($Al_{15}(FeMn)_3(SiCu)_2$) are the two main iron-rich phases as generally observed in the final microstructure of the Al-4.5Cu-0.3Fe alloys.

To further disclose the morphologies of the iron-containing intermetallics, some selected specimens were deeply etched. Fig. 5.5 shows the typical three-dimensional morphologies of the iron-containing intermetallics.

Fig. 5.5 Three-dimensional morphologies of iron-containing intermetallics
(a) Eutectic Al_7Cu_2Fe, (b) Pre-eutectic $Al_7Cu_2(FeMn)$, and (c) $Al_{15}(FeMn)_3(SiCu)_2$

It can clearly be seen that the fine β-Fe has a plate shape interwoven with the Al_2Cu phase in the Al matrix as indicated in Fig. 5.5a. In contrast, the coarse β-Fe in Fig. 5.5b is like a rod embedded in the Al matrix. As shown in Fig. 5.5c, the α-Fe has a typical dendrite form. Many primary branches with different sizes grow from a center nucleus and some secondary branches can grow directly from the sides of the large primary axes.

5.2.2   Solidification sequence of iron-rich intermetallic phases

Fig. 5.6 shows the TA curves and their first derivatives for all four 206 alloys. It can be seen that there are 4 peaks in the A206 base alloy and 3 peaks in Alloy 1 with 0.1 Mn and 0.1 Si but 5 peaks in Alloys 2 and 3, indicating that the solidification reactions have changed with the alloy compositions. It is observed that Peak 2 in Fig. 5.6d (Alloy 3) is

higher than that in Fig. 5.6c (Alloy 2) while Peak 3 in Alloy 3 is lower than that in Alloy 2,

indicating that the quantity of the formed intermetallics have also changed with alloy

chemistry.
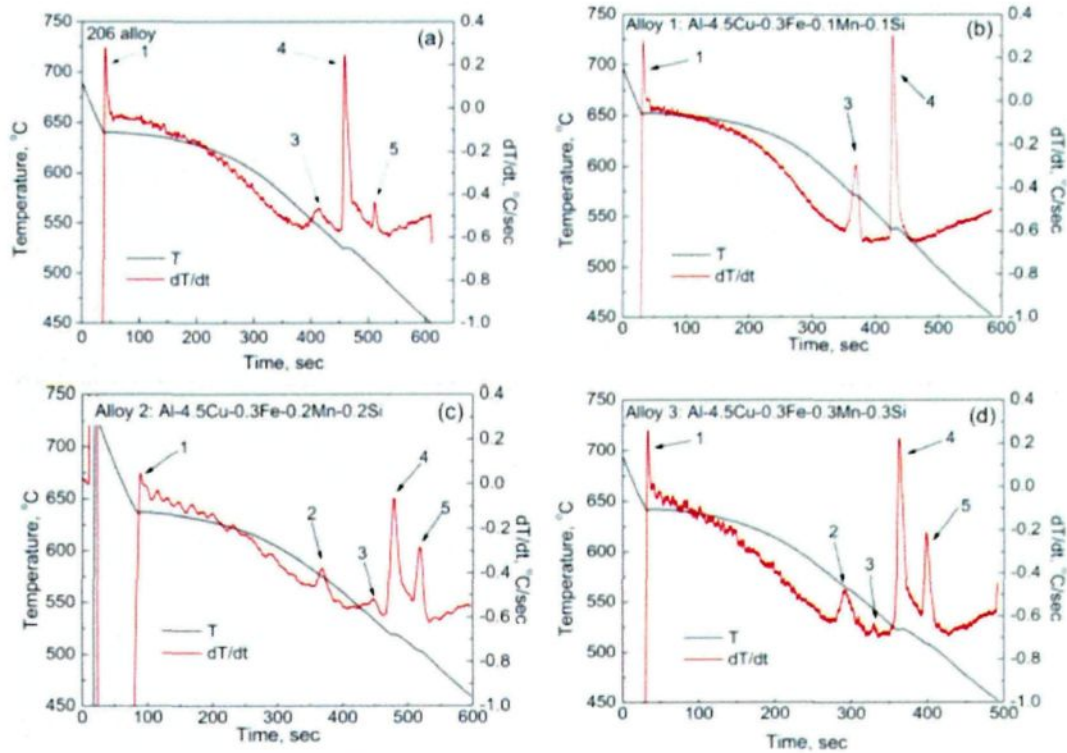
Fig. 5.6 TA curves of the 4 alloys used in this work

The DSC heating curves are shown in Fig. 5.7. It can also be seen that there are 4

peaks in the baseline A206 alloy (Fig. 5.7a) and 3 peaks in Alloy 1 (Fig. 5.7b) but 5 peaks

in Alloys 2 (Fig. 5.7c) and Alloy 3 (Fig. 5.7d). Therefore, the peaks obtained in the DSC

heating curves are highly consistent with those obtained from the TA cooling curves.

Similarly to the TA results, it can be seen that peak 2 is Alloy 3 (Fig. 5.7d) is higher than

that in Alloy 2 (Fig. 5.7c) indicating that the volume fraction of the phase formed at this temperature is higher. Almost all the iron-rich intermetallic particles are α-Fe in Alloy 3 but both platelet β-Fe and Chinese script α-Fe phases are observed in Alloy 2. The reaction appearing in peak 2, therefore, is most probably related to the formation of α-Fe phase.
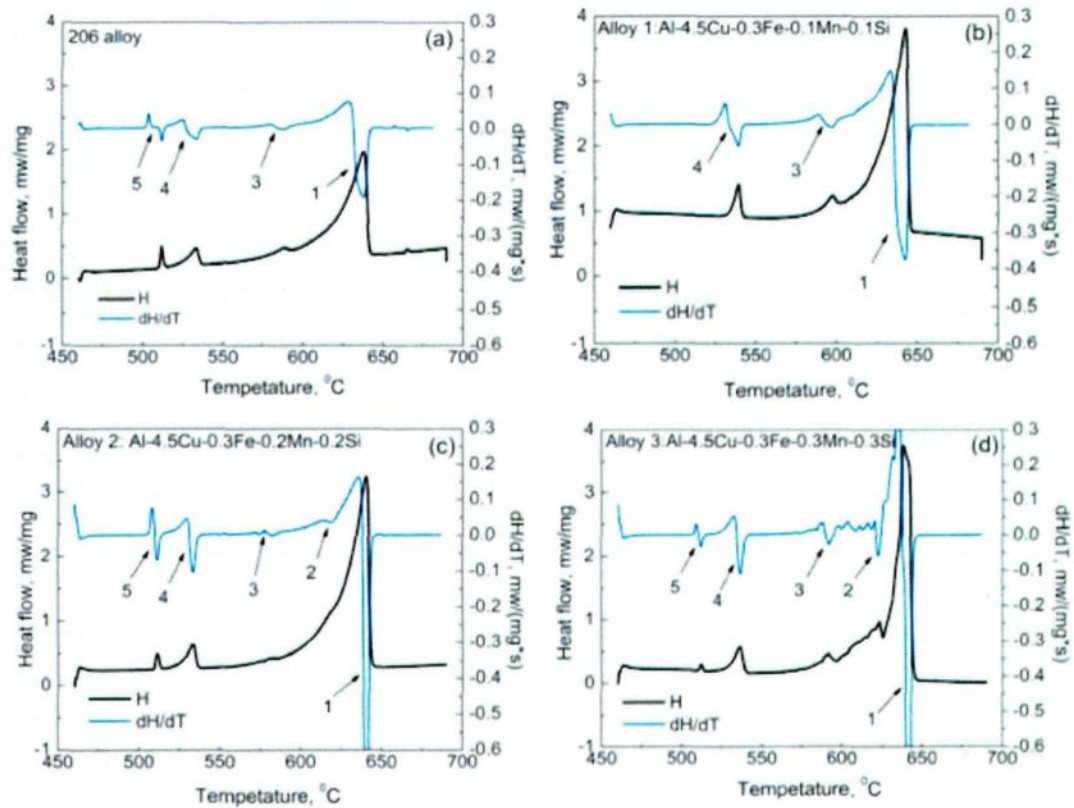
Fig. 5.7 DSC heating curves of the 4 Alloys used in this work

It should be pointed out that a few Chinese script α-Fe phase is observed in Fig. 5.1a for the base 206 alloy but Peak 2 is not shown in the TA (Fig. 5.6a) and DSC (Fig. 5.7a)

curves. The reason for this is probably due to the small amount of the Chinese script phase so that the heat released is not sufficient to be reflected in the TA or DSC curves.

Combining all the information obtained from the TA and the DSC with the observed microstructures, all possible solidification reactions and paths are listed in Table 5.3. The main reactions appearing in dendritic development, eutectic and post-eutectic stages agree well with those from Backerud *et al.* [11]. However, the reactions appearing in the post-dendritic or pre-eutectic stage are absent in the work of Backerud *et al.* [11]. In this study, these reactions related to the precipitation of the Fe-rich phases seem to be well supported by the TA and DSC results as well as the microstructural observations.

Table 5.3 Possible solidification reactions in experimental 206alloys at 0.3%Fe

Peak	Temp. range	Reaction	Suggested temp. K (°C)*	Solidification stage
1	T: T_L	A: Aluminum dendrite network forms B: Liq.→Al+Al$_6$(FeMnCu)	923~918 (650~645)	Dendritic
2	T: T_L~T_E	a):Liq.+Al$_6$(FeMnCu)→Al+Al$_{15}$(FeMn)$_3$(SiCu)$_2$ b:) Liq.→Al+Al$_{15}$(FeMn)$_3$(SiCu)$_2$	898~883 (625~610)	Post-dendritic
3**	T: T_L~T_E	a):Liq.+Al$_6$(FeMnCu)→Al+Al$_7$Cu$_2$(FeMn) b):Liq.+Al$_{15}$(FeMn)$_3$(SiCu)$_2$→Al+Al$_7$Cu$_2$(FeMn) c):Liq.→Al+Al$_7$Cu$_2$(FeMn)	868~858 (595~585)	Pre-eutectic
4	T : T_E	Liq.→Al+Al$_2$Cu+Al$_{20}$Mn$_3$Cu$_2$+Al$_7$Cu$_2$Fe	813~803 (540~530)	Eutectic
5	T : <T_E	Liq.→Al+Al$_2$Cu+Al$_2$CuMg+Mg$_2$Si	783~773 (510~500)	Post-eutectic

Notes: The peak numbers are corresponded to those as indicated in Figs. 5.6 and 5.7.

* Temperatures are determined from the DSC heating curves, which eliminate the

undercooling effect.

    ** Some reactions may depend on the alloy compositions.

    A, B: The two different reactions may overlap.

    T_L, T_E: Liquids temperature for formation of Al dendrite and Al-Cu eutectic.

One feature should be pointed out concerning Peak 1 in the present work. During the research of Backerud et al. [11], they found that the aluminum dendrites begin to develop at 924~922 K (651~649 °C) while the Al_6(FeMnCu) forms at 922 K (649 °C). In other words, the precipitation of Al_6(FeMnCu) follows the Al dendrites almost immediately. This is also further confirmed in this work. Only one peak is observed over this temperature range, but Al_6(FeMnCu) is present in the sample after water quenching at 873 K (600 °C) (Fig. 5.2a) indicating that the two reactions seem to be overlapped at Peak 1. Table 5.3 lists all solidification reactions possibly appearing in A206 alloys but the presence of some will depend on the alloy composition. For instance, Peak 2 is absent in the A206 base alloy and Alloy 1 but appears in Alloy 2 and more in Alloy 3, indicating the increased amount of the α-Fe phase with the increasing Mn contents. In contrast, Peak 3 becomes gradually weaker from Alloys 1 to Alloy 3, indicating that the amount of the Al_7Cu_2(FeMn) phase decreases with increasing Mn contents from Alloy 1 to Alloy3. These observations have been well confirmed by the microstructure results are consistent with well known knowledge.

As indicated in Table 5.3, β-Fe can precipitate prior to the eutectic reaction 858~868 K (585~595 °C) and/or at eutectic reactions 803~813 K (530~540 °C). Here,

Reaction 4 is defined as main eutectic reaction because this reaction is present in all the alloys with various compositions in this work. The β-Fe platelet ($Al_7Cu_2(FeMn)$) formed prior to the main eutectic reaction is termed as pre-eutectic β-Fe in this work and contains some Mn element which replaces some Fe atoms. Element Mn can be obtained through its direct diffusion from the Al melt or from $Al_6(FeMnCu)$, or $Al_{15}(FeMn)_3(SiCu)_2$ through the peritectic reactions as indicated in Peak 3. In contrast, Mn has a lower diffusion rate at lower temperature during the main eutectic reaction and hence the β-Fe (Al_7Cu_2Fe) phase formed during the main eutectic reaction (termed as eutectic β-Fe in this work) contains little Mn. Moreover, some other Mn-containing intermetallics (e.g. $Al_{20}Mn_3Cu_2$ in Peak 4) also consume some Mn. In this case, little Mn is available for Al_7Cu_2Fe during the main eutectic reaction stage. Therefore, to a close approximation, the pre-eutectic β-Fe is expressed as $Al_7Cu_2(FeMn)$ and the eutectic β-Fe as Al_7Cu_2Fe in this work. In contrast, α-Fe can only precipitate at the post-dendritic stage as indicated in Peak 2.

Furthermore, it can be found that $Al_6(FeMnCu)$ takes part in Peaks 2 and 3 to form α-Fe and β-Fe phases, respectively. These are typical peritectic reactions appearing at high temperatures and hence $Al_6(FeMnCu)$ particles are consumed. This is probably the main reason why $Al_6(FeMnCu)$ is only present in the water quenched samples (Fig. 5.2a) but

disappears in the final solidified sample (Fig. 5.1b). In occasional conditions, the remaining $Al_6(FeMnCu)$ may still be observed as the nucleus for α-Fe phase as discussed later.

In the experimental Al-Cu alloys, Al dendrite is the first phase to develop and then other phases will follow. According to the study of Backerud et al. [11], there are only two kinds of iron-rich intermetallics found during solidification: $Al_6(FeMnCu)$ and eutectic Al_7Cu_2Fe (β-Fe). In this study, however, α-Fe and pre-eutectic β-Fe phases are also observed in addition to the $Al_6(FeMnCu)$ and eutectic β-Fe. Many researchers [2-4] have studied the effect of Mn on iron-rich intermetallics in Al-Si alloys and found that the solidification sequence may change with the addition of Mn: α-Fe will precipitate prior to β-Fe at high Mn levels. The present work indicates that this still holds true for Al-4.5Cu alloys also. The α-Fe can form in the post-dendrite stage (Peak 2 in Table 5.3) but before the pre-eutectic and eutectic β-Fe phase (Peaks 3 and 4 in Table 5.3) when high Mn and Si are present.

Fig. 5.8 demonstrated the α-Fe and β-Fe phases obtained from Alloys 1 and 2. Fig. 5.8a shows α-Fe appearing in the interdendritic region. In Fig. 5.8b, a faceted particle is observed in the center of the interdendritic α-Fe whose branches grow from this central nucleus. A β-Fe platelet as indicated in Fig. 5.8cseems to be within the aluminum dendrite. However, further investigations indicate that nearly all β-Fe platelets are located in

interdendritic regions for the experimental alloys used in this work. Therefore, the β-Fe

platelet which was very occasionally observed to appear inside the aluminum dendrite (Fig.

5.8c) is probably due to the sectioning effect. In addition, it's also interested to find that

β-Fe can grow from the α-Fe phase as indicated in Fig. 5.8d.
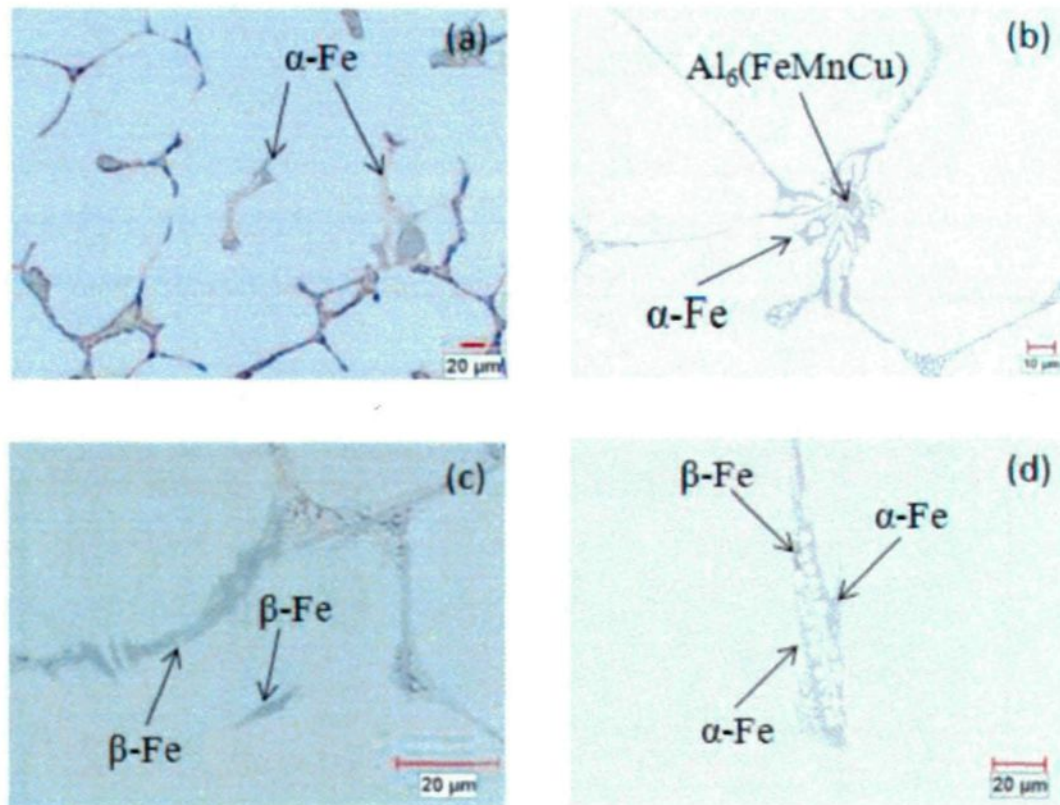
Fig. 5.8 α-Fe and β-Fe phases: (a), (b), and (d) from Alloy 2 and (c) from Alloy 1.

As shown in Fig. 5.8b, a faceted particle is observed in the very center of the α-Fe

phase as a nucleation point. This particle is distinct from the branches of the Chinese script

α-Fe phase and its faceted morphology indicates that it forms at a higher temperature than

the branches. This crystal has similar shape to those in Fig. 5.2a and is identified to be $Al_6(FeMnCu)$ by SEM-EDS. Therefore, the formation of Chinese script α-Fe in Fig. 5.8b is a typical peritectic reaction as indicated in Table 5.4 (Reaction 2): Liq. + $Al_6(FeMnCu) \rightarrow Al + Al_{15}(FeMn)_3(SiCu)_2$. For Peak 3, two possible reactions for the formation of β have been suggested. The reaction 3a) to form β-Fe: Liq. + $Al_6(FeMnCu) \rightarrow Al + Al_7Cu_2(FeMn)$ was reported to occur at 863 K (590 °C) in Al-Cu-Fe system [16] and thus it might be possible to appear in the A206 alloy system investigated in this work. The transformation from early precipitated α-Fe to later formed β-Fe through the peritectic reaction 3b): Liq. + $Al_{15}(FeMn)_3(SiCu)_2 \rightarrow Al + Al_7Cu_2(FeMn)$ is well displayed in Fig. 5.8d. The α-Fe is still observed indicating it has not been consumed at a relatively low temperature.

5.2.3 Nucleation of iron-rich intermetallic phases

For the nucleation of iron-rich intermetallics, there exist some different opinions: Khalifa *et al.* [5] reported that α-Al_2O_3, γ-Al_2O_3, CaO, MgO, TiB_2, TiC, Al_4C_3 and SiC are all the potential nucleation sites for iron-containing intermetallics, depending on the composition and cooling rate. Sigworth [17] suggested that the AlP particles formed in the presence of P in the melt can also nucleate the iron-containing intermetallics..

Recently, Cao and Campbell [18-20] have proposed that oxide films play a significant role in nucleating the iron-rich intermetallics in Al-Si Alloys. During their research, it was observed that almost all the iron-rich intermetallics could nucleate on oxide films which are present in molten Al alloys in large quantities. The entrained oxide films in the liquid metal have two sides: the dry, unbonded inner surfaces, and their wetted exterior surfaces. If intermetallic compounds precipitate onto the doubled-over oxides, they can, of course, only precipitate onto the wetted outer surfaces of the double oxide films. There will, of course, be perfect atomic contact between the wetted side of the film and the liquid from which the film originally grew, atom by atom. Similarly, perfect atomic contact is to be expected between the oxide phase and any intermetallics that have grown on it. All this leads to the expectation that the bonding of the outside surfaces of the folded films with both the matrix and/or the intermetallics will be strong. However, at the risk of laboring what might by now be obvious, the gap between two dry sides of the doubled bifilms is expected to constitute the observed cracks either in the intermetallics or in the matrix because of the expected complete lack of bonding across the folded plane. Thus the cracks observed travelling through such intermetallic particles, or sometimes separating the particle/matrix interfaces, are formed by non-bonded oxide inter layers. This new theory was further confirmed later by D. N. Miller *et al.* [21] in Al-11.6Si-0.37Mn cast alloy

In the present work, the cracks are frequently observed also in both the α-Fe and β-Fe phases as shown in Fig. 5.9. Fig. 5.9a and 5.9b display the oxide cracks in α-Fe while the cracks in β-Fe are shown in Fig. 5.9c and 5.9d. It is interesting to notice that a pore is associated with the two sides of an α-Fe particle as shown in Fig. 5.9b. The two sides of the Fe-rich phase is not only separated by the porosity but also displaced on the left. These observations are consistently with the nucleation of the Fe-rich phases on the wetted sides of the oxide films and the precipitation of gas on the dry sides of the bifilms [18-20]. Therefore, the porosity is an open oxide film. The oxide crack or porosity is a diffusion barrier and thus Fe-rich phases cannot grow through the oxide crack or porosity. Therefore, the displaced Fe-rich phase can form due to the different growth rates along the two wetted sides of the oxide crack or porosity. In Fig. 5.9c, it can be observed that the β-Fe precipitates from α-Fe indicating the transformation from α-Fe to β-Fe through peritectic reaction 3b.
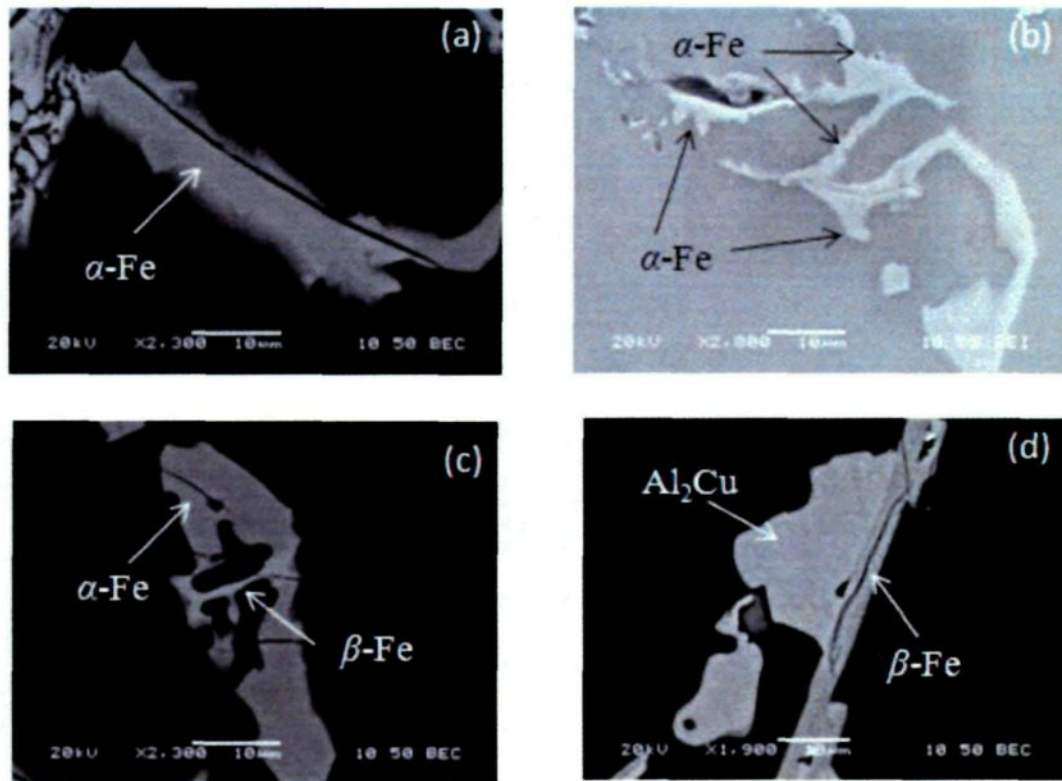
Fig. 5.9 Cracks in α-Fe and β-Fe: (a), (b), and (c) for α-Fe and (d) for β-Fe

Fig. 5.10a displays cracks in α-Fe and the distribution of elements along the red line as shown in Fig. 5.10b-g. For Al, it was found that the content is a little lower when scanned to the crack in Fig. 5.10b while it is slightly higher for Mg in Fig. 5.10c. In Fig. 5.10d, it can be seen that the content of oxygen at the crack is the higher than the other places: the content of oxygen is the highest either side of the crack. In contrast, the crack has lower oxygen peak but is still higher than the surrounding Fe-rich phase. This result further indicates the nature of the oxide film as cracks. In the study of Cao and Campbell

[19], it was found that the oxide films were mainly Al_2MgO_4 when Mg content was between 0.005% and 2%. In this work, the alloy has 0.3% Mg addition and hence the oxide films are most likely to be Al_2MgO_4. As shown in Fig. 5.10, the intensities of Mg (15~20) and O (60~70) seem to support the formation of Al_2MgO_4 in the experimental alloys. Additionally, it is clearly shown that the distributions of Fe, Mn and Si are quite similar, mainly detected from the α-Fe phase. In summary, this work further confirms the nucleation mechanism of the Fe-rich phases on the oxide films which was proposed from Al-Si alloys but is also demonstrated to be true for Al-Cu alloys.
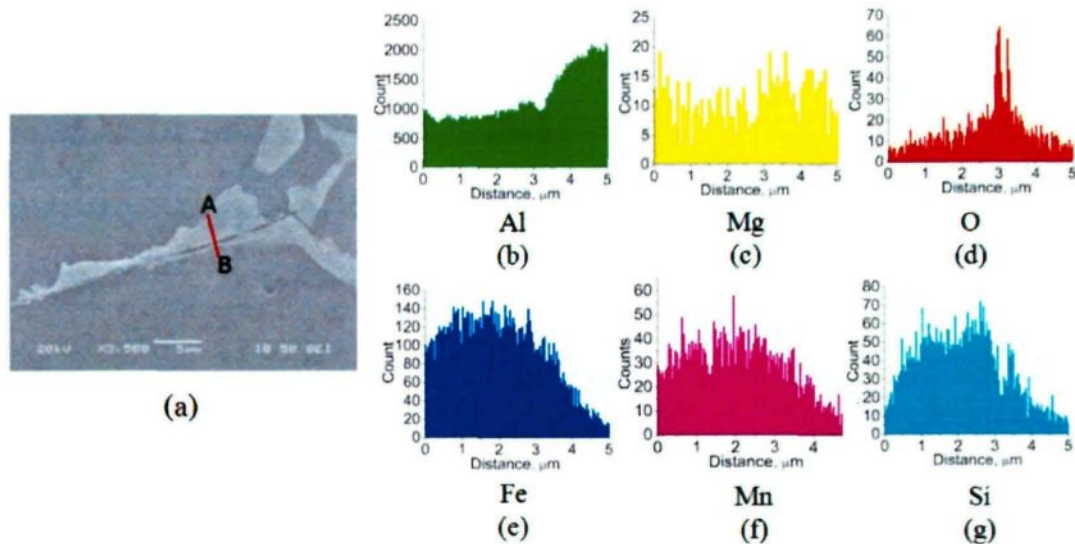
Fig. 5.10 The crack in α-Fe and the distribution of elements along the red line

In addition to the nucleation of Fe-rich phases on oxide films, some other nucleation mechanisms are also observed as demonstrated in the microstructures. In Fig. 5.5c, an

Al_3Ti particle is observed in the centre of the α-Fe. Hence, α-Fe phase can also nucleate on the Al_3Ti particle. As indicated in Fig. 5.8b, α-Fe can precipitate on $Al_6(FeMnCu)$ particles through a peritectic reaction. In addition, it was reported that the early-solidified iron-rich intermetallics can nucleate the iron-rich intermetallics formed later [18]. This is also further confirmed in this work. Fig. 5.8d and Fig. 5.9c display the nucleation of β-Fe on α-Fe phase. This transformation from the α-Fe to β-Fe phases is completed though typical peritectic reactions as listed in Table 5.4.

As is well known, planar disregistry can be used to evaluate nucleation potential [18]. Though the planar disregistry is not the unique factor effecting the nucleation, the nucleation will be much more potential when good registry is achieved. In addition, the planar disregistry is also the only index which can easily be assessed quantitatively. The planar disregistry can be calculated using the following equation [22]:

$$\delta \begin{smallmatrix} (hkl)_s \\ (hkl)_n \end{smallmatrix} = \sum_{i=1}^{i=3} \frac{\left| d_{[uvw]_s} \cos\theta - d_{[uvw]_n} \right|}{d_{[uvw]_n}} \times 100$$

Where $(hkl)_s$ is a low-index plane of the substrate;

$[uvw]_s$ is a low-index direction in $(hkl)_s$;

$(hkl)_n$ is a low-index plane in the nucleated solid;

$[uvw]_n$ is a low-index direction in $(hkl)_n$;

$d_{[uvw]n}$ is an interatomic spacing along $[uvw]_n$;

$d_{[uvw]s}$ is an interatomic spacing along $[uvw]_s$;

θ is the angle between $[uvw]_s$ and $[uvw]_n$.

It is reported that the nucleating agent is potent if the planar disregistry is less than about 12 pct. assuming that the electronic (bonding) contribution to the energy of the interface is favorable. Campbell [23] extended the definition for substantially metallically bonded materials and found that any disregistry less than 23 pct would assist the nucleation to some extent.

In the study of Cao and Campbell [24], they calculated the planar disregistries between different oxide films and α-Fe phase in Al-Si cast alloys and found that some low-index planes have good lattice match and hence may constitute the nucleation of α-Fe on these oxides:

MgO—α-Fe: $(111)_{MgO}//(111)_{\alpha-Fe}$;   δ=0.09 pct

Al_2MgO_4—α-Fe: $(111)_{Al2MgO4}//(111)_{\alpha-Fe}$;   δ=4.19 pct

γ-Al_2O_3—α-Fe: $(111)_{\gamma-Al2O3}//(111)_{\alpha-Fe}$;   δ=6.81 pct

However, no planar disregistry has ever been calculated between the oxide films and the β-Fe phase in Al-Si alloys due to the complexity of the crystal structure for β-Fe phase which is monoclinic.

Table 5.4 shows the crystal information about the Al_3Ti, $Al_6(FeMnCu)$, α-Fe, β-Fe and oxide films in Al-Cu alloys. The data are obtained from the database of the Powder Diffraction File (PDF 2003).

Table 5.4 Data of Al_3Ti, $Al_6(FeMnCu)$, α-Fe, β-Fe and oxide films

Phase	Structure	a (nm)	b (nm)	c(nm)
Al_3Ti	cubic	0.3972		
$Al_6(FeMnCu)$	orthorhombic	0.6434	0.746	0.878
α-Fe	cubic	1.265		
β-Fe	tetragonal	0.6336		1.487
MgO	cubic	0.4213		
Al_2MgO_4	cubic	0.8075		
γ-Al_2O_3	cubic	0.7859		

In Al-Cu alloys, the oxide films (Al_2O_3, Al_2MgO_4, MgO) and α-Fe phases have the same crystal structures and cell sizes as those in Al-Si alloys which were dealt with by Cao and Campbell [24]. In this work, hence, only the planar disregistries between the oxide films and β-Fe, between α-Fe and β-Fe, between $Al_6(FeMnCu)$ and α-Fe, and between Al_3Ti and α-Fe at low index plane families, such as {100}, {110} and {111} have been calculated. From the results, the favorite planar disregistry between different substrates and iron-rich intermetallics have been chosen and listed in Table 5.5.

Table 5.5 Planar disregistries between different substrates and iron-rich phases

Substrate and Phase	Match planes	[uvw]s	[uvw]n	d[uvw]s (nm)	d[uvw]n (nm)	Φ	δ
MgO and β-Fe	(110)s//(110)n	[001]	[Ī10]	5×0.423	2×0.896	0	
		[Ī11]	[Ī11]	5×0.733	2×1.736	4.19	7.94
		[Ī10]	[001]	5×0.598	2×1.487	0	
Al₂MgO₄ and β-Fe	(110)s//(110)n	[001]	[Ī10]	5×0.808	4×0.896	0	
		[Ī11]	[Ī11]	5×1.399	4×1.736	4.19	5.72
		[Ī10]	[001]	5×1.143	4×1.487	0	
γ-Al₂O₃ and β-Fe	(110)s//(110)n	[001]	[Ī10]	4×0.785	3×0.896	0	
		[Ī11]	[Ī11]	4×1.361	3×1.736	4.19	7.18
		[Ī10]	[001]	4×1.111	3×1.487	0	
α-Fe and β-Fe	(100)s//(100)n	[001]	[001]	1.265	1.487	0	
		[011]	[011]	1.789	1.616	21.6	6.00
		[010]	[010]	1.265	1.267	0	
Al₆(FeMnCu) and α-Fe	(100)s//(100)n	[001]	[001]	3×0.878	2×1.265	0	
		[011]	[011]	3×1.152	2×1.789	4.65	6.46
		[010]	[010]	3×0.746	2×1.265	0	
Al₃Ti and α-Fe	(100)s//(100)n	[001]	[001]	3×0.397	1.265	0	
		[011]	[011]	3×0562	1.789	0	5.80
		[010]	[010]	3×0.397	1.265	0	

As indicated in Table 5.5, it seems that the oxide films, such as, MgO, Al₂MgO₄, γ-Al₂O₃ and α-Fe all could be good substrates for the nucleation of β-Fe phase. Similarly, Al₃Ti and Al₆(FeMnCu) could also be potential nucleation sites for α-Fe. The planar disregistries between these substrates and iron-rich intermetallics are all lower than 8 pct, indicating a potential positive effect on nucleation.

Based on the microstructure observation and planar disregistries calculation, the possible nucleation hierarchy for the main iron-rich intermetallics in Al-4.5Cu-0.3Fe A206

type cast alloys are proposed in Fig. 5.11. It can be seen that the oxide film can be the nucleation sites for both α-Fe and β-Fe during the solidification. In addition, α-Fe could also nucleate on Al_6(FeMnCu) and Al_3Ti substrates while the earlier formed α-Fe could nucleate the later formed β-Fe. The Al_3Ti present in liquid metal is most probably from the grain refiner used. The Al_6(FeMnCu) phase precipitates with Al dendrites through eutectic reaction 1B (Table 5.3). The two intermetallic phases, Al_3Ti and Al_6(FeMnCu) are most likely to nucleate on the existing oxide films (as indicated in dot lines in Fig. 5.11) due to their high formation temperatures though no direct evidences are observed in this study.
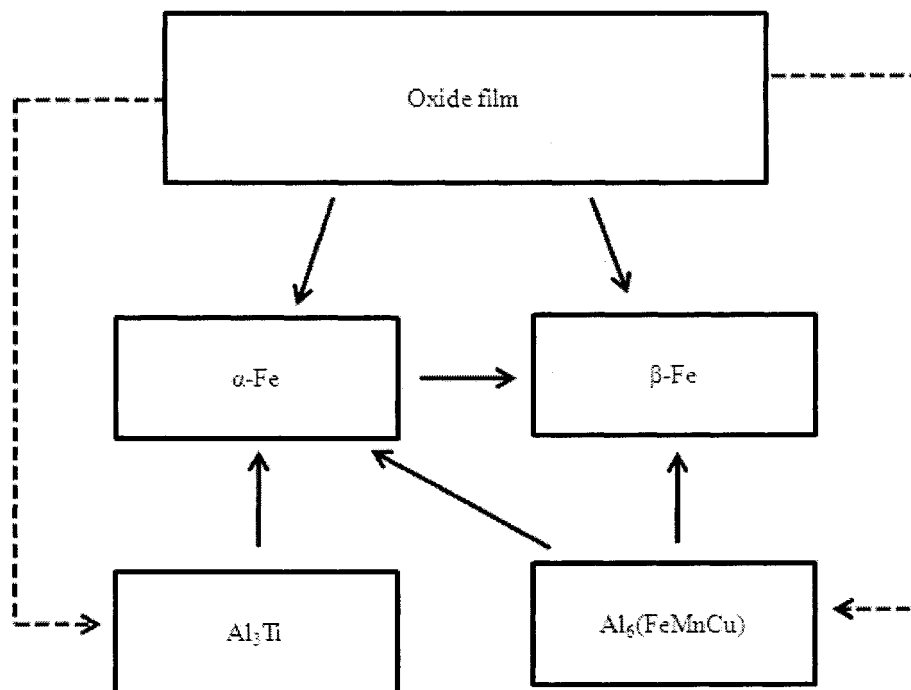
Fig. 5.11 The possible nucleation hierarchy for the main iron-rich intermetallics in Al-4.5Cu-0.3Fe A206 cast alloys (The arrow points to the nucleated phases)

5.3   Effect of Mn and Si on the iron-rich intermetallics

The microstructures of Alloys 1, 4 and 5 at 0.1% Si and various Mn contents are shown in Fig. 5.12. It can be seen that almost all the iron-containing intermetallics in Alloy 1 with a Mn/Fe ratio of 0.3 are β-Fe (Fig. 5.12a). Even though many β-Fe particles are still present, the α-Fe phase is observed in Alloy 4 with a Mn/Fe ratio of 0.67 (Fig. 5.12b). In Alloy 5 with a Mn/Fe ratio of 1.33, the amount of β-Fe is much less than that in Alloy 4 and α-Fe has become the dominant Fe-rich phase. Hence, it can be concluded that the addition of Mn will be useful for the formation of α-Fe. However, the presence of β-Fe phase at a high Mn/Fe ratio of 1.33 indicates that not all the β-Fe can transform to α-Fe. Compared with Alloy 4, it can also be found that Alloy 6 (Fig. 5.14) has much less β-Fe and more α-Fe, indicating that Si also has influence on the formation of iron-containing intermetallics in Al-Cu alloys. Further evidences of the effect of Si on the iron-containing intermetallics are shown in Fig. 5.13.
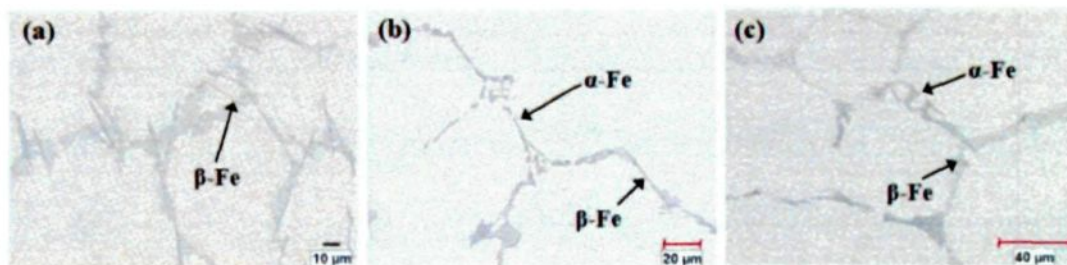
Fig. 5.12 - Microstructures of iron-containing intermetallics in Alloys 1, 4 and 5
(a) Alloy 1 (0.1Si+0.1Mn), (b) Alloy 4 (0.1Si+0.2Mn), and (c) Alloy 5 (0.1Si+0.4Mn)
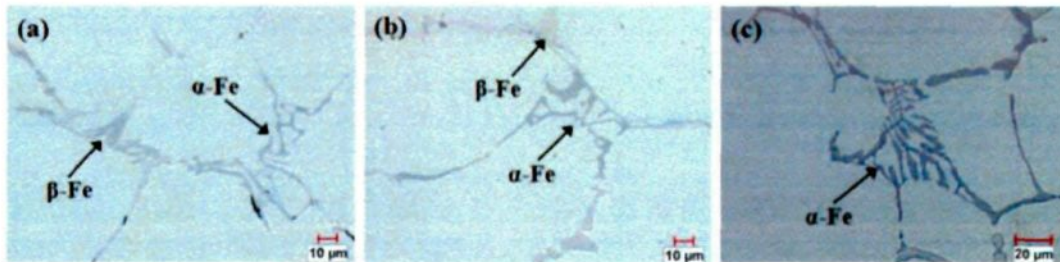
Fig. 5.13 - Microstructures of iron-containing intermetallics in Alloys 6, 7 and 3
(a) Alloy 6 (0.2Si+0.1Mn) , (b) Alloy 7 (0.3Si+0.1Mn) , and (c) Alloy 3 (0.3Si+0.3Mn)

Compared with the microstructures shown in Fig. 5.13, it can be found that Si has a similar effect with Mn on the transformation tendency of Fe-rich phases. The α-Fe phase precipitates in Alloys 6 and 7 but there are still some β-Fe particles. In Alloy 3 with 0.3% Si and 0.3% Mn, however, almost all the Fe-rich particles are α-Fe phase indicating the effective transformation of β-Fe into the α-Fe phase. Additionally, compared with the results in Fig. 5.13b and Fig. 5.13c, it can be concluded that more addition of Mn with the same level of Si (0.3 wt. %) also favors the formation of the α-Fe phase, which further confirms the role of Mn as an effective neutralization agent in Al-Cu alloys .

To quantify the iron-containing intermetallics, the relative volume fraction of the two iron-containing intermetallic phases has been measured using image analysis, as shown in Fig. 5.14. These quantified results are consistent with the general metallographic observations as discussed above. In general, the relative volume fraction of the α-Fe phase increases when increasing the contents of Mn and/or Si. However, the individual addition

of either Mn or Si cannot completely transform a β-Fe into a α-Fe phase even at a high Mn/Fe level of 1.33 or a Si/Fe level of 1.0. At the 0.3 % Si and 0.3 % Mn levels in Alloy 3, the β-Fe has been effectively suppressed and hence almost all iron-containing intermetallics precipitate in the α-Fe phase. This indicates that a combination of both high Si and Mn levels can completely transform β-Fe into a α-Fe phase. Comparing Alloy 7 (0.3 % Si+0.1% Mn) with Alloy 2 (0.2% Si+0.2% Mn), there is more α-Fe precipitate in Alloy 6 indicating that Mn is a more effective element than Si to transform β-Fe into the α-Fe phase. The results can also be further confirmed by the comparison of Alloy 4 (0.1% Si+0.2% Mn) and Alloy 6 (0.2% Si+0.1% Mn).
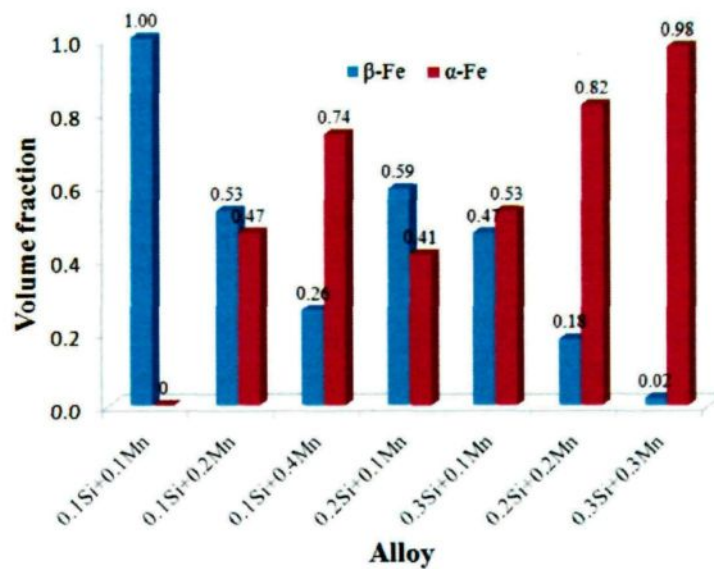
Fig 5.14 - Volume fraction of iron-rich intermetallics in Alloys 1 to 7

[12], the possible phase reactions occurring in the alloy of this study are listed in Table 6.2.

It is interested to notice that two iron-rich intermetallics, Al_mFe and Al_7Cu_2Fe, are found to

form in the alloy of this study as shown by Peaks 2-4 through eutectic reactions.

Fig. 6.1 (a) TA and (b) DSC curves for the alloy of this study

Table 6.2 Possible solidification reactions in the experimental 206 alloy of this study

Peak	Reaction	Temperature K (°C)*	Stage
1	Development of aluminum dendrite [6, 13, 14]	921 (648)	Dendritic
2	Liq. →Al + Al_mFe	902(629)	Post-dendrite
3	Liq. →Al + Al_7Cu_2Fe [13]	868 (595)	Pre-eutectic
4	Liq.→Al + Al_2Cu+ Al_7Cu_2Fe [6, 14]	813 (540)	Eutectic
5	Liq.→Al + Al_2Cu + Al_2CuMg + Mg_2Si[6, 13, 14]	783 (510)	Post-eutectic

Notes: The peak numbers are corresponded to those as indicated in Fig. 6.1.

* Temperatures are determined from the DSC heating curves when the slope of dH/dT changes [8], which eliminate the undercooling effect.

As shown in Fig. 6.2a, the intermetallics in this study have two different

morphologies (Chinese script and platelet) indicating two kinds of iron-rich intermetallic

compounds present in the fully solidified structure: Al_mFe and Al_7Cu_2Fe (β-Fe). In the

Furthermore, the peak intensity of pre-eutectic β-Fe (peak 3) is much weaker in Alloy 2 than in Alloy 1. Additionally, the formation temperature of the pre-eutectic β-Fe phase in Alloy 2 is also lower, about 853 K (580 °C) in Alloy 2 and 863 K (590 °C) in Alloy 1, indicating that the formation of the β-Fe phase has been effectively suppressed in Alloy 2. In summary, addition of Mn and/or Si favors the formation of the α-Fe phase but suppresses the β-Fe phase and that Mn is a more effective neutralization agent than Si. The combined addition of both Mn and Si is even more effective than the individual addition of either Mn or Si.

5.4 Summary

(1) The two main iron-rich intermetallic phases present in the final microstructure of Al-4.5Cu-0.3Fe alloys are platelet β-Fe, $Al_7Cu_2(FeMn)$ or Al_7Cu_2Fe and Chinese script α-Fe, $Al_{15}(FeMn)_3(SiCu)_2$. The α-Fe phase precipitates in the post-dendritic stage at 883~898 K (610~625 °C). The β-Fe phase can form in both the pre-eutectic stage at 858~838 K (585~595 °C), or eutectic stage at 803~813 k (530~540 °C), termed as pre-eutectic β-Fe $(Al_7Cu_2(FeMn))$ and eutectic β-Fe (Al_7Cu_2Fe), respectively.

(2) All the solidification reactions, precipitation temperatures and resulted microstructures and Fe-rich intermetallic phases possibly appearing in A206 alloys are

summarized as an important complement for the prior works in the literature about the solidification of A206 alloys.

(3) The nucleation of the Fe-rich phases is performed through the direct deposition onto the proposed substrates and/or the classic peritectic reactions.

(4) Both α-Fe and β-Fe phases can nucleate on the oxide films. It is found that α-Fe can also nucleate on $Al_6(FeMnCu)$ and Al_3Ti particles. In addition, the earlier formed α-Fe phase can also nucleate the later formed β-Fe phase. Several lattice matches have been found through the calculation of the planer disregistries between the substrates and the Fe-rich intermetallic phases. The planar disregistries calculated are all lower than 10 pct indicating potentially positive nucleation as proposed. A nucleation hierarchy has been outlined in Al-4.5Cu-0.3Fe cast A206 type alloys.

(5) Either Si or Mn favors the transformation of β-Fe into the α-Fe phase. Moreover, Mn is a more effective neutralization agent than Si. The individual addition of either Si or Mn cannot completely transform β-Fe into the α-Fe phase even at a high Mn/Fe level of 1.33 or a Si/Fe level of 1.0.

(6) At a combination of both high Mn and high Si, almost all β-Fe platelets can be converted into Chinese script α-Fe. For a cast Al-4.5Cu-0.3Fe alloy, 0.3% Mn and 0.3% Si are required to completely suppress the β-Fe phase.

References

[1] A. M. Samuel, F. H. Samuel and H. W. Doty: *J. Mater. Sci.*, 1996, Vol. 31, pp. 5529-5539.

[2] A. M. Samuel, A. Pennors, C. Villeneuve, F. H. Samuel, H. W. Doty and S. Valtierra: *Int. J. Cast Met. Res.*, 2000, Vol. 13, pp. 231-253.

[3] S. Murali, K. S. Raman and K. S. S. Murthy: *Mater. Sci. Eng., A*, 1995, Vol. 190, pp. 165-172.

[4] L. Lu and A. K. Dahle: *Metall. Mater. Trans. A*, 2005, Vol. 36, pp. 819-835.

[5] W. Khalifa, F. H. Samuel, J. E. Gruzleski, H. W. Doty and S. Valtierra: *Metall. Mater. Trans. A*, 2005, Vol. 36, pp. 1017-1032.

[6] G. Gustafsson, T. Thorvaldssons and G. L. Dunlop: *Metall. Mater. Trans. A*, 1986, Vol. 17 A, pp. 45-52.

[7] J. Y. Hwang, H. W. Doty and M. J. Kaufman: *Mater. Sci. Eng., A*, 2008, Vol. 488, pp. 496-504.

[8] S. G. Shabestari: *Mater. Sci. Eng., A*, 2004, Vol. 383, pp. 289-298.

[9] C. M. Dinnis, J. A. Taylor and A. K. Dahle: *Scripta Materialia*, 2005, Vol. 53, pp. 955-958.

[10] N. Roy, A. M. Samuel and F. H. Samuel: *Metall. Mater. Trans. A*, 1996, Vol. 27, pp. 415-429.

[11] L. Bäckerud, *Solidification characteristics of aluminum alloys*, Skanaluminium, Universitetsforlaget AS, Oslo, Norway, 1986.

[12] M. Talamantessilva, A. Rodriguez, J. Talamantessilva, S. Valtierra and R. Colas: *Mater. Charact.*, 2008, Vol. 59, pp. 1434-1439.

[13] C. J. Tseng, S. L. Lee, S. C. Tsai and C. J. Cheng: *J. Mater. Res.*, 2002, Vol. 17, pp. 2243-2250.

[14] C. J. Tseng, S. L. Lee, T. F. Wu and J. C. Lin: *Mater. Trans., JIM*, 2000, Vol. 41, pp. 708-713.

[15] G. K. Sigworth: 2002, Vol. pp. 22-25.

[16] N. A. Belov, A. A. Aksenov and D. G. Eskin, *Iron in aluminum alloys: impurity and alloying element*, Taylor & Francis, London, 2002.

[17] G. K. Sigworth: *Mod. Cast.*, 1987, Vol. 77, pp. 23-25.

[18] X. Cao and J. Campbell: *Metall. Mater. Trans. A*, 2004, Vol. 35 A, pp. 1425-1435.

[19] X. Cao and J. Campbell: *Can. Metall. Q.*, 2005, Vol. 44, pp. 435-448.

[20] X. Cao and J. Campbell: *Mater. Trans., JIM*, 2006, Vol. 47, pp. 1303-1312.

[21] D. N. Miller, L. Lu and A. K. Dahle: *Metall. Mater. Trans. B*, 2006, Vol. 37, pp. 873-878.

[22] B. L. Bramfitt: *Metall. Trans.* , 1970, Vol. 1, pp. 1987-1995.

[23] J. Campbell, *Castings*, Butterworth-Heinemann, Oxford; Boston, 1991.

[24] X. Cao and J. Campbell: *Metall. Mater. Trans. A*, 2003, Vol. 34, pp. 1409-1420.

CHAPTER 6

IRON-RICH INTERMETALLICS

IN 206 CAST ALLOYS AT 0.5% FE

Chapter 6

Iron-rich intermetallics in 206 cast alloys at 0.5% Fe

6.1 Introduction

As discussed in Chapters 4 and 5, the platelet β-Fe and Chinese script α-Fe phases can form during solidification, depending on the alloys compositions, such as Mn and Si contents. The solidification sequence and possible nucleation mechanism have been dealt with in detail. It is also found that the addition of Mn and/or Si, or the increase of the cooling rate can promote the formation of Chinese script α-Fe and inhibit the precipitation of platelet β-Fe.

The major content in this chapter were published as:

6.2: K. Liu, X. Cao, X.-G. Chen, "A new iron-rich intermetallic--AlmFe phase formed in Al-4.6Cu-0.5Fe cast alloy", Metallurgical and Materials Transaction A, 2012, 43A (4): 1097-1101;

6.3: K. Liu, X. Cao, X.-G. Chen, "Precipitation of iron-rich intermetallic phases in Al-4.6Cu-0.5Fe-0.5Mn cast alloy", Journal of Materials Science, 2012, 43 (10): 4290-4298;

6.4: K. Liu, X. Cao, X.-G. Chen, "Formation and phase selection of iron-rich intermetallics in Al-4.6Cu-0.5Fe cast alloys", Metallurgical and Materials Transaction A, 2012, on-line published, DOI: 10.1007/s11661-012-1419-7.

To date, the very limited investigations have indicated that the existence of diverse iron-rich intermetallics in 206 alloys at a high Fe level of 0.5%. The formation and phase selection of these intermetallics will certainly depend on the alloy chemistry and solidification conditions. Al_mFe is one of the most widely observed iron-rich intermetallics in AA1xxx and AA5xxx wrought aluminum alloys [1-4]. It was reported to precipitate at high cooling rate compared with other iron-rich intermetallics, such as Al_3Fe and Al_6Fe in Al-Fe-Si ingots [1, 2, 5]. However, Al_mFe has never been reported in A206 cast aluminum alloys. Mondolfo [6] mentioned that Chinese script $Al_3(FeMn)$ phase was possible to appear in the Al-Cu cast alloy with 5%Cu and 0.55%Fe if the Si level was much lower than the Fe content but no evidence was presented.

The phase selection among iron-rich intermetallic Al_3Fe, Al_6Fe and Al_mFe (i.e. $Al_3(FeMn)$, $Al_6(FeMn)$ and $Al_m(FeMn)$ in the presence of Mn, respectively) has been frequently encountered in the Al-Fe binary alloy system, such as AA1XXX alloys during Direct Chill (DC) casting [2, 7, 8]. Generally, Al_3Fe is reported as the equilibrium phase while Al_6Fe and Al_mFe are the metastable iron-rich intermetallics in Al-Fe and Al-Fe-Si systems. The formation of the iron-rich intermetallic phases can be predicted and manipulated to obtain the favorable microstructures and the associated mechanical properties through the careful control of the alloy chemistry and solidification conditions [2,

7]. In addition, many researchers [8-11] have investigated the effect of cooling condition and growth velocity on the intermetallic phase selection. Generally, a high solidification velocity can enhance the formation of $Al_m(FeMn)$ and $Al_6(FeMn)$ phases over $Al_3(FeMn)$. Therefore, the Al_3Fe precipitates at a low cooling rate and Al_mFe at a high cooling rate while Al_6Fe at a moderate cooling rate [12].

However, very limited investigations about the phase formation and the phase selection among the various iron-rich intermetallics have been performed in 206 alloys at 0.5% Fe. To design and develop new Al-Cu 206 cast alloys with a high allowable iron content, this part is concentrated on the formation and phase selection of the iron-rich intermetallics in 206 cast alloys at 0.5% Fe over various cooling rates and alloy compositions (Si and Mn contents).

The chemical compositions of the experimental alloys used were analyzed by using an Optical Emission Spectrometer (OES) and are shown in Table 6.1. The details of solidification can be found in Chapter 3.

Since the cooling rate, particularly during slow cooling, can be accurately controlled in the DSC test, this technique was used to investigate the effect of cooling rate on the phase selection of the iron-rich intermetallic phases in this work. The DSC samples were taken from the solidified thermal analysis (TA) ingot samples at 12 K per minute (KPM)

and then rapidly heated to 700 °C at 125 KPM. After holding at 700 °C for 5 minutes, the samples were then cooled at 1, 5, 10 and 50 KPM. The solidified DSC samples were carefully mounted and polished for metallographic observations.

Table 6.1 Chemical composition of 206 alloys at 0.5% Fe used in this work

Alloy #	Elements （wt. %)						
	Cu	Mg	Fe	Si	Mn	Ti	Al
1	4.58	0.28	0.51	0.07	0.003	0.01	Bal.
2	4.60	0.32	0.49	0.09	0.11	0.01	Bal.
3	4.61	0.32	0.49	0.19	0.22	0.01	Bal.
4	4.65	0.30	0.51	0.31	0.30	0.01	Bal.
5	4.62	0.28	0.50	0.48	0.10	0.01	Bal.
6	4.59	0.30	0.52	0.49	0.51	0.01	Bal.
7	4.68	0.31	0.51	0.11	0.53	0.01	Bal.

In this chapter, OM, SEM, TEM were used to observe the microstructures and identify the iron-rich intermetallics while TA and DSC were performed to distinguish and confirm the solidification sequences of iron-rich intermetallics. Details of these methods were shown in Chapter 3.

6.2   Formation of Al_mFe in Al-4.6Cu-0.5Fe-0.07Si 206 cast alloy

Fig. 6.1 shows the TA cooling, and DSC heating and cooling curves of the alloy used in this study. It can be found that there are 5 peaks appearing during the heating or cooling. Based on the present and earlier systematic metallographic observations [13], as well as those work of Backerud et $al.$ [14] and Mondolfo [6], and ternary Al-Cu-Fe phase diagram

[12], the possible phase reactions occurring in the alloy of this study are listed in Table 6.2. It is interested to notice that two iron-rich intermetallics, Al_mFe and Al_7Cu_2Fe, are found to form in the alloy of this study as shown by Peaks 2-4 through eutectic reactions.

Fig. 6.1 (a) TA and (b) DSC curves for the alloy of this study

Table 6.2 Possible solidification reactions in the experimental 206 alloy of this study

Peak	Reaction	Temperature K (°C)*	Stage
1	Development of aluminum dendrite [6, 13, 14]	921 (648)	Dendritic
2	Liq. $\rightarrow$Al + Al_mFe	902(629)	Post-dendrite
3	Liq. $\rightarrow$Al + Al_7Cu_2Fe [13]	868 (595)	Pre-eutectic
4	Liq.$\rightarrow$Al + Al_2Cu+ Al_7Cu_2Fe [6, 14]	813 (540)	Eutectic
5	Liq.$\rightarrow$Al + Al_2Cu + Al_2CuMg + Mg_2Si[6, 13, 14]	783 (510)	Post-eutectic

Notes: The peak numbers are corresponded to those as indicated in Fig. 6.1.

* Temperatures are determined from the DSC heating curves when the slope of dH/dT changes [8], which eliminate the undercooling effect.

As shown in Fig. 6.2a, the intermetallics in this study have two different morphologies (Chinese script and platelet) indicating two kinds of iron-rich intermetallic compounds present in the fully solidified structure: Al_mFe and Al_7Cu_2Fe (β-Fe). In the

deeply-etched samples, the Chinese script Al_mFe has a 3-D compact branched shape, as shown in Fig. 6.2b, slightly different from the reported 3-D morphology of the Al_mFe phase in AA1xxxx alloy where it was observed to appear as a fine feathery shape with many curved branches growing out from the center nucleus into the Al interdendritic space [3].
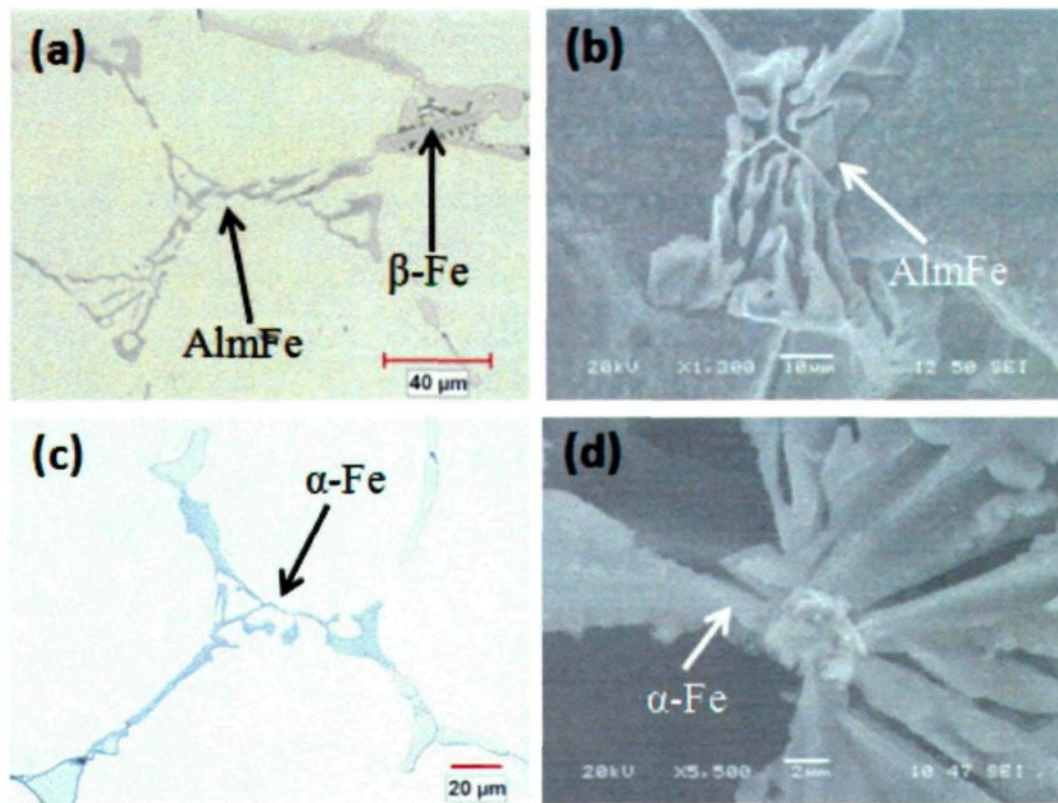
Fig. 6.2 Non-etched and deeply-etched microstructures for AlmFe (a-b) obtained in this study and α-Al15(FeMn)$_3$(SiCu)$_2$ (c-d) obtained in Al-4.5Cu-0.3Fe-0.2Mn-0.2Si alloy

Careful metallographic observations indicate that the Chinese script Al_mFe obtained in the alloy of this study (Fig. 6.2a-b) is different from the well known Chinese script α-Fe (α-Al$_{15}$(FeMn)$_3$(SiCu)$_2$). The typical morphology of α-Fe obtained in

Al-4.5Cu-0.3Fe-0.2Mn-0.2Si is shown in Fig. 6.2c-d. Both Al_mFe and α-Fe phases have

Chinese script shape but there are some differences in the 3-D morphologies. For α-Fe, it

looks much more like a dendrite form with large primary and fine secondary branches (Fig.

6.2d). However, Al_mFe is more compact as shown in Fig. 6.2b and is hard to distinguish the

primary and secondary branches. In addition, the precipitation temperature of the Al_mFe in

the present alloy of this study (902 K (629 °C)) is much higher than that of the α-Fe phase

in A206 cast alloy with 0.3% Fe (883~898 K (610~625 °C)) [13].

In order to distinguish the two Chinese script intermetallics, SEM-EDS, EBSD and

TEM are performed to characterize them. The phase compositions measured using

SEM-EDS show that there exist significant differences in Si and Fe contents for the two

intermetallics. For the Chinese script α-Fe obtained in Al-4.5Cu-0.3Fe-0.2Mn-0.2Si alloy,

Si (6.25 ± 0.18 at. %) is one of the main component elements in α-Fe but Fe (13.11 ± 0.24

at. %) is relatively low. However, almost no Si is detected in Al_mFe and the Fe content

(17.55 ± 0.33 at. %) is higher for Al_mFe in this study. The ratio of Al/Fe of the Al_mFe in the

alloy of this study is about 4.2 while it is about 5.0 in α-Fe.

The EBSD patterns and simulation results of the two phases are shown in Fig. 6.3.

Fig. 6.3b and Fig. 6.3e are the indexed experimental EBSD patterns for the two phases

while Fig. 6.3c and Fig. 6.3f are the simulation results calculated by Channel 5 software. In

EBSD, the Mean Angular Deviation (MAD) between the experimental and calculated patterns represents the accuracy of the solution provided by the software, where a smaller value indicates a closer match between the experimental and simulated Kikuchi bands. Normally, MAD, lower than 0.7, is considered desirable for an accurate solution [15]. As shown in Fig. 6.3, the MAD values are 0.168 and 0.143 for Al_mFe and α-Fe, respectively, indicating that the accurate solutions are obtained for the two phases, confirming the presence of the Al_mFe phase in the alloy of this study. The EBSD pattern is related to the crystal structure and the atom position in lattice. The crystal structures are reported to be body centered tetragonal (bct) for Al_mFe [5, 13, 16, 17] and body-centre cubic (bcc) for α-Fe [13, 18, 19]. The difference in crystal structure results in the different EBSD patterns and hence the two iron-rich phases can easily be distinguished using EBSD. Therefore, it is evident that the Chinese script phase formed in the alloy of this study is Al_mFe rather than the α-Fe phase, which is observed in typical A206 Al-Cu casting alloys [13, 20].
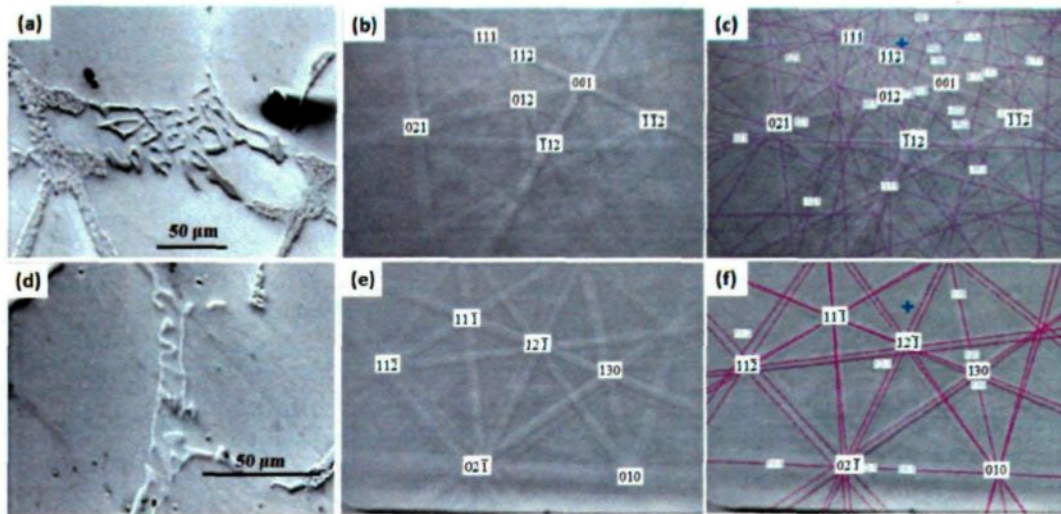
Fig. 6.3 Phase morphology, EBSD pattern and simulation results for
(a-c) Al_mFe (MAD = 0.168) and (d-f) α-Fe (MAD = 0.143)

In order to further confirm the Al_mFe phase, TEM was performed on the sample which was water quenched at 883 K (610 °C) (after Peak 2 in Fig. 6.1) in this study. Fig. 6.4 shows the micro-image of Al_mFe and its two selected area diffraction patterns (SADPs) along [110] and [210] directions. From the SADPs, it can be found that there are some extra reflection spots parallel to the [110] direction. It is reported that the streaks and extra reflection spots are commonly observed in the crystal of Al_mFe, mainly due to such defects as twining and stacking fault, both of which are considered to be intrinsic in its structure [5, 17]. The results of the SADPs confirm the crystal structure of the Al_mFe phase which has a body centered tetragonal unit cell with lattice parameters a 0.884 nm and c 2.160 nm [2, 4, 5].
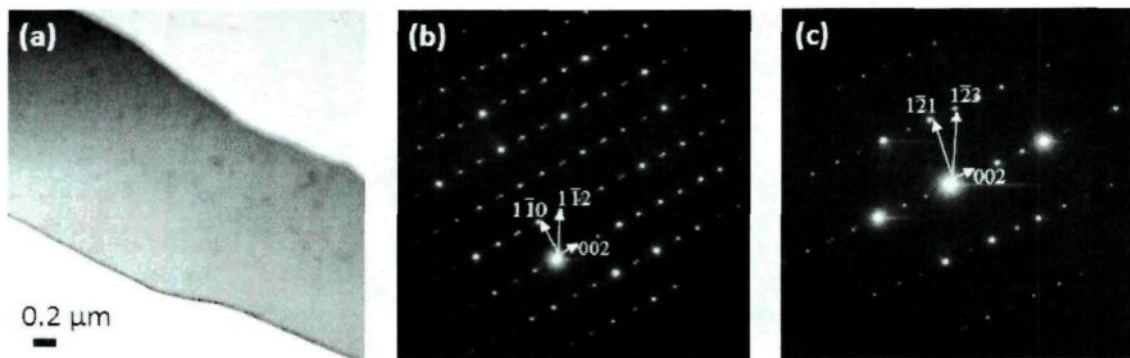
Fig. 6.4 (a) TEM micro-image of Al$_m$Fe,
and its SADPs along (b) [110] and (c) [210] directions

EDS on TEM also is performed to verify the compositions of the Al$_m$Fe phase. The results show that the Al$_m$Fe phase has the compositions of $(68.53 \pm 0.39)\%$ Al- $(16.33 \pm 0.27)\%$ Fe - $(14.39 \pm 0.39)\%$Cu and the ratios of Al/Fe lie between 4.1 and 4.3 with the average value of m being about 4.2, which is very close to the constitutions of the Al$_m$Fe phase with m 4.0~4.4 [2, 4], further confirming the presence of Al$_m$Fe phase in the alloy of this study.

All the results of SEM, EBSD and TEM show that the Chinese script Fe phase obtained in the alloy of this study at 0.5% Fe is Al$_m$Fe. It should be emphasized that, to the author's knowledge, Al$_m$Fe phase has never been reported in the Al-Cu A206 family alloys. Additionally, it is not shown in the Al-Cu-Fe phase diagram [6, 12] or any simulated phase diagrams. It can be easily confused with the α-Fe phase as typically observed in the A206 alloy [13, 20] due to the similar morphology in the optical microstructure. However, the

two phases can be distinguished using SEM-EDS and EBSD due to their differences in chemical compositions and crystal structures.

The measured formation temperature of the Al_mFe phase in this study obtained from the DSC heating curve is about 902 K (629 °C), which is lower than the reported value, 922 K (649 °C) [2] or 918 K (645 °C) [1] for AA 1xxx alloys, probably due to the high content of Cu in A206 cast alloy, compared with AA1xxx and AA5xxx alloys. As is well known, the addition of Cu can reduce the liquids temperature [21-23]. Therefore, the A206 cast alloy has lower liquids temperature and the associated Al_mFe phase is also expected to precipitate at a lower temperature in the A206 than that in the AA1xxx and AA5xxx alloys. In addition, the Al_mFe phase was reported to precipitate preferably at high cooling rate (>10 K/s) [2, 5, 17]. However, the present investigation indicates that it can precipitate at a cooling rate as low as 0.2 K/s. Moreover, the image analysis results show that the total volume of the iron-rich intermetallic phases in the alloy of this study are approximately 2.1 ± 0.58 vol. % , which consists of 81 vol. % Chinese script Al_mFe and 19 vol. % platelet-like Al_7Cu_2Fe indicating that Chinese script Al_mFe phase is the dominant iron-rich intermetallic in the alloy used in this study. As is well known, A206 cast family alloys require extremely low iron contents (< 0.15%) to avoid the harmful effect caused by brittle platelet iron-rich intermetallic phase [24, 25]. To neutralize its detrimental effect, Mn is often added to

transform the platelet form to Chinese script morphology which has been thought to be less

detrimental to the mechanical properties of the castings [13, 20, 26]. In this work, the

Chinese script Al_mFe is observed to be the dominant iron-rich intermetallic phase even at a

high iron level of 0.5% and low contents of Si (0.1%) and Mn (0.003%). The influence of

the Al_mFe phase on the mechanical properties of A206 cast alloys has not been investigated

yet but it is expected that it may behave similar with the Chinese script α-Fe phase due to

their similar morphology. This important finding indicates that the commercially important

A206 family cast alloys can still obtain the preferred Chinese script microstructures at high

Fe with low level of Mn and Si, even at a low cooling rate of 0.2 K/s. Hence the design and

development of some new high iron A206 cast alloys might become feasible.

6.3   Formation of Al_3Fe in Al-4.6Cu-0.5Fe-0.5Mn-0.1Si 206 cast alloy

6.3.1   Identification of iron-rich intermetallic phases

Fig. 6.5 shows the iron-rich intermetallics precipitated during the solidification in the

experimental alloy. It can be found that there are two typical kinds of iron-rich intermetallic

morphologies, i.e. platelet-like (A and C) and Chinese script (B).
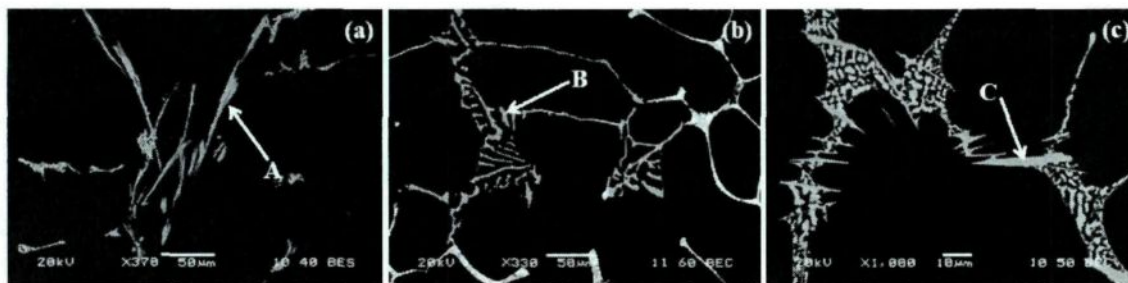
Fig. 6.5 Typical iron-rich intermetallic phases precipitated in the experimental alloy

In order to definitely identify the iron-rich intermetallic phases with the two kinds of morphologies, the combined use of both EDS and EBSD on SEM are performed, which can improve the phase differentiation process by collecting chemical information from EDS and simultaneously the crystallography information from EBSD [27]. The SEM-EDS results (with one standard deviation) are shown in Table 6.3.

Table 6.3 Compositions of the iron-rich intermetallic phases obtained using SEM-EDS

Phase	Element (at. %)			
	Al	Mn	Fe	Cu
A	76.62 ± 0.48	3.20 ± 0.38	17.50 ± 0.43	2.68 ± 0.27
B	83.56 ± 0.58	2.89 ± 0.31	11.00 ± 0.47	2.56 ± 0.34
C	72.74 ± 0.51	1.98 ± 0.28	6.31 ± 0.31	18.96 ± 0.53

As shown in Table 6.3, the main differences between the phase A and the phase B are the levels of Fe. The Fe content in the phase A (17.50 at. %) is much higher than that in the phase B (11.00 at. %). The ratio of Al/(Fe+Mn) in the phases A and B is 3.7 and 5.9, respectively, probably indicating the $Al_3(FeMn)$ for the phase A and $Al_6(FeMn)$ for the

phase B [4]. The Al: Cu: (Fe+Mn) atom ratios in the phase C is approximately 7:2:1, suggesting the phase C as $Al_7Cu_2(FeMn)$ (β-Fe).

The EBSD results of phases A, B and C are shown in Fig. 6.6. Fig. 6.6a, 6.6d and 6.6g are the phase morphologies while the corresponding experimental patterns are displayed in Fig. 6.6b, 6.6e and 6.6h. Fig. 6.6c, 6.6f and 6.6i are the simulated patterns.
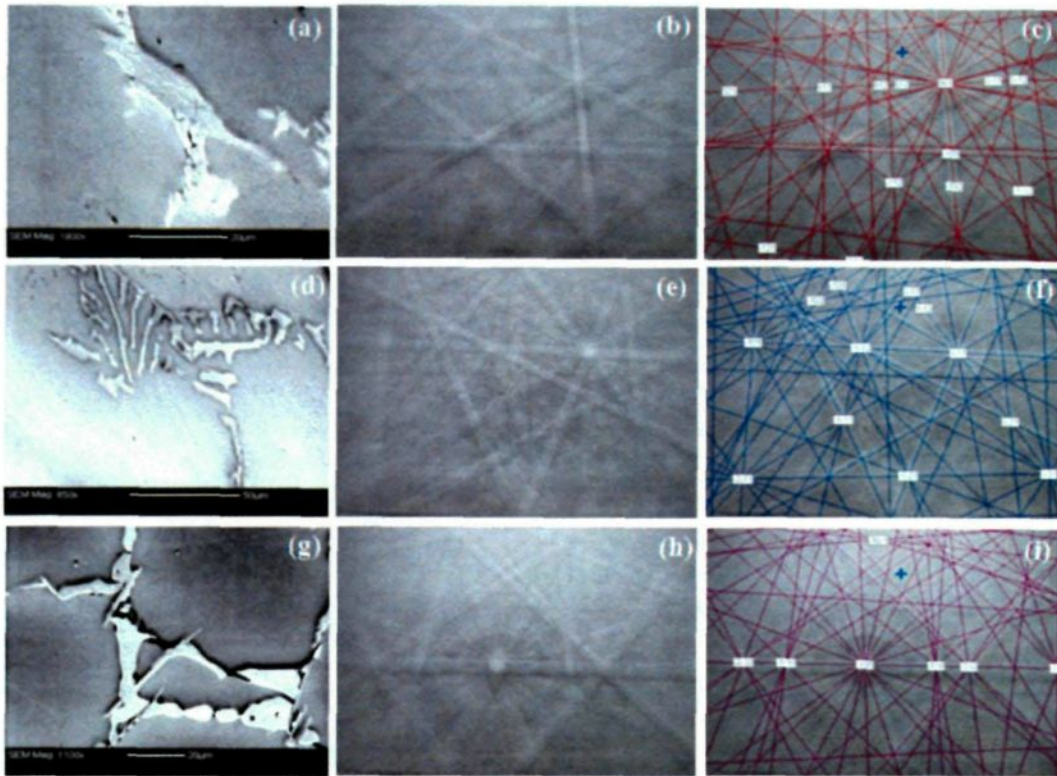

Fig. 6.6 Morphologies, EBSD patterns and simulated results of iron-rich intermetallics;
(a), (b) and (c) for $Al_3(FeMn)$ (MAD=0.223);
(d), (e) and (f) for $Al_6(FeMn)$ (MAD=0.155);
(g), (h) and (i) for $Al_7Cu_2(FeMn)$ (MAD=0.192)

In EBSD, the Mean Angular Deviation (MAD) between the experimental and the calculated patterns represents the accuracy of the solution given by the software, where a smaller value indicates a closer match between the experimental and the simulated patterns. Normally, a MAD value of lower than 0.7 is considered to be desirable for an accurate solution [15]. As shown in Fig. 6.6c and 6.6f, the MAD values for phase A and phase B are 0.223 and 0.155, respectively, much lower than 0.7 and thus confirming the EDS results, i.e. the platelet phase A is $Al_3(FeMn)$ and the Chinese script phase B is $Al_6(FeMn)$. In addition, the EBSD results also confirm the presence of $Al_7Cu_2(FeMn)$ with a MAD value of 0.192, as shown in Fig. 6.6i.

Both $Al_3(FeMn)$ and $Al_7Cu_2(FeMn)$ phases are observed to be platelet-like in the 2-D morphology, as shown in Fig. 6.5a and 6.5c, resulting in some confusions between the two phases. However, the combination of both EDS and EBSD can be used to distinguish them in spite of their similar morphology. The EBSD pattern is generally related to the crystal structure and the atom position in the lattices. The crystal structures were reported to be monoclinic for Al_3Fe with lattice parameters a 1.549 nm, b 0.808 nm, c 1.249 nm and β 107.75° [2], and tetragonal for Al_7Cu_2Fe with a 0.6336 nm and c 1.4879 nm [12]. The difference of the iron-rich intermetallics in the crystal structure results in the different EBSD patterns, as shown in Fig. 6.6. Together with the differences in the phase

compositions obtained from EDS, as shown in Table 6.3, the platelet-like $Al_3(FeMn)$ and $Al_7Cu_2(FeMn)$ phases can be clearly distinguished by the combined use of EBSD.

The results of both EDS and EBSD show that $Al_3(FeMn)$, $Al_6(FeMn)$ and $Al_7Cu_2(FeMn)$ can precipitate during solidification in the experimental alloy. However, only $Al_3(FeMn)$ and $Al_7Cu_2(FeMn)$ are found to be present in the fully solidified experimental alloy indicating that $Al_6(FeMn)$ disappears during the later solidification, which will be dealt with later.

To further confirm the presence of $Al_3(FeMn)$, TEM is used to investigate the crystal structure of the phase, as shown in Fig. 6.7. Fig. 6.7a displays the nearly half transverse section of $Al_3(FeMn)$ extracted from the particle shown in Fig. 6.5a using FIB technique. The high magnification cross section of the $Al_3(FeMn)$ particle consists of several faceted segments which exhibits a rod-like morphology. Some twinning is observed in each segment. The similar segment shape and twining were also reported in Al-Fe alloys [28, 29]. In the research of Sahoo et al. [29], they found that Al_3Fe can appear as a dendrite with ten branches in a rapidly solidified Al-8.3% Fe-0.8% V alloy. The formation of the branches is due to the $(20\bar{1})$ and (100) twining. From the SADP shown in Fig. 6.7c, it can be found that there are strong streak lines parallel to the [001] direction. The reflection spots have smeared into a coarse line on some planes, indicating the pronounced stacking

faults in Al_3(FeMn) phase [4, 16, 30, 31]. The results of the SADPs (Fig. 6.7b and 7c) confirm the crystal structure of the Al_3(FeMn) which has a monoclinic unit cell with lattice parameters a 1.549 nm, b 0.808 nm, c 1.248 nm and β 107.75° [2].
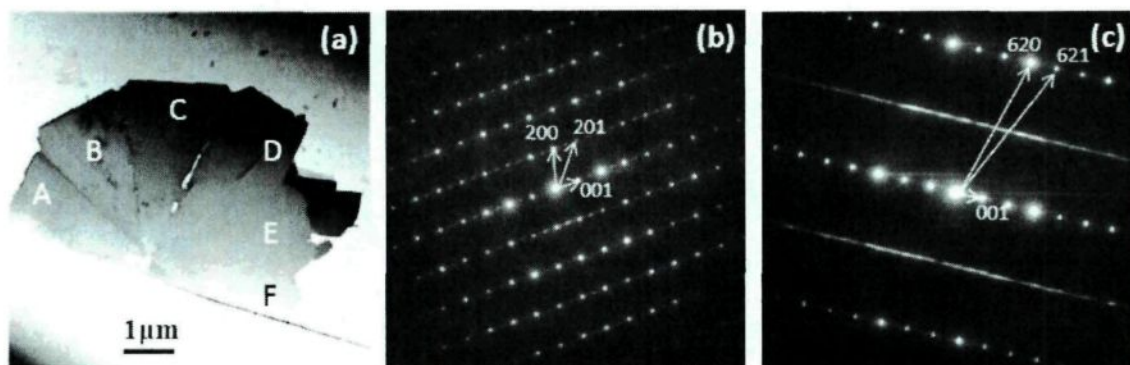
Fig. 6.7 (a) TEM microimage of the Al_3(FeMn) phase,
and its SADPs along (b) [010] and (c) [$\bar{1}$30] directions

EDS on TEM is also performed to verify the chemical compositions of the Al_3(FeMn) phase. Each segment displayed in Fig. 6.7a has been checked and the results are shown in Table 6.4. It can be found that the ratios of Al/(Fe+Mn) lie between 3.25 and 3.4 with the average value being about 3.36, which is very close to the constitutions of the Al_3(FeMn) phase [2, 4], further confirming the presence of Al_3(FeMn) phase in the experimental alloy.

Table 6.4 Chemical compositions of Al_3(FeMn) obtained using TEM-EDS (at. %)

Segment	Al	Mn	Fe	Cu	Al: (Fe+Mn)
A	68.54	5.28	14.88	11.29	3.40
B	68.90	4.09	16.26	10.75	3.39
C	68.14	4.88	15.42	11.57	3.36
D	68.05	4.76	16.21	10.97	3.25
E	68.83	4.84	15.07	11.26	3.46
F	68.34	5.11	15.53	11.03	3.31
Avg.	68.47	4.83	15.56	11.15	3.36

Al_3Fe or $Al_3(FeMn)$ in the presence of Mn is one of the most frequently observed iron-rich intermetallics in Al-Fe or Al-Fe-Si alloys [2, 3, 32-34] but has seldom been reported in Al-Cu cast alloys. In the classic reference of Mondolfo [6] a Chinese script $Al_3(FeMn)$ was mentioned to appear in Al-5Cu-0.55Fe alloy but no evidence was given. However, the $Al_3(FeMn)$ phase is found to precipitate as platelets in the present work, similar to the morphology as reported in AA1xxx and AA5xxx alloys [2, 3].

The examination in this study shows that majority of the $Al_3(FeMn)$ phase has a regular straight platelet shape, as shown in Fig. 6.5a. Its typically 3-D morphology is shown in Fig. 6.8a. It is observed that, in spite of the rigid platelet-like shape, $Al_3(FeMn)$ may change its growth direction through the branch mechanism to adapt to the irregular interderdendritic space between the aluminum cells. It was reported that Al_3Fe had a strong tendency to twin [12, 31, 35], which can lead to easily branch from one platelet to the other one. Fig. 6.8b and 6.8c display the $Al_3(FeMn)$ phase with branches in different growth directions, resulting from the twining characteristics. It can be found that the two parallel branches grow with a small angle as shown in Fig. 6.8b, while $Al_3(FeMn)$ with branches in a large angle is occasionally observed in the experimental alloy, as displayed in Fig. 6.8c, which was reported to be the result of (100) and (001) twining [35].
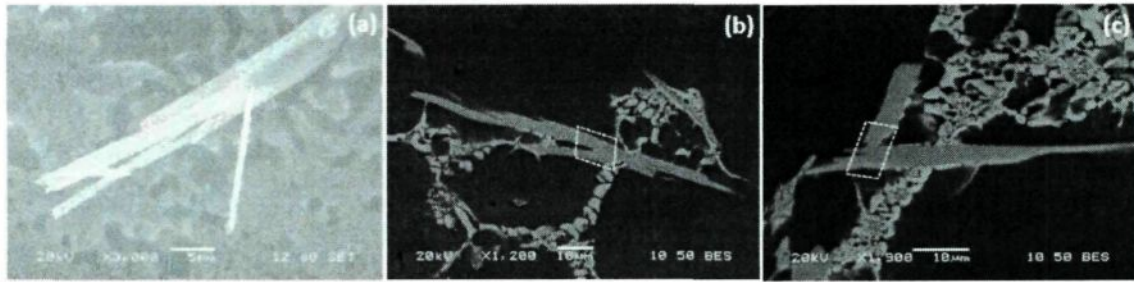
Fig. 6.8 3-D morphology for $Al_3(FeMn)$ phase with straight interfaces (a)
and $Al_3(FeMn)$ phase with branches (b and c)

6.3.2 Solidification characteristics of iron-rich intermetallics

Fig. 6.9 shows the TA cooling curve and DSC heating and cooling curves with their

first derivates for the experimental alloy. It can be found that there are 5 peaks appearing in

both the TA cooling and the DSC heating and cooling curves. According to the metallurgic

observations in this study combined with the reactions reported in literatures [13, 14, 20],

the precipitation of the iron-rich intermetallics takes place in Peaks 2 to 4 for the

experimental alloy.
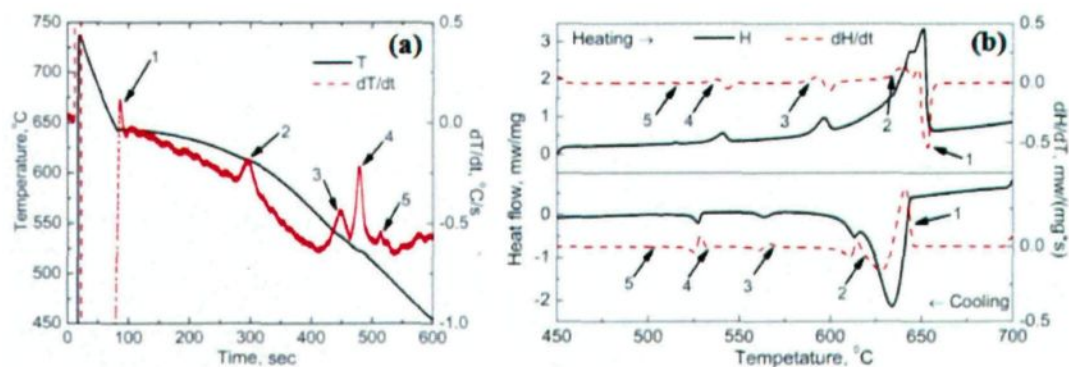
Fig. 6.9 TA cooling curve (a) and DSC heating & cooling curves (b)
of experimental alloy

In order to establish the precipitation sequence of the iron-rich intermetallic phases,

the interrupted quench technique has been performed at 615 °C (after Peak 2), 550 °C (after

Peak 3) and 520 °C (after Peak 4) on the thermal analysis samples. The microstructures

obtained after the interrupted quench are shown in Fig. 6.10.
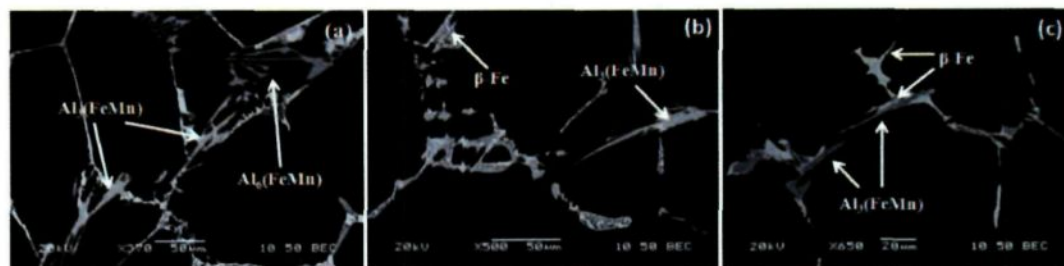
Fig. 6.10 Microstructures of the experimental alloy after water quenched at
(a) 615 °C, (b) 550 °C and (c) 520 °C

As shown in Fig. 6.10a, the platelet Al_3(FeMn) and Chinese script Al_6(FeMn) are

observed to coexist in the sample after water quenched at 615 °C. The image analysis

results show that the platelet Al_3(FeMn) is the principal iron-rich intermetallic particles (97

vol. % of the total iron-rich intermetallics) with only 3 vol. % $Al_6(FeMn)$ being present. Moreover, $Al_6(FeMn)$ disappears and only $Al_3(FeMn)$ and β-Fe ($Al_7Cu_2(FeMn)$/ Al_7Cu_2Fe) are found to be present in the samples after water quenched at 550°C and 520°C, as shown in Fig. 6.10b and 6.10c.

Based on the present and earlier systematic metallographic observations [13], as well as those work of Bäckerud *et al.* [14] and Mondolfo [6], and the ternary Al-Cu-Fe phase diagram [12], the possible solidification reactions occurring in the present experimental alloy are listed in Table 6.5.

The formation temperature of $Al_3(FeMn)$ is found to be about 640 °C obtained from the DSC heating curve, which is lower than the reported value of 654 °C [1, 2] in AA1xxx alloy, probably due to the high content of Cu in 206 cast alloys compared with AA1xxx alloys. As is well known, the addition of Cu can reduce the liquids temperature [21, 22, 36]. Therefore, the 206 cast alloy has lower liqudus temperature and thus the associated $Al_3(FeMn)$ phase is also expected to precipitate at a lower temperature in 206 cast alloy than that in AA1xxx alloys.

Table 6.5 Possible solidification reactions in the experimental 206 alloy

Peak	Reaction	Temperature (°C)*
1	Development of aluminum dendrite	648
2	a) Liq.→Al + Al$_3$(FeMnCu) b) Liq.→Al + Al$_6$(FeMnCu)	640
3**	a) Liq. + Al$_3$(FeMnCu)→Al + Al$_7$Cu$_2$(FeMn) b) Liq. + Al$_6$(FeMnCu)→Al + Al$_7$Cu$_2$(FeMn) c) Liq.→Al + Al$_7$Cu$_2$(FeMn)	595
4	Liq.→Al + Al$_2$Cu + Al$_{20}$Mn$_3$Cu$_2$ + Al$_7$Cu$_2$Fe	540
5	Liq.→Al + Al$_2$Cu + Al$_2$CuMg + Mg$_2$Si	510

Notes: The peak numbers are corresponded to those as indicated in Fig. 6.9.

*Temperatures are determined from the DSC heating curves, which eliminate the undercooling effect.

**The possible reactions to form Al$_7$Cu$_2$(FeMn) in the experimental 206 alloy.

It should be noted that two reactions may overlap in Peak 2. The major reaction is the formation of Al$_3$(FeMn) and the minor one is the occurrence of Al$_6$(FeMn). As shown in Fig. 6.10a, it is observed that a small volume of Al$_6$(FeMn) (3 vol. %) coexists with the dominant Al$_3$(FeMn) in the samples after water quenched at 615 °C, indicating the possible reaction 2B to form Al$_6$(FeMn). However, Al$_6$(FeMn) disappears in the samples after water quenched at 550 °C and 520 °C, as shown in Fig. 6.10b and 10c, indicating the reaction 3b: Liq. + Al$_6$(FeMn)→Al + Al$_7$Cu$_2$(FeMn), similar to the observations in A204.2 alloy at 0.15% Fe [14] and 206 cast alloy at 0.3% Fe [13]. The precipitation of Al$_7$Cu$_2$(FeMn) can also occur through different paths.Al$_3$(FeMn) is occasionally observed to be surrounded by the later formed Al$_7$Cu$_2$(FeMn), as shown in Fig. 6.10c, suggesting the possible transformation from Al$_3$(FeMn) into Al$_7$Cu$_2$(FeMn) by the reaction 3a: Liq. + Al$_3$(FeMn)→Al +

$Al_7Cu_2(FeMn)$. In addition, $Al_7Cu_2(FeMn)$ is often observed to present with no association to $Al_3(FeMn)$ (Fig. 6.5c), indicating the direct formation of $Al_7Cu_2(FeMn)$ from the liquid through the reaction 3c: Liq. $\rightarrow Al + Al_7Cu_2(FeMn)$ [37].

Nevertheless, the $Al_3(FeMn)$ is present as the dominant iron-rich intermetallic phase in the fully solidified microstructure of the experimental alloy. The quantitative results of the image analysis show that the total volume fraction of the iron-rich intermetallic phases in the final microstructure are approximately 2.3 vol. % , which consists of approximately 75 vol. % $Al_3(FeMn)$ and 25 vol. % $Al_7Cu_2(FeMn)$.

In spite of an optimum Fe/Mn of 1, the platelets of $Al_3(FeMn)$ and β-Fe are obtained in the final microstructure indicating that the Mn addition cannot modify the morphology of the platelet intermetallics in Al-Cu 206 alloys , which is completely different from the well known observations that Mn can usually change the platelet iron-rich intermetallic phases into the Chinese script in cast Al-Si alloys [38-40]. The reason is not clear but the formation of dominant $Al_3(FeMn)$ phase in 206 alloy is probably due to the favored phase selection and the iron segregation in the interdenritic regions during the solidification. The segregation of iron in liquid Al can be calculated by the following Scheil equation which is often used to approximate the solute redistribution during non-equilibrium solidification [41]:

$$C_l = C_0(1 - f_s)^{k-1}$$

Where, C_l is the concentration of the solute in liquid; C_0 is the concentration of the solute in the original alloy; f_s is the solid fraction and k is the partition coefficient of the solute.

Fig. 6.11a shows the relationship between solid fraction, solidification temperature and concentration of Fe solute in liquid Al calculated according to the Scheil equation for the experimental alloy. The simulated isopleths phase diagram using Thermo-Calc is also shown in Fig. 6.11b. As shown in Fig. 6.9a (TA cooling curve), the $Al_3(FeMn)$ phase actually begins to form at around 625 °C during solidification. As shown in Fig.6.11a, f_s is about 0.54 at 625 °C. The partition coefficient k of iron in aluminum is reported to be about 0.02~0.03 [42, 43] and C_0 is 0.51%. Then C_l is calculated to be about 1.08-1.09% at 625 °C, as shown in Fig. 6.11a. This value is much higher than the required concentration of iron to form $Al_3(FeMn)$, which is about 0.75% at 625 °C (Fig. 6.11b), indicating that it is possible for the massive formation of $Al_3(FeMn)$ in 206 cast alloy at 0.51% Fe (Peak 2 in Fig. 6.9a).
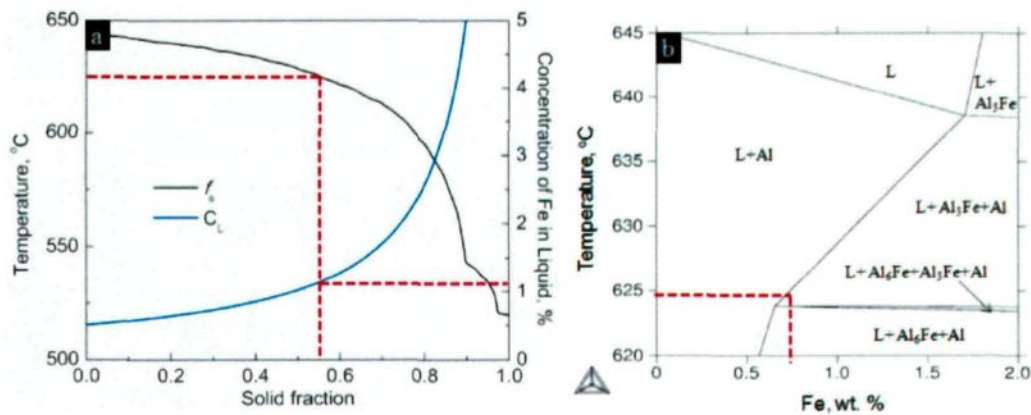
Fig. 6.11 Relationship between f_s and C_L(a) and
simulated isopleths phase diagram from Thermo-Calc (b)

Backerud *et al*. [14] also reported that the Al$_3$Fe is the first iron-rich intermetallic

phase formed in A204.2 Al-Cu cast alloy (Al-4.4Cu-0.15Fe-0.08Mn-0.02Si-0.22Ti).

However, it was believed that all the Al$_3$Fe was transformed into Al$_6$Fe and subsequently

the Al$_6$Fe was transformed into Al$_7$Cu$_2$Fe during the further cooling. In the present work, it

is found that only a very small amount of Al$_6$(FeMn) coexist with the dominant Al$_3$(FeMn)

after the precipitation of Al$_3$(FeMn). This probably resulted from the favored phase

selection at a high Mn content. It was reported that Mn is one of the elements which

promote the formation of Al$_3$Fe and inhibit the formation of Al$_6$(FeMn) in AA1xxx alloy

[44] and AA5005 alloy [45]. In the experimental alloy, Mn content is as high as 0.53%,

which favors to stabilize Al$_3$(FeMn) and inhibits the formation of Al$_6$(FeMn) or the

transformation from Al$_3$(FeMn) to Al$_6$(FeMn). During further cooling, the small amount of

Al$_6$(FeMn) might completely transform into Al$_7$Cu$_2$(FeMn) through Reaction 3b as shown

in Table 6.5. However, the large quantity of $Al_3(FeMn)$ could only partially transform to $Al_7Cu_2(FeMn)$ due to the limited diffusion time available through the peritectic Reaction 3a at low temperature. Hence, $Al_3(FeMn)$ is found to be present and even become the dominant iron-rich intermetallic phase in the fully solidified experimental alloy.

Regarding the nucleation of the iron-rich intermetallics in 206 type cast alloys, It is found that β-Fe ($Al_7Cu_2(FeMn)$ is possible to nucleate on oxide film, $Al_6(FeMn)$ and α-Fe in 206 cast alloy at 0.3% Fe while $Al_6(FeMn)$ probably nucleates on oxide film [13]. In the present work, β-Fe is frequently observed to form around the early precipitated $Al_3(FeMn)$, as shown Fig. 6.12. It can be found that $Al_3(FeMn)$ is located in the centre and β-Fe is present at the both sides of the $Al_3(FeMn)$. The EBSD results have confirmed their presence of $Al_3(FeMn)$ (with a MAD value of 0.132) and β-Fe (with a MAD value of 0.144), as shown in Fig. 6.12b and 6.12c, indicating the possibility of β-Fe nucleating on $Al_3(FeMn)$. In addition, $Al_6(FeMn)$ is observed to form from the tip of $Al_3(FeMn)$, as shown in Fig. 6.10a. It was reported that the formation temperature of $Al_3(FeMn)$ is higher than $Al_6(FeMn)$ [1-3]. Therefore, it is reasonable to believe that the later formed $Al_6(FeMn)$ nucleates on the earlier formed $Al_3(FeMn)$.
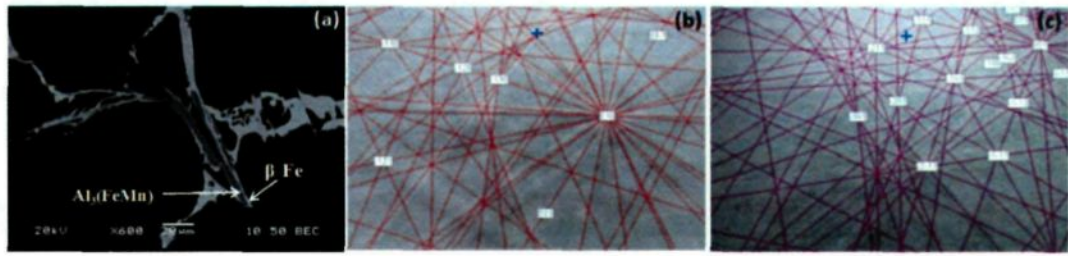
Fig. 6.12 Possible nucleation of β-Fe on $Al_3(FeMn)$ (a) and EBSD simulation results for $Al_3(FeMn)$ (MAD=0.132) (b) and β-Fe (MAD=0.144) (c)

In order to evaluate the possibility of the these nucleation mechanisms, the planar disregistry δ [13] has been calculated between β-Fe, $Al_6(FeMn)$ and $Al_3(FeMn)$ at low index plane families, as shown in Table 6.6. It was reported that the planar disregistry δ is the only index which can be easily used to quantitatively assess the nucleation potential and any disregistry less than 23 pct would assist the nucleation to some extent [46]. It is calculated that the planar disregistry δ is 13.15% between β-Fe and $Al_3(FeMn)$, and 11.34% between $Al_6(FeMn)$ and $Al_3(FeMn)$, indicating a positive potential for β-Fe and $Al_6(FeMn)$ to nucleate on $Al_3(FeMn)$.

Table 6.6 Planar disregistries between β-Fe, $Al_6(FeMn)$ and $Al_3(FeMn)$

Nucleating solid	Crystal structure	Match planes	δ(%)
β-Fe	Tetragonal	$(001)_{Al3(FeMn)} // (100)_{\beta\text{-Fe}}$	13.15
$Al_6(FeMn)$	Orthorhombic	$(010)_{Al3(FeMn)} // (001)_{Al6(FeMn)}$	11.34

6.4   Phase selection of iron-rich intermetallics in 206 cast alloys at 0.5%Fe

6.4.1   Iron-rich intermetallic phases precipitated at 12 K/min (KPM)

Fig. 6.13 shows the microstructures of the experimental 206 cast alloys solidified at 12 KPM. Two iron-rich intermetallic phases, i.e. Chinese script Al_mFe (or $Al_m(FeMn)$ in the presence of Mn) and platelet β-Fe are observed in Alloy 1 with 0.07% Si and 0.003% Mn and Alloy 2 with 0.09% Si and 0.11% Mn. In Alloy 3 with 0.19% Si and 0.22% Mn, α-Fe, $Al_m(FeMn)$ and β-Fe all coexist. However, only Chinese script α-Fe is present in Alloys 4, 5 and 6 while two platelet iron-rich intermetallics, $Al_3(FeMn)$ and β-Fe are observed in Alloy 7 with 0.09% Si and 0.53% Mn. These results clearly indicate that the content of Mn and Si have a significant influence on the formation of iron-rich intermetallic phases in the experimental 206 cast alloys at 0.5% Fe.
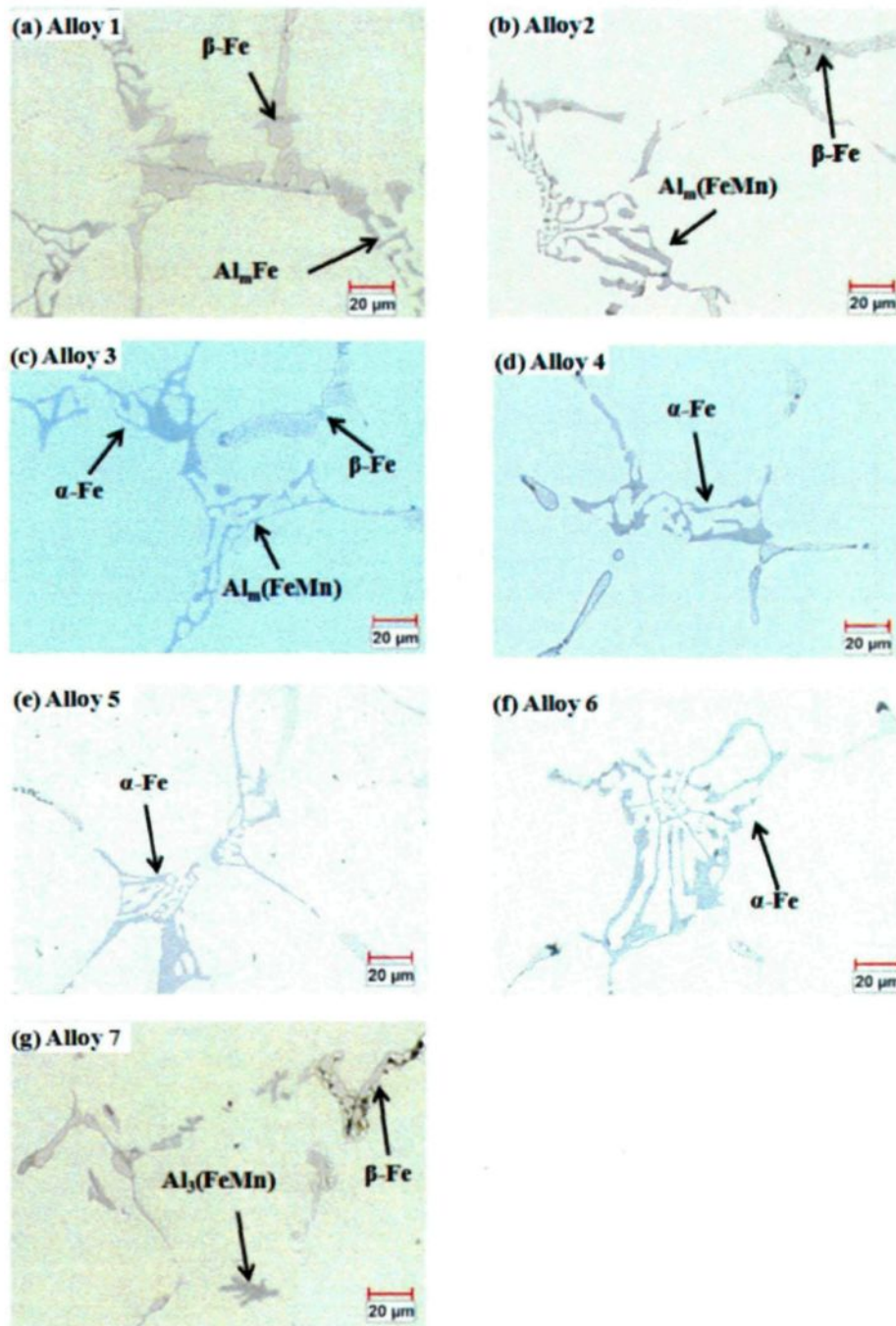
Fig. 6.13 Typical microstructures obtained in Alloys 1-7 solidified at 12 KPM

In order to clearly identify the iron-rich intermetallic phases, the combined use of both EDS and EBSD on SEM was performed, which can improve the phase identification process by collecting chemical information from EDS and crystallography information from EBSD simultaneously [27]. The SEM-EDS results are shown in Table 6.7.

Table 6.7 Composition of the iron-rich intermetallic phases obtained using SEM-EDS

Phases	Source	Elements (at. %)				
		Al	Si	Mn	Fe	Cu
Al_mFe	Alloy 1	78.93±0.87	0	0	16.41±0.65	4.91±0.22
$Al_3(FeMn)$	Alloy 7	75.62±0.89	0	3.2±0.22	17.5±0.36	3.68±0.12
α-Fe	Alloy 6	72.97±0.76	7.2±0.31	3.41±0.12	12.18±0.27	4.26±0.16
β-Fe	Alloy 1	72.74±0.72	0	1.98±0.16	6.31±0.21	18.96±0.28

As shown in Table 6.7, Si is only present in α-Fe and the ratio of Al: Cu: Fe is close to 7:2:1 in β-Fe. The α-Fe and β-Fe are two most popular intermetallic phases in Al-Cu cast alloys and can be easily identified. However, there are only small differences in chemical compositions between Al_mFe and $Al_3(FeMn)$. To further distinguish the iron-rich intermetallic phases, EBSD is used and the results are shown in Fig. 6.14. Figs. 6.14a and 14c display typical SEM microimages of Chinese script $Al_m(FeMn)$ and platelet $Al_3(FeMn)$ phases taken from Alloys 2 and 7, respectively. Their corresponding simulated patterns are shown in Figs. 6.14b and 14d, respectively.

159
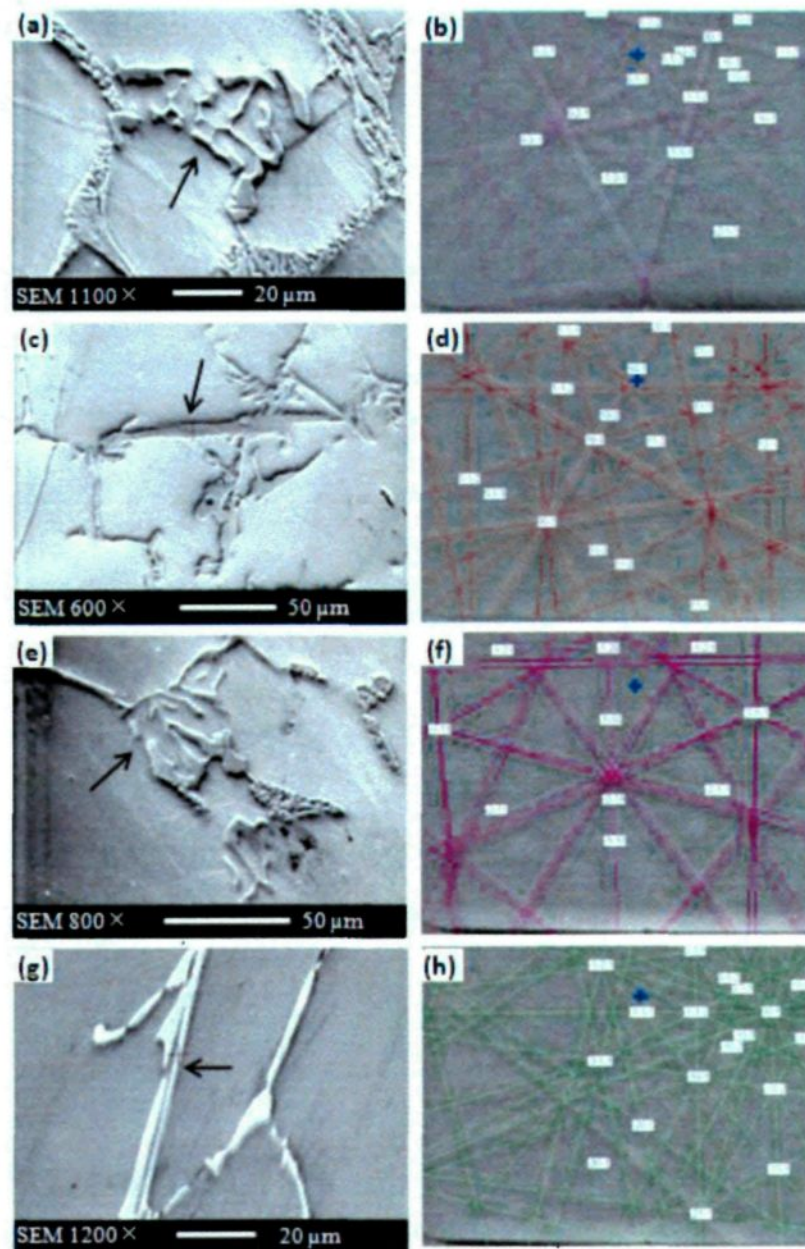
Fig. 6.14 Intermetallic morphologies, EBSD patterns and simulated results;
(a-b) for $Al_m(FeMn)$ taken from Alloy 2 (MAD=0.238);
(c-d) for $Al_3(FeMn)$ taken from Alloy 7 (MAD=0.215);
(e-f) for α-Fe taken from Alloy 6 (MAD=0.223);
(g-h) for β-Fe taken from Alloy 1 (MAD=0.301)

In EBSD, the Mean Angular Deviation (MAD) between the experimental and calculated patterns represents the accuracy of the solution given by the software (Channel 5). A smaller value indicates a closer match between the experimental and simulated patterns. Normally, a MAD value lower than 0.7 is considered to be desirable for an accurate solution [15]. As shown in Figs. 6.14b and 14d, the MAD values for Chinese script $Al_m(FeMn)$ and platelet $Al_3(FeMn)$ phases are 0.238 and 0.215, respectively, much lower than 0.7, confirming the presence of $Al_m(FeMn)$ and $Al_3(FeMn)$ in Alloys 2 and 7, respectively. The EBSD results of the α-Fe from Alloy 6 and the β-Fe from Alloy 1 are also shown in Figs. 6.14e-6.14h. The low MADs (0.223 for α-Fe and 0.301 for β-Fe) also verify the precipitation of α-Fe and β-Fe phases in Alloys 6 and 1, respectively.

Since Chinese script $Al_mFe/Al_m(FeMn)$ and platelet $Al_3(FeMn)$ have been reported only recently in 206 cast alloys [37, 47], the TEM observations have also been performed to further confirm their presence. Fig. 6.15 show the microimages of Al_mFe taken from Alloy 1 and $Al_3(FeMn)$ taken from Alloy 7, and their selected area diffraction pattern (SADP).

As shown in Fig. 6.15a and b, some streaks and extra reflection spots are often observed due to the defects such as twining and stacking fault in Al_mFe [5, 17]. The well indexed SADP further confirms the presence of the Al_mFe phase in Alloys 1-3. In addition,

Fig. 6.15c displays a TEM microimage of the half transverse section of a rod-like

$Al_3(FeMn)$ taken from Alloy 7.
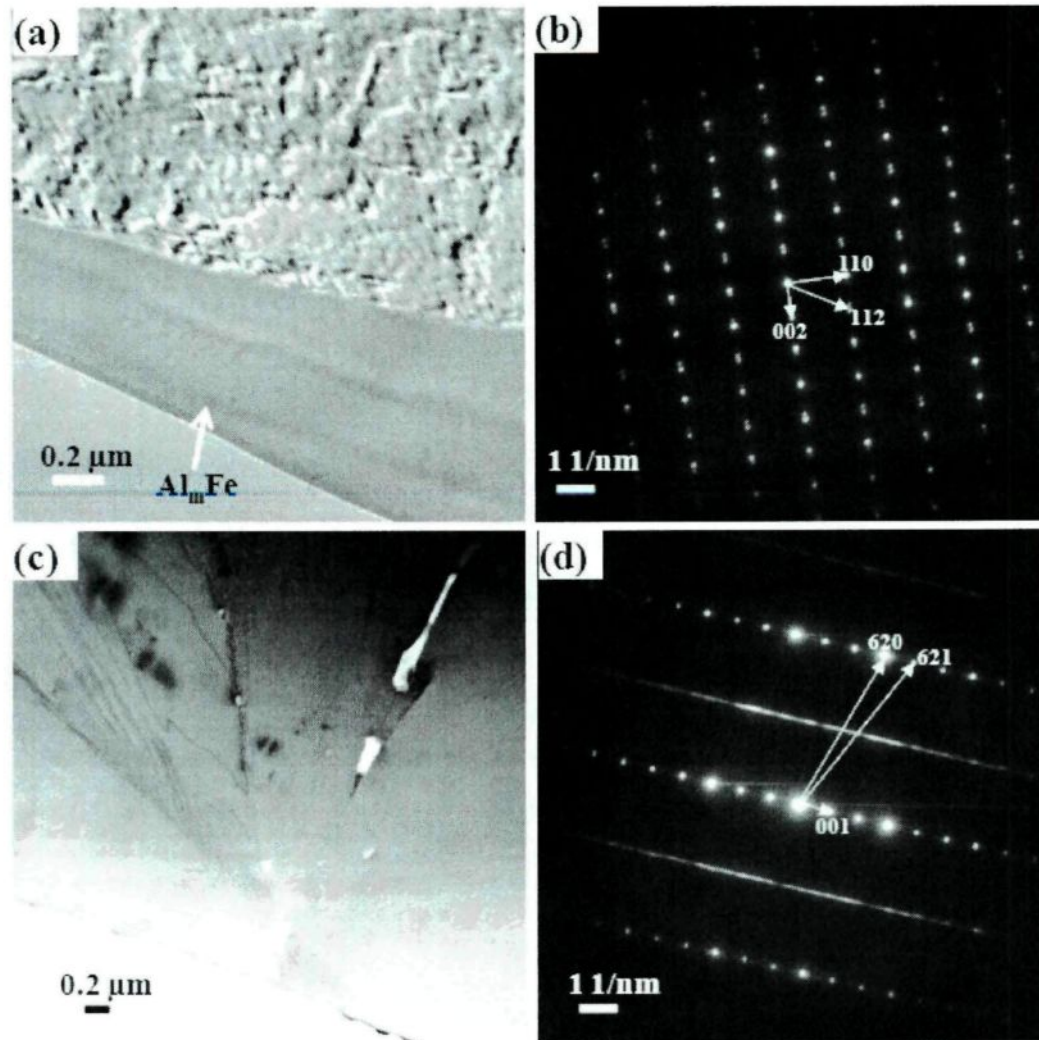
Fig. 6.15 TEM observations for Al_mFe taken from Alloy 1 and $Al_3(FeMn)$ from Alloy 7;
(a) TEM microimage of Al_mFe and (b) its SADP along [010];
(c) TEM microimage of $Al_3(FeMn)$ and (d) its SADP along $[\bar{1}30]$

The highly magnified transverse section of the $Al_3(FeMn)$ particle consists of several

faceted segments and some twinnings as observed in each segment. The similar segment

shape and twinings were also reported in Al-8.3% Fe alloys [28, 29]. The strong streak lines in Fig. 6.15d are parallel with [001] direction. The reflection spots have smeared into a coarse line on some planes, indicating the pronounced stacking faults in Al_3(FeMn) phase [4, 31, 48]. The well indexed SADP in Fig. 6.3d further confirms the presence of Al_3(FeMn) in Alloy 7 with 0.09% Si and 0.53% Mn.

In Alloy 3 with 0.19% Si and 0.22% Mn, both α-Fe and Al_m(FeMn) are observed to be adjacent, as shown in Fig. 6.13c. Though the morphologies of both the α-Fe and Al_m(FeMn) are Chinese script, they have some differences in chemical composition, particularly the high Si content which is present in α-Fe but absent from Al_m(FeMn), as shown in Table 6.7. Fig. 6.16 displays the SEM mapping for the two adjacent Chinese script iron-rich intermetallic phases taken from Alloy 2. It can be seen that both Cu and Fe are almost uniformly distributed in the two phases. However, Si is observed in the left phase but is almost absent in the right one, indicating that the left phase is α-Fe and the right one is Al_m(FeMn). In addition, it seems that the content of Mn is higher in α-Fe than in Al_m(FeMn).
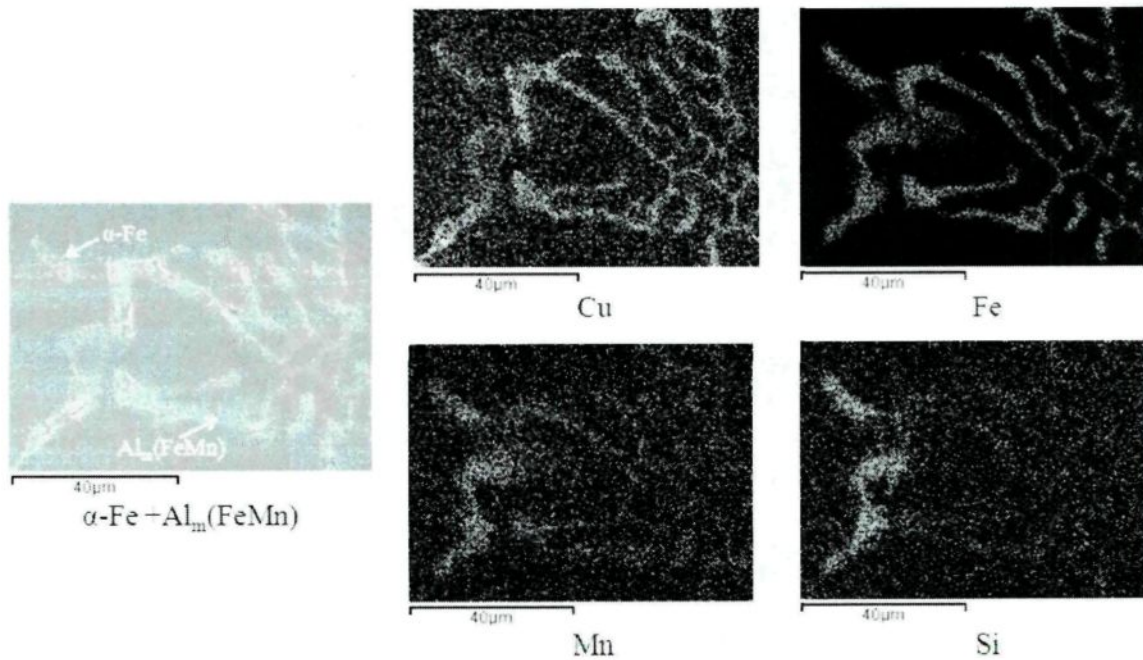
Fig. 6.16 SEM mapping for α-Fe and Al$_m$(FeMn)

Table 6.8 summarizes the information for the four iron-rich intermetallic phases including their crystal structures, densities and hardness values available. It can be found that both Al$_m$(FeMn) and α-Fe have similar crystal structure. However, it was reported that the formation temperature of Al$_m$(FeMn) is higher than that of α-Fe [13, 37]. Therefore, the α-Fe could probably nucleate on the Al$_m$(FeMn). In order to evaluate the possibility of this nucleation mechanism, the planar disregistry δ [13] between the α-Fe and the Al$_m$(FeMn) at the low index plane families has been calculated. It was reported that the planar disregistry δ is an index which can be easily used to quantitatively assess the nucleation potential [49]. The nucleating agent is thought to be potent if the disregistry is less than 12% assuming

that the electronic bonding contribution to the energy of the interface is favorable [50].

Campbell [46] extended the definition for substantially metallically bonded materials and

found that any disregistry lower than 23% would assist the nucleation to some extent. The

planar disregistry δ between $Al_m(FeMn)$ and α-Fe was calculated to be only 10.08%

between $(\bar{1}10)_{Alm(FeMn)}$ and $(001)_{\alpha\text{-Fe}}$, indicating the positive potential for α-Fe to nucleate on

$Al_m(FeMn)$.

Table 6.8 Properties for the iron-rich intermetallics in the experimental alloys [9]

Phase	Crystal structure	ρ (g/cm^3)	Mircohardness at 20 °C (GPa)
Al$_3$Fe	monoclinic a = 1.549 nm, b = 0.808 nm, c = 1.248 nm β = 107.72°	3.78	11.47
Al$_m$Fe	body-centered tetragonal a = b = 0.884 nm, c = 2.16 nm		
Al$_6$Fe	orthorhombic a = 0.643 nm, b = 0.746 nm, c = 0.878 nm	3.45	
β-Fe	tetragonal a = b = 0.634 nm, c = 1.488 nm	4.3	5.95
α-Fe	body-centered cubic a = b = c = 1.265 nm	3.55	8.8

To quantify the iron-rich intermetallic phases precipitated in all the experimental

alloys, the volume percent of the iron-rich intermetallic phases has been measured by using

an image analysis system and the results are shown in Fig. 6.17. These results indicate that

the formation of the iron-rich intermetallic phases is significantly related to the content of

Si and Mn. Compared with the formation of the iron-rich intermetallic phases shown in Figs. 6.13 and 6.17, it can be seen that Al_m(FeMn) preferably precipitates at low Si and Mn levels, as shown in Alloys 1 and 2 (Figs. 6.13a and 6.13b). With increasing Si content, α-Fe will favorably form instead of Al_m(FeMn) as in the cases of Alloys 4 to 6. On the other hand, the individual addition of Si favors the formation of α-Fe but inhibits the precipitation of β-Fe, as found in Alloys 3 and 5 (Fig. 6.13c and Fig. 6.13e). Similar results were also reported in 206 cast alloys at 0.15% Fe [51] and 0.3% Fe [13]. However, the individual addition of high Mn level (0.53%), as shown in Alloy 7 (Fig. 6.13g), promotes the formation of Al_3(FeMn). The combined addition of both Si and Mn enhances the precipitation of α-Fe rather than Al_3(FeMn) as observed in Alloys 4-6 (Figs. 6.13d-f). It is also evident that the type of iron-rich intermetallic phases depends on the alloy composition but the total volume percent of the iron-rich intermetallic phases tends to increase with increasing content of both Si and Mn. The Al_mFe/Al_m(FeMn) phase is observed to be the dominant iron-rich intermetallic at low Si and Mn levels, approximately 80 vol. % in Alloy 1 and 85 vol. % in Alloy 2. In Alloy 3 with 0.19% Si and 0.22% Mn, however, the Chinese script Al_m(FeMn) and α-Fe occupy about 90 vol. %. In Alloys 4, 5 and 6, the α-Fe is present as the only iron-rich intermetallic phase due to the significant enhancement by Si

[13, 20, 52]. In Alloy 7, the $Al_3(FeMn)$ occupies about 75 vol. % with the remaining 25

Vol. % β-Fe, probably due to the high Mn and low Si [47].
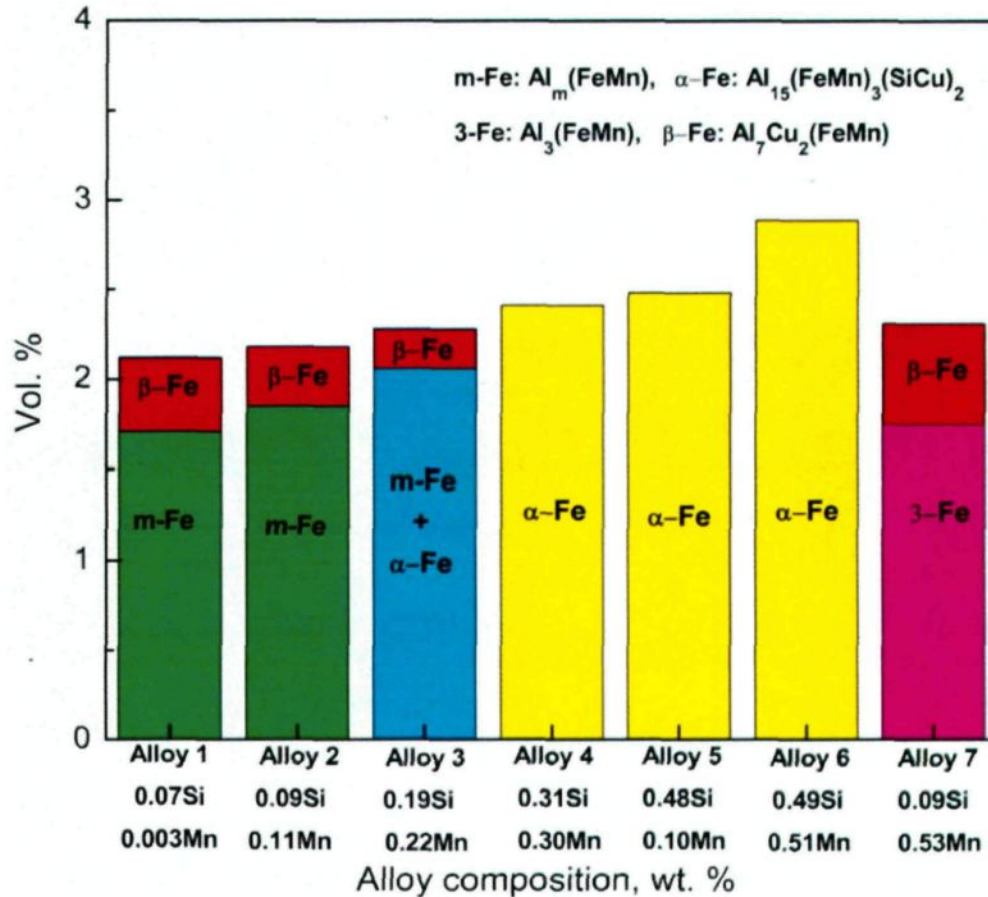
Fig. 6.17 Vol. % of the iron-rich intermetallic phases in the experimental alloys

6.4.2 Solidification reactions and sequences of experimental alloys

According to the iron-rich intermetallic phases shown in Figs. 6.13 and 6.17, the

seven experimental alloys used can been classified into four types: Alloys 1 and 2 with

dominant $Al_mFe/Al_m(FeMn)$, Alloy 3 with dominant $Al_m(FeMn)$ and α-Fe, Alloys 4-6 with

only α-Fe and Alloy 7 with dominant $Al_3(FeMn)$. The TA curves of the four typical alloys,

such as Alloys 1, 3, 5 and 7, are shown in Fig. 6.18.
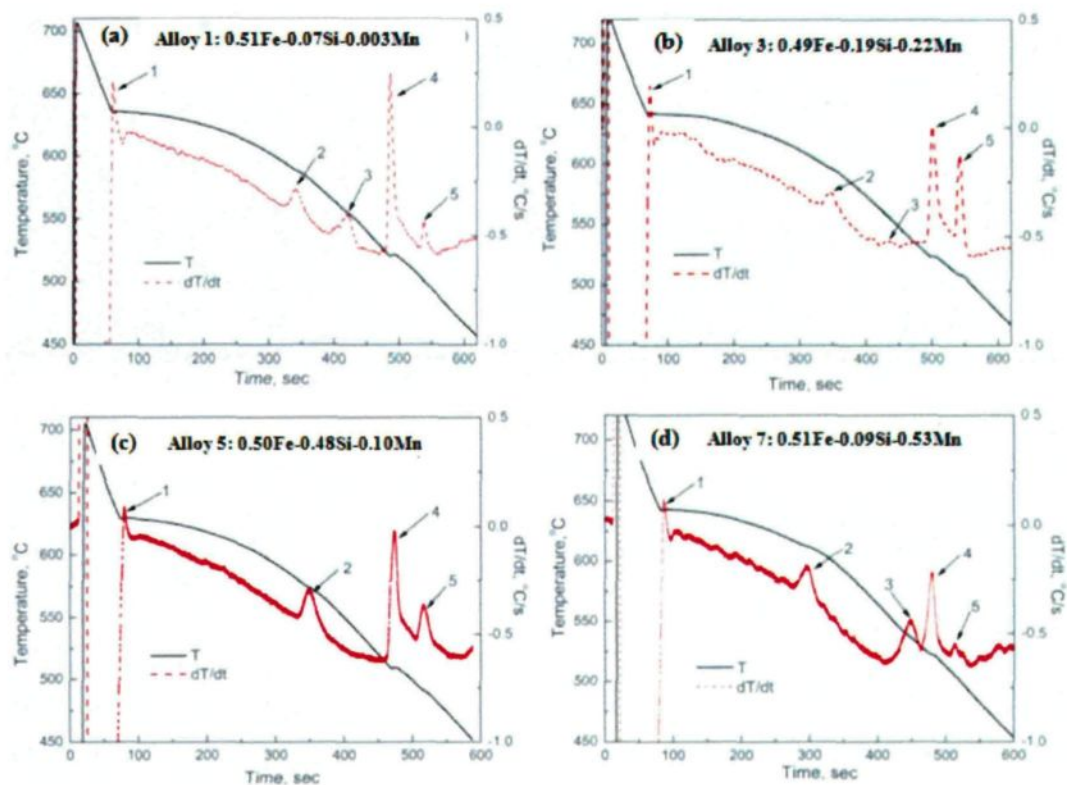
Fig. 6.18 TA curves and their first derivatives of Alloys 1, 3, 5 and 7

From the TA curves, it can be found that the number of the peaks (reactions) varies

with the contents of Si and Mn. As shown in Figs. 6.18a, b and d, five peaks are present in

Alloys 1, 3 and 7 but the intensity of peak 3 in Alloy 3 (Fig. 6.18b) is much weaker. This

peak even disappears in Alloy 5 and only four peaks are thus detected, as shown in Fig.

168

6.18c. According to literature [13, 37, 47], Peak 3 is related to the precipitation of platelet β-Fe, indicating that the β-Fe is present in Alloys 1, 3, and 7 but its volume percent is much lower in Alloy 3 while it is even completely suppressed in Alloy 5, which is in consistent agreement with the optical observations and the measured volume percent.

After the α-Al dendrite formed at Peak 1, Peak 2 is the main reactions where different iron-rich intermetallic phases can precipitate. To identify iron-rich intermetallic phases occurring at Peak 2, interrupted quenching at 590 °C (between Peak 2 and Peak 3) was performed for Alloys 1, 3, 5 and 7 and the microstructures obtained are shown in Fig. 6.19. It was found that some Chinese script iron-rich phases are present in Alloys 1, 3 and 5 but a platelet iron-rich phase occurred in Alloy 7. As identified by using EDS and EBSD, the Chinese script phase is Al_mFe in Alloy 1 (Fig. 6.19a), and α-Fe in Alloy 5 (Fig. 6.19c). However, both the $Al_m(FeMn)$ and α-Fe are detected in Alloy 3, as marked as $Al_m(FeMn)$/α-Fe in Fig. 6.19b. The platelet iron-rich intermetallic in Alloy 7 is identified to be $Al_3(FeMn)$, as shown in Fig. 6.19d. In addition, a small amount of $Al_6(FeMn)$ is reported to coexist with dominant $Al_3(FeMn)$ in Alloy 7 after water quenching at 615 °C [47].
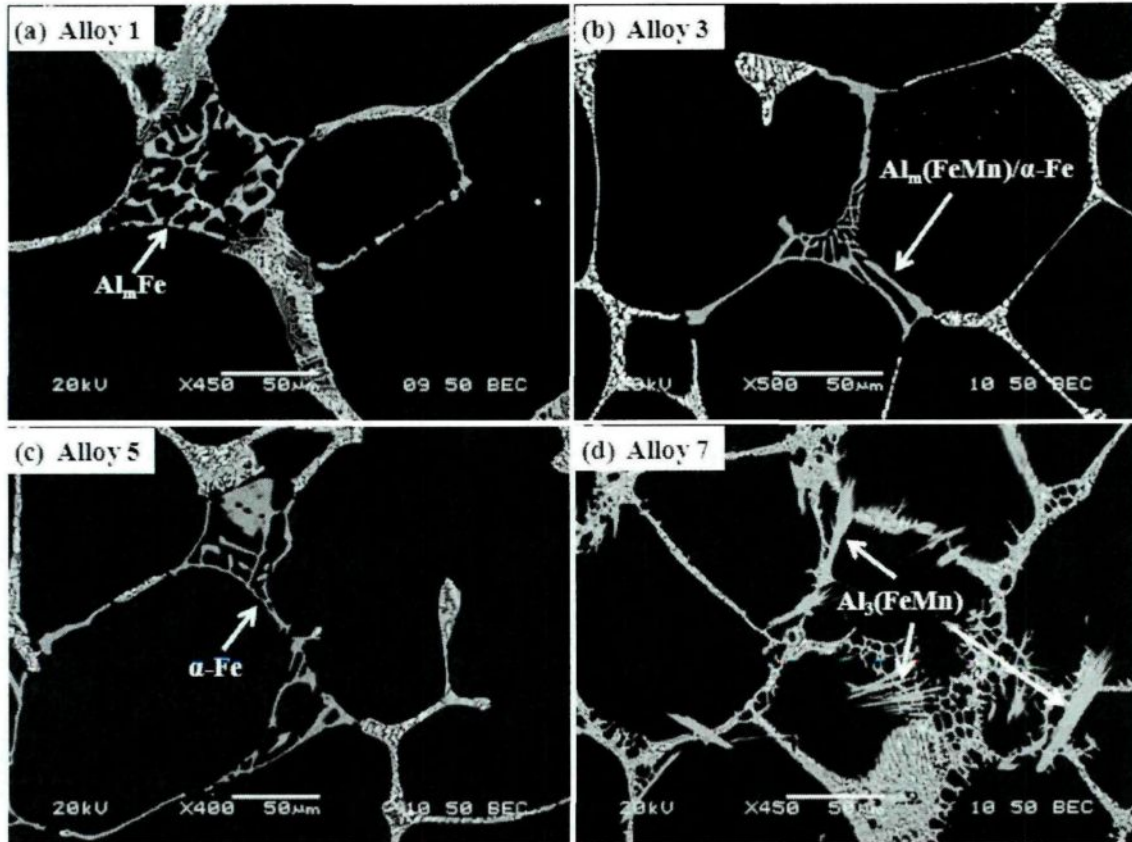
Fig. 6.19 Microstructures of Alloys 1, 3, 5 and 7 after interrupted quenching at 590 °C

To further identify the iron-rich intermetallic phases and determine their formation temperatures during solidification, DSC was also used and the results are shown in Fig. 6.20. It can be found that the results obtained are rather similar to those obtained from the TA curves. However, the 5 peaks are all detected in Alloys 1, 3, 5, and 7, probably due to the high accuracy of the DSC technique although the intensity of Peak 3 in Alloy 5 is rather weak. The formation temperature of β-Fe (Peak 3) in Alloy 5 is also the lowest due to the inhibiting effect of Si on β-Fe. As displayed in Fig. 6.20b (Peaks 2), the formation temperatures of the dominant iron-rich intermetallic phases are in a descending order of

Al$_3$(FeMn) at 615 °C in Alloy 7, Al$_m$Fe at 611 °C in Alloy 1 and α-Fe at 601 °C in Alloy 5,

similar to the results reported in literature [13, 37, 47].
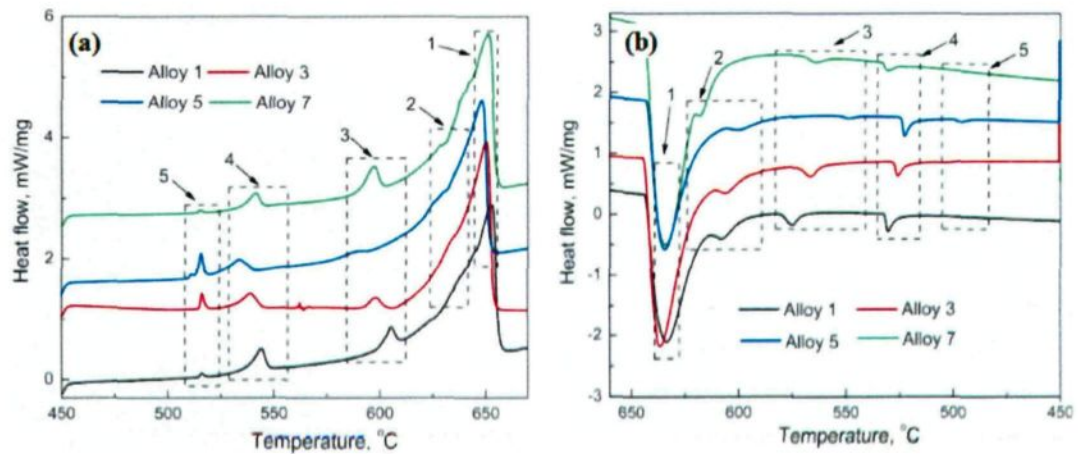
Fig. 6.20 DSC curves and their first derivates: (a) heating and (b) cooling curves

Based on the present and earlier systematic metallographic observations [13, 37, 47]

and results of the TA and DSC curves obtained in the present work, the solidification

reactions and sequences occurring in the experimental alloys are listed in Table 6.9.

Table 6.9 Solidification reactions and sequences in the 206 cast alloys at 0.5% Fe

Peak	Reaction	Temperature (°C)*	Alloy
1	Development of aluminum dendrite	648	1-7
2**	a) Liq. →Al + Al_mFe/$Al_m(FeMn)$	629	1, 2
	b) Liq. →Al + $Al_m(FeMn)$+α-Fe	627	3
	c) Liq. →Al + α-Fe	625-615	4-6
	d) Liq. →Al + $Al_3(FeMn)$/$Al_6(FeMn)$	640	7
3**	a) Liq. + $Al_3(FeMn)$/$Al_m(FeMn)$/α-Fe →Al + β-Fe b) Liq. →Al + β-Fe	595~575	1-7
4***	Liq. →Al + Al_2Cu + $Al_{20}Mn_3Cu_2$ + β-Fe	540~530	1-7
5***	Liq. →Al + Al_2Cu + Al_2CuMg + Mg_2Si	510~500	1-7

Notes: The peak numbers correspond to those as indicated in Figs. 6.18 and 6.20

*: Temperatures are determined from the DSC heating curves, where the undercooling effect is avoided.

**: The type of the iron-rich phases, $Al_3(FeMn)$, $Al_m(FeMn)$, α-Fe and β-Fe precipitated during solidification depends on the alloy compositions.

***: Based on the prior work of Backerud et al. [14].

6.4.3 Effect of cooling rate on phase selection of iron-rich intermetallics

As shown in Figs. 6.13 and 6.17, $Al_m(FeMn)$,α-Fe and $Al_3(FeMn)$ can be one of the dominant Fe-rich intermetallic phases in the final microstructure of the experimental alloys, indicating that the precipitation of the iron-rich intermetallic phases mainly depends on the alloy composition at a given cooling condition. However, the cooling rate also plays an important role in phase selection of the iron-rich intermetallics. To investigate the effect of

cooling rate on iron-rich intermetallic phases, the DSC experiments of different alloys were conducted with a controllable and accurate cooling rate at 1, 5, 10 and 50 KPM. Alloys 1, 3, 5 and 7 are still selected as four typical alloys. Fig. 6.21 shows their DSC cooling curves obtained at 1, 5, 10 and 50 KPM.
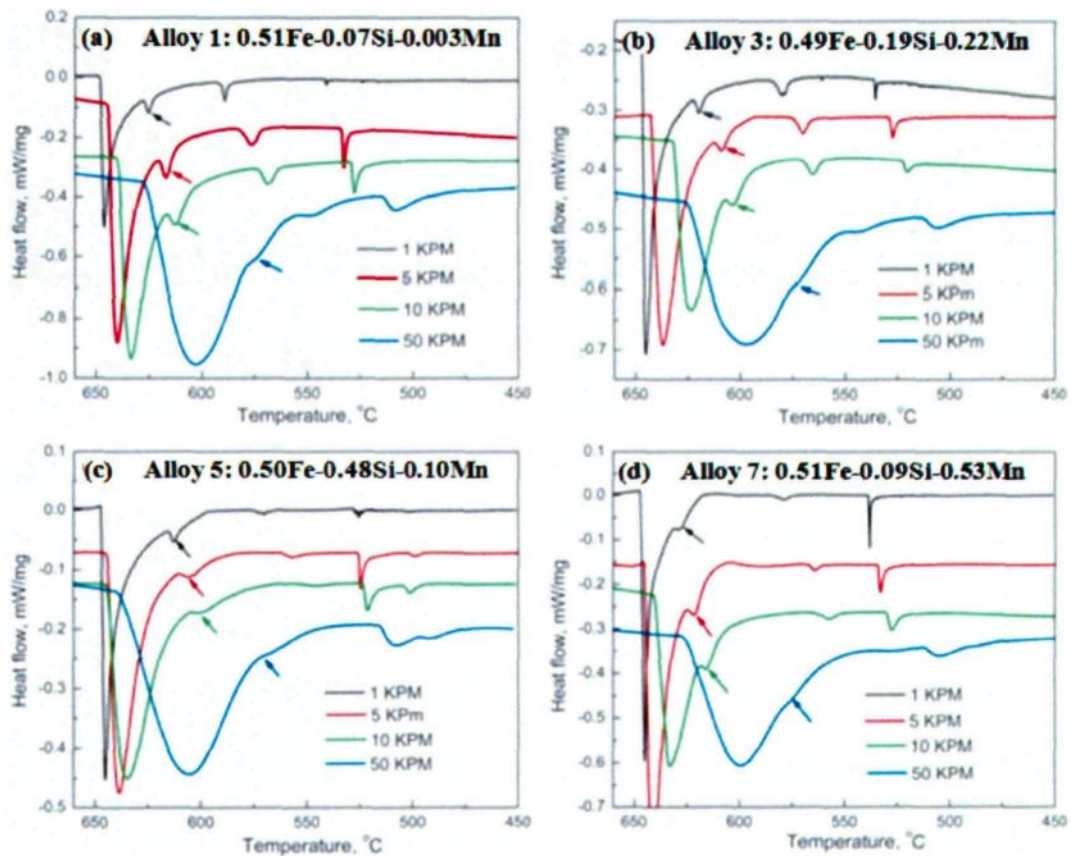
Fig. 6.21 DSC cooling curves of Alloys 1, 3, 5 and 7 at various cooling rates

It was found that the temperature of the second peaks (indicated by the arrows and corresponding to Reactions 2 in Table 6.9) decreases with increasing cooling rate for all

four alloys. The results are also shown in Table 6.10. At a given cooling rate, the formation temperature of the iron-rich intermetallics also varies with alloy compositions, i.e. Si and Mn content. For instance, the formation temperature of $Al_3(FeMn)$ is 625.1 °C for Alloy 1, 619.6 °C for Alloy 3 and 611.5 °C for Alloy 5, respectively, at a cooling rate of 1 KPM. The dominant iron-rich intermetallic phases of the solidified microstructure and their formation temperatures vary with the alloy composition and cooling rate, as shown in Table 6.10. The microstructures of Alloys 1, 5 and 7 at various cooling rates are shown in Fig. 6.12. Due to the similar morphologies of the iron-rich intermetallics in Alloys 1 and 3, the microstructure of Alloy 3 is not presented here. All iron-rich intermetallic phases in these alloys have been identified and confirmed by using EBSD and EDS.

It is interesting to note that the formation of platelet β-Fe can be effectively suppressed in all the experimental alloys at a high Fe level of 0.5% (Figs. 6.13, 6.17 and 6.21). The critical cooling rate to suppress β-Fe is much lower than that reported for 206 cast alloys at 0.15% Fe [51]. For instance, the critical cooling rate is 10 KPM for Alloy 5 at 0.5% Fe, lower than 90 KPM (1.5 K/s) for the 206 cast alloy at 0.15% Fe [51]. Therefore, it is much easier to suppress the formation of platelet β-Fe for the experimental 206 alloys at higher Fe contents.

Table 6.10 Formation temperatures of main iron-rich intermetallics
at various cooling rates

Cooling rate (KPM)	Alloy 1		Alloy 3		Alloy 5		Alloy 7	
	Main Phase	Temp. (°C)	Main Phase	Temp. (°C)	Main Phase	Temp. (°C)	Main Phase	Temp. (°C)
1	3	625.1	3	619.6	3	611.5	6	627.1
5	6	616.6	6	608.9	α+m	605.2	6+3	621.1
10	m	612.5	m+α	603.8	α	602.1	3	615.6
50	m	581.2	m+α	576.8	α	573.2	m	577.1

Note: 3 - $Al_3(FeMn)$, 6 - $Al_6(FeMn)$, m - $Al_m(FeMn)$ and α - $Al_{15}(FeMn)_3(SiCu)_2$

As shown in Fig. 6.22 and Table 6.10, the dominant iron-rich intermetallic phase at a very low cooling rate of 1 KPM (near equilibrium condition) for most of the Si and Mn range studied in present work is $Al_3Fe/Al_3(FeMn)$, which is generally considered as the equilibrium phase in Al-Fe and Al-Fe-Si systems [2]. The only exception is Alloy 7 where $Al_6(FeMn)$ appears at the very low cooling rate and is displaced by $Al_3(FeMn)$ with an increase of the cooling rate up to 10 KPM. It seems that $Al_6(FeMn)$ becomes more stable than $Al_3(FeMn)$ in the presence of high Mn and low Si. According to the Al-Fe-Mn phase diagram in Al-rich corner [53], the critical Mn content for the $Al-Al_3(FeMn)-Al_6(FeMn)$ eutectics is about 0.43%. When the Mn content is less than 0.43%, the formation of $Al_3(FeMn)$ is more favorable but $Al_6(FeMn)$ will be the preferable iron-rich intermetallic to precipitate at a Mn content higher than 0.43% [7]. In Alloy 7, the Mn content is as high as

0.53% and thus $Al_6(FeMn)$ tends to be a stable phase rather than $Al_3(FeMn)$ at a very low

cooling rate (1KPM).
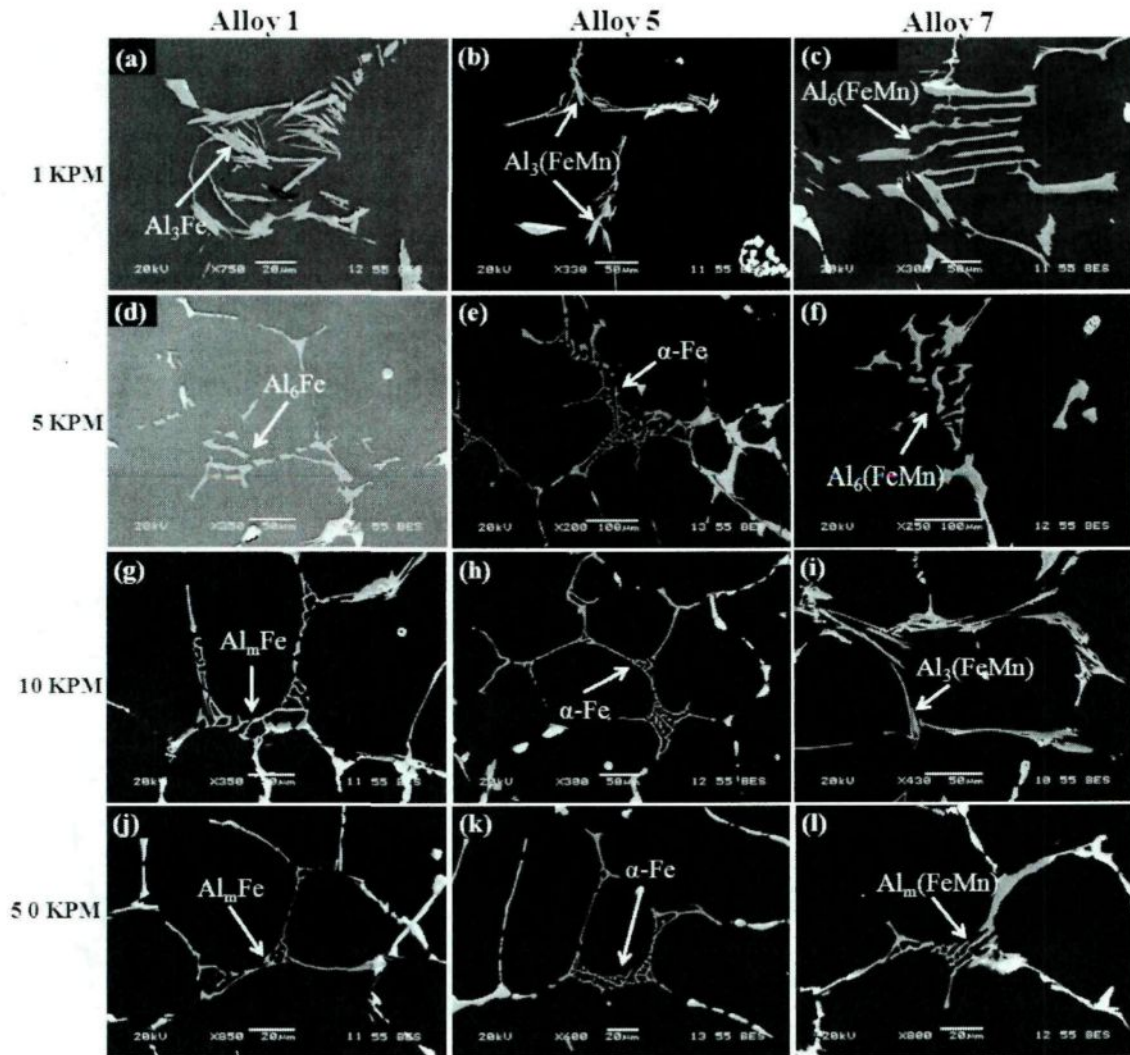
Fig. 6.22 Microstructures of Alloy 1, 5 and 7 at various cooling rates;
(a-c) 1 KPM, (d-f) 5 KPM, (g-i) 10 KPM, (j-l) 50 KPM

With increase cooling rate (towards more non-equilibrium condition), the dominant

iron-rich intermetallic phases change from Al_3Fe via Al_6Fe to Al_mFe for Alloy 1, $Al_3(FeMn)$

via $Al_6(FeMn)$ to $Al_m(FeMn)/\alpha$-Fe for Alloy 3 and from $Al_3(FeMn)$ via $Al_m(FeMn)$ to α-Fe

for Alloy 5, respectively. Besides, the major intermetallic phase in Alloy 7 also transforms from $Al_3(FeMn)$ to $Al_m(FeMn)$ when the cooling rate increases from 10 PKM to 50 KPM. All the experimental results indicate the significant effect of cooling rate on the phase selection of the iron-rich intermetallics during solidification. These results are in general agreement with prior work in Al-Fe and Al-Fe-Si systems [2, 12, 54], in which the equilibrium phase of Al_3Fe can be kinetically replaced by an intermediate metastable phase of Al_6Fe and further displaced by a more metastable phase of Al_mFe under more extreme solidification conditions. In addition, it can be found that the dominant iron-rich intermetallic is Al_mFe in Alloy 1, α-Fe in Alloy 5 and $Al_3(FeMn)$ in Alloy 7 at a cooling rate of 10 KPM, which is similar to that obtained from TA analysis samples solidified at 12 KPM, as shown in Figs. 6.13 and 6.17.

The effect of cooling rate and alloy composition on intermetallic phase selection can be explained by the competitive growth model based on the growth temperature theory [2, 10]. During solidification, one phase can be kinetically displaced by another one if the later has a higher growth temperature (T_G) than the former, assuming that both phases are able to nucleate and grow under given solidification conditions [2]. The relationship between growth temperature (T_G) of iron-rich intermetallic phases and growth velocity (V) can be expressed as [10]:

$$T_G = T_{EU} - kV^{1/2} \qquad\qquad (1)$$

Where T_{EU} is the equilibrium eutectic temperature of an iron-rich intermetallic phase

and k is a constant.

The cooling rate (V_C) is reported to be proportional to growth velocity (V) [55], and

thus Equation (1) can be displaced by the following equation:

$$T_G = T_{EU} - k'V_C^{1/2} \qquad\qquad (2)$$

It can be found that growth temperature (T_G) decreases with growth velocity (V) or

cooling rate (V_C). However, the constant k or k' varies with the iron-rich intermetallic

phases and alloy chemistry. In other words, the extent of its reduction of the growth

temperature of the iron-rich intermetallics also varies with the intermetallic phases and the

alloy chemistry. The iron-rich intermetallic phase with a higher growth temperature is

usually preferred to precipitate during solidification and may be replaced by another

intermetallic with a higher growth temperature with increasing cooling rate.

According to the experimental results shown in Table 6.10 and Fig. 6.22, the

relationship between growth temperature (T_G) and cooling rate (V_C) for the four typical

alloys is displayed in Fig. 6.23.

As shown in Fig. 6.23, the iron-rich intermetallics evolve from the stable to

metastable phases with increasing cooling rate (V_C). The growth temperatures (T_G) of each

iron-rich intermetallic phase decreases with increasing cooling rate (V_C). However, the descending rates of the growth temperatures with cooling rate (i.e. k' values in Equation 2) depend on alloy chemistry (i.e. Si and Mn content in the present study). As shown in Fig. 6.23a, it can be found that the descending rates of Al_3Fe, Al_6Fe and Al_mFe increase with increasing Si content, which is in general consistency with the results of Al_3Fe and Al_mFe phases as reported by Meredith et al. [56]. In addition, the range of cooling rate for a given iron-rich intermetallic phase to occur also varies with the alloy chemistry. As shown in Fig. 6.23a, the cooling rate range becomes a little wider for Al_3Fe but much narrower for Al_6Fe with increasing Si content. It was reported that the Si content can broaden the cooling rate range of Al_3Fe but shrink that of Al_6Fe [57, 58]. In Alloy 5, the high content of Si can enhance the formation of α-Fe and thus the α-Fe becomes the main iron-rich intermetallic phase at a cooling rate above 5 KPM.

It is most interesting to point out that there exists a threshold cooling rate above which all Fe-rich intermetallics can be mainly present in Chinese script morphologies (Al_mFe or α-Fe). This critical cooling rate decreases with increasing Si content as indicated in Fig. 6.23a. The values of the threshold cooling rate are quite low. For instance, the critical cooling rate is approximately 8 KPM in Alloy 1 (indicated by "A" in Fig. 6.23a) and 6 KPM in Alloy 3 for the formation of Al_mFe but only 3.5 KPM for the formation of

α-Fe in Alloy 5. In Alloy 7, the critical cooling rate for Al_mFe is higher, approximately 43

KPM (indicated by "B" in Fig. 6.23b). These values are still much lower than those cooling

rates reported for the formation of Al_mFe or α-Fe phases in AA1XXX series alloys (Al-Fe

and Al-Fe-Si systems), i.e. 10 ~ 20 K/s (600 ~ 1200 KPM) for Al_mFe in Al - 0.2% ~ 0.6%

Fe alloy and 5.5 K/s (330 KPM) for α-Fe in cast Al-0.29% Fe-0.17% Si alloy [2]. The low

critical cooling rate obtained in the present work indicates the high possibility of casting

new 206 Al-Cu alloys using conventional casting processes to obtain Chinese script phases

(Al_mFe or α-Fe) with a high tolerant iron content.
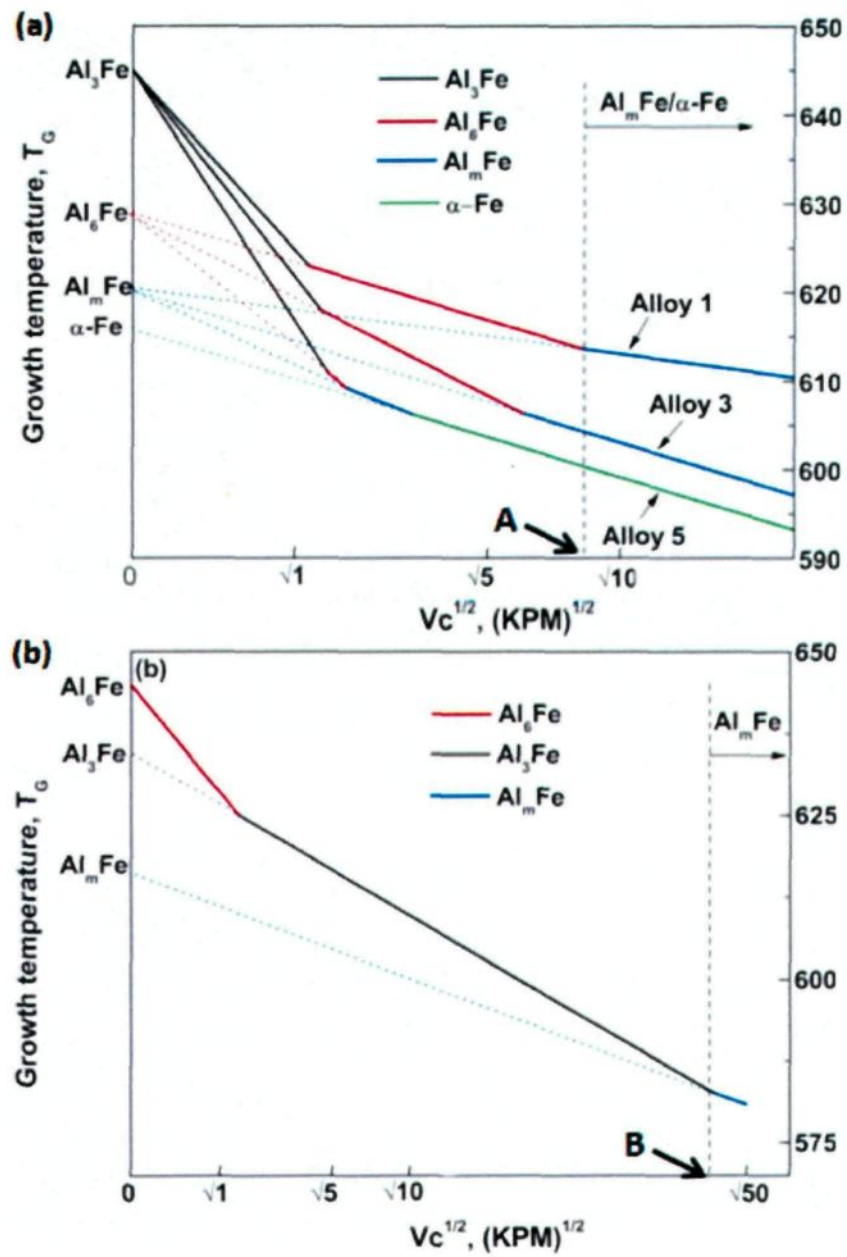
Fig. 6.23 Relationship between growth temperature (T_G) and cooling rate (V_C) for (a) Alloy 1 (0.07Si-0.003Mn); Alloy 3 (0.48Si-0.10Mn) and Alloy 5 (0.11Si-0.53Mn); and (b) Alloy 7(0.11Si-0.53Mn)

In summary, the dominant Chinese script $Al_m(FeMn)$ or α-Fe phases can be obtained in the solidified microstructure above cooling rates of 8 KPM for Alloys 1-6 and 43 KPM for Alloy 7. These cooling rates are much lower than those used in industrial permanent mold casting condition (2-3 K/s, i.e. 120-180 KPM). Therefore, Chinese script $Al_m(FeMn)$ or α-Fe can be predominant for all experimental alloys solidified in normal industrial permanent mold casting. Due to the fact that Chinese script morphologies can minimize their harmful effect on mechanical properties, the design and development of new 206 cast alloys at higher iron contents may become feasible under well controlled solidification conditions. It was also reported that the dominant Chinese script iron-rich intermetallics are beneficial to increase fatigue life of the Al-Cu cast alloys, one of the important properties for automobile and aerospace applications [59]. Future work will need to systematically investigate the effects of the various iron-rich intermetallics on the mechanical properties and further optimize the phase structures and the associated mechanical properties.

6.5 Summary

(1) The solidification microstructure and the precipitation of various iron-rich intermetallic phases in Al-Cu 206 cast alloys at a high iron level of 0.5% were

systematically investigated, and the full solidification reactions and sequences as well as the formation temperatures of iron-rich intermetallics were established.

(2) Iron-rich Al_mFe phase is observed, for the first time, in A206 Al-Cu cast alloys at a high Fe level of 0.5%. Its formation temperature is about 902 K (629 °C), measured from DSC heating process. This phase can precipitate at a low cooling rate of 0.2 K/s, compared to its formation at high cooling rates (>10 K/s) for AA1xxx and AA5xxx alloys. It has 2-D Chinese script and 3-D compact branched morphology. The structure of the Al_mFe phase has been confirmed by TEM and EBSD as body centered tetragonal. The value of m is about 4.2. Al_mFe phase can form and be present in the fully solidified experimental A206 cast alloy as the dominant iron-rich intermetallic phase (~81 vol. %). The formation of the dominant Chinese script Al_mFe in A206 cast alloy with high Fe (0.5%) and low levels of Mn (0.003%) and Si (0.1%) indicates the significant potential of designing and developing new A206 family cast alloys with expected enhanced mechanical properties in spite of high iron contents.

(3) $Al_3(FeMn)$ phase is experimentally observed to be present in the fully solidified Al-4.6Cu-0.5Fe-0.5Mn-0.1Si 206 cast alloy and becomes the dominant iron-rich intermetallic phase (75 vol. %) with the remaining 25 vol. % for β-Fe. Al_3 (FeMn) is formed through a eutectic reaction and has a platelet-like morphology. The formation

temperature of $Al_3(FeMn)$ is about 640 °C as obtained from the DSC heating process. The formation of dominant $Al_3(FeMn)$ phase is probable due to the favored phase selection and the segregation of Fe in liquid aluminum during solidification.

(4) $Al_m(FeMn)$, α-Fe and $Al_3(FeMn)$ are all possible as dominant iron-rich intermetallic phases of the solidified microstructure in 206 cast alloy at 0.5% Fe, depending on Si and Mn content at a cooling rate of 12 KPM. $Al_m(FeMn)$ preferably precipitates at low Si and Mn levels. The individual addition of Si favors the formation of α-Fe but inhibits the precipitation of β-Fe while the individual addition of a high Mn level promotes the formation of $Al_3(FeMn)$. The combined addition of both Si and Mn enhances the formation of predominate α-Fe.

(5) Over most of the Si and Mn levels investigated in the present work, $Al_3(FeMn)$ is considered to be stable but $Al_6(FeMn)$ and $Al_m(FeMn)$ are metastable iron-rich intermetallics. At high Mn and low Si, however, $Al_6(FeMn)$ becomes stable, and $Al_3(FeMn)$ and $Al_m(FeMn)$ are metastable phases. With increasing cooling rate, the formation temperature of each iron-rich intermetallic phase decreases and the stable iron-rich intermetallic is gradually replaced by the metastable phase.

(6) There exists a threshold cooling rate to obtain the predominant Chinese script Al_mFe or α-Fe phases. This critical cooling value is much lower in experimental 206 cast

alloys than in Al-Fe and Al-Fe-Si (AA1XXX) alloys. The achievement of dominant Chinese script iron-rich intermetallics $Al_m(FeMn)$ or α-Fe in all experimental alloys at 0.5% Fe in normal industrial permanent mold casting indicates the great possibility of designing and developing new 206 cast alloys with a high iron content.

References

[1] C. A. Aliravci and M. O. Pekguleryuz: *Calphad*, 1998, Vol. 22, pp. 147-155.

[2] C. M. Allen, K. A. Q. O'Reilly, B. Cantor and P. V. Evans: *Prog. Mater. Sci.*, 1998, Vol. 43, pp. 89-170.

[3] X. G. Chen: *Light Metals*, Minerals, Metals & Materials Soc (TMS), San Antonio, TX, USA, 1998, pp. 1071-1076.

[4] Y. J. Li and L. Arnberg: *Acta Mater.*, 2004, Vol. 52, pp. 2673-2681.

[5] P. Skierpe: *Acta Cryst.*, 1988, Vol. B44, pp. 480-486.

[6] L. F. Mondolfo, *Aluminum alloys: Structure and properties*, Butterworths, London, 1976.

[7] M. W. Meredith, A. L. Greer, P. V. Evans and R. G. Hamerton: *Light metals*, San Diego, CA, USA, 1999, pp. 811-817.

[8] C. M. Adam and L. M. Hogan: *Acta Metall.*, 1975, Vol. 23, pp. 345-354.

[9] L. Bäckerud: *Jernkont. Ann.*, 1968, Vol. 152, pp. 109-138.

[10] L. Dong and J. Howard: *Z. Metallkde*, 1992, Vol. 83, pp. 224-226.

[11] I. R. Hughes and H. Jones: *J. Mater. Sci.*, 1976, Vol. 11, pp. 1781-1793.

[12] N. A. Belov, A. A. Aksenov and D. G. Eskin, *Iron in aluminum alloys: impurity and alloying element*, Taylor & Francis, London, 2002.

[13] K. Liu, X. Cao and X. G. Chen: *Metall. Mater. Trans. A*, 2011, Vol. 42, pp. 2004-2016.

[14] L. Bäckerud, *Solidification characteristics of aluminum alloys*, Skanaluminium, Universitetsforlaget AS, Oslo, Norway, 1986.

[15] M. Kral: *Scripta Mater.*, 2004, Vol. 51, pp. 215-219.

[16] P. Skjerpe: *Mater. Trans. A*, 1987, Vol. 18A, pp. 189-200.

[17] R. M. K. Young and T. W. Clyne: *Scrital Metall. Mater.*, 1982, Vol. 15, pp. 1211-1216.

[18] X. Cao and J. Campbell: *Metall. Mater. Trans. A*, 2003, Vol. 34, pp. 1409-1420.

[19] M. V. Kral, P. N. H. Nakashima and D. R. G. Mitchell: *Metall. Mater. Trans. A*, 2006, Vol. 37, pp. 1987-1997.

[20] K. Liu, X. Cao and X. G. Chen: *Light Metal – Advances in Materials and Processes*, Met. Soc, Vancouver, BC, Canada, 2010, pp. 113-120.

[21] J. Cho, X.Yan and C. R. Loper: *AFS Trans.*, 2003, Vol. 111, pp. 1-17.

[22] F. C. R. Hernandez, M. B. Djurdjevic, W. T. Kierkus and J. H. Sokolowski: *Mater. Sci. Eng., A*, 2005, Vol. 396, pp. 271-276.

[23] S. G. Shabestari: *Mater. Sci. Eng., A*, 2004, Vol. 383, pp. 289-298.

[24] A. Couture: *Int. Cast Met. J.*, 1981, Vol. 6, pp. 9-17.

[25] C. J. Tseng, S. L. Lee, T. F. Wu and J. C. Lin: *Mater. Trans., JIM*, 2000, Vol. 41, pp. 708-713.

[26] C. J. Tseng, S. L. Lee, S. C. Tsai and C. J. Cheng: *J. Mater. Res.* , 2002, Vol. 17, pp. 2243-2250.

[27] C. L. Chen and R. C. Thomson: *J. Alloys Compd.*, 2010, Vol. 490, pp. 293-300.

[28] D. H. Kim and B. Cantor: *J. Mater. Sci.*, 1994, Vol. 29, pp. 2884-2892.

[29] K. Sahoo, S. Das and B. Murty: *Mater. Sci. Eng., A*, 2003, Vol. 355, pp. 193-200.

[30] Z. F. Li, R. Y. Zhang and D. Mei: *Journal of Inner Mongolia University of Technology*, 2004, Vol. 23, pp. 209-212.

[31] P. Skjerpe: *J. Microsc.*, 1987, Vol. 148, pp. 33-50.

[32] Á. Griger and V. Stefániay: *J. Mater. Sci.*, 1996, Vol. 31, pp. 6645-6652.

[33] Y. Wang, H. Jones and P. V. Evans: *J. Mater. Sci.*, 1998, Vol. 33, pp. 5205-5220.

[34] Y. Zhang, Y. Liu, Y. Han, C. Wei and Z. Gao: *J. Alloys Compd.*, 2009, Vol. 473, pp. 442-445.

[35] L. Li, Y. Zhang, C. Esling, H. Jiang, Z. Zhao, Y. Zuo and J. Cui: *J. Appl. Crystallogr.*, 2010, Vol. 43, pp. 1108-1112.

[36] S. G. Shabestari and H. Moemeni: *J. Mater. Process. Technol.*, 2004, Vol. 153-154, pp. 193-198.

[37] K. Liu, X. Cao and X. G. Chen: *Metall. Mater. Trans. A*, 2012, Vol. 43, pp. 1097-1101.

[38] S. Belmares-Perales, M. Castro-Román, M. Herrera-Trejo and L. E. Ramirez-Vidaurri: *Met. Mater. Int*, 2008, Vol. 14, pp. 307-314.

[39] J. Y. Hwang, H. W. Doty and M. J. Kaufman: *Mater. Sci. Eng., A*, 2008, Vol. 488, pp. 496-504.

[40] S. Seifeddine, S. Johansson and I. L. Svensson: *Mater. Sci. Eng., A*, 2008, Vol. 490, pp. 385-390.

[41] D. M. Herlach, *Solidification and crystallization*, Wiley-VCH John Wiley, Weinheim; Chichester, 2004.

[42] A. E. Javitz, *Materials science and technology for design engineers*, Hayden Book Co., New York, 1972.

[43] X. J. Zhai, Y. Fu, X. M. Zhang, Z. Q. Sun and L. Z. Fan: *Light metals*, 2000, Vol. 12, pp. 37-39.

[44] S. J. Maggs, R. F. Cochrane, S. C. Flood and P. V. Evans: *Light Metals*, Minerals, Metals & Materials Soc (TMS), Las Vegas, NV, USA, 1995, pp. 1039-1047.

[45] D. A. Granger: *Light Metals*, Minerals, Metals & Materials Soc (TMS), San Antonio, TX, USA, 1998, pp. 941-952.

[46] J. Campbell, *Castings*, Butterworth-Heinemann, Oxford; Boston, 1991.

[47] K. Liu, X. Cao and X. G. Chen: *J. Mater. Sci.* , 2012, Vol. 47, pp. 4290-4298.

[48] Y. J. Li and L. Arnberg: *Acta Mater.*, 2004, Vol. 52, pp. 2945-2952.

[49] X. Cao and J. Campbell: *Metall. Mater. Trans. A*, 2004, Vol. 35 A, pp. 1425-1435.

[50] B. L. Bramfitt: *Metall. Trans.* , 1970, Vol. 1, pp. 1987-1995.

[51] K. Liu, X. Cao and X. G. Chen: *Metall. Mater. Trans. B*, 2012, Vol. 43, pp. 1231-1240.

[52] W. Khalifa, F. H. Samuel and J. E. Gruzleski: *Metall. Mater. Trans. A*, 2003, Vol. 34, pp. 807-825.

[53] W. T. Denholm, J. D. Esdaile, N. G. Siviour and B. W. Wilson: *Metall. Trans. A*, 1984, Vol. 15 A, pp. 1311-1317.

[54] P. Gilgien, A. Zryd and W.Kurz: *Acta Metall. Mater.*, 1995, Vol. 43, pp. 3477-3487.

[55] R. M. Srivastava, J. Eckert, W. Löser, B. K. Dhindaw and L. Schultz: *Metall. Trans.* , 2002, Vol. 43, pp. 1670-1675.

[56] M. W. Meredith, A. L. Greer and P. V. Evans: *Light metals*, Minerals, Metals & Materials Soc (TMS), San Antonio, TX, USA, 1998, pp. 977-982.

[57] P. V. Evans, J. Worth, A. Bosland and S. C. Flood: *Proceedings of the 4th Decennial International Conference on Solidification Processing (SP'97)*, Univ. of Sheffield, Sheffield, 1997, pp. 531-535.

[58] R. W. Thomas, H. Cama, P. V. Evans and J. D. Hunt: *Proceedings of the 4th Decennial International Conference on Solidification Processing (SP'97)*, Univ. of Sheffield, Sheffield, 1997, pp. 559-563.

[59] C. J. Tseng, Ph. D thesis, Engeering College, National Central University Taiwan, China, 2003.

Chapter 7

MECHANICAL PROPERTIES OF 206 CAST ALLOYS

AT VARIOUS IRON CONTENTS

Chapter 7

Mechanical properties of 206 cast alloys at various iron contents

7.1 Introduction

There have been increasing interests in heat-treatable 206 Al-Cu cast alloys for aerospace and automobile industries due to the high strength and good elevated temperature properties [1]. As is well known, high iron contents can cause significant decrease in mechanical properties (particularly ductility) for cast Al alloys. To this end, extremely low upper limit for iron content is usually set up in the 206 Al-Cu alloy standards, i.e. 0.15% in 206.0 or 0.07% in A206.0 [2] (all alloy compositions are in wt. % unless indicated otherwise). However, the low iron level in the cast Al alloys will not encourage the utilization of iron-rich recycled aluminum alloys, and thus cause the significant increase in manufacturing costs. How to increase the allowable iron content has been a great challenge in designing and developing new 206 Al-Cu cast alloys.

In Chapters 4, 5 and 6, the formation of iron-rich intermetallics in 206 cast alloy at various contents have been dealt with. According to the results, it is found that the

---

iron-rich intermetallics which may appear in the final solidified 206 cast alloys include platelet-like $Al_7Cu_2Fe/Al_7Cu_2(FeMn)$ (β-Fe) [3-6] and $Al_3(FeMn)$ [7, 8] , Chinese script $Al_{15}(FeMn)_3(SiCu)_2$ (α-Fe) [3-5, 9] and Al_mFe [7, 10], depending on the alloy composition, such as the contents of Fe, Mn and Si. These iron-rich intermetallic phases, particularly with platelet morphology can act as stress risers and crack initiators [11-13], and thus have usually been thought to be harmful to the mechanical properties of the cast alloys.

In order to neutralize the detrimental effect of platelet iron-rich intermetallics in Al-Cu cast alloys, Mn and/or Si is added to transform the iron-rich intermetallic from platelet to Chinese script, which is thought to be less harmful to the mechanical properties [13-17]. Though the transformation from platelet to Chinese script has been realized from the point of microstructure evolution [3-5, 7], little work has been performed to quantify the effect of iron-rich intermetallics on the mechanical properties in the 206 cast alloys. Limited studies have been performed on the mechanical properties [1, 6, 14, 16, 18], However, these studies as reviewed above are limited to an iron content up to 0.3%. Little has been known about the effect of the iron-rich intermetallics on the mechanical properties of the 206 family cast alloys at a higher Fe content (i.e. 0.5%). Based on our earlier work [7, 8, 10], the dominant Chinese script Al_mFe or α-Fe intermetallics can be obtained in the 206 cast alloys with 0.5% Fe at cooling rates of 1 K/s, similar to permanent mold casting [8].

Therefore, it is important to quantify the mechanical properties at the high iron 206 cast

alloys and explore the potential of designing and developing new 206 cast alloys with high

iron content. To this end, the effect of iron-rich intermetallics on the tensile properties of

the 206 cast alloys over the iron range from 0.1% to 0.5% has been investigated in this

chapter.

The chemical compositions of the alloys used in this chapter were shown in Table 7.1.

Based on the results obtained in previous studies [4, 5, 7], Baseline B11 and B33 alloys

have 0.15%Fe to obtain dominant platelet and Chinese script iron-rich intermetallics,

respectively. Similarly, Alloys 311 and 333 have 0.3%Fe to dominantly obtain platelet in

Alloy 311and Chinese script in Alloy 333. Alloys 511, 515 and 533 were designed to

investigate the mechanical properties of206 cast alloys with a much higher iron level

(0.5%Fe).

Table 7.1 Chemical compositions of the experimental alloys used (wt. %)

Alloys*	Elements (wt.%)						
	Cu	Mg	Fe	Si	Mn	Ti	Al
B11	4.64	0.27	0.14	0.12	0.12	0.21	Bal.
B33	4.61	0.29	0.16	0.29	0.32	0.21	Bal.
311	4.66	0.27	0.30	0.11	0.12	0.19	Bal.
333	4.62	0.28	0.29	0.29	0.33	0.19	Bal.
511	4.69	0.29	0.51	0.11	0.11	0.20	Bal.
515	4.68	0.29	0.49	0.09	0.51	0.18	Bal.
533	4.64	0.28	0.49	0.30	0.31	0.19	Bal.

*Alloy designation XXX: the first digit stands for Fe content (B is 0.15 wt. % as baseline content) while the second and third digits are for Si and Mn contents, respectively.

Table 7.2 summaries the heat treatment (T4 natural aging and T7 artificial over aging)

used in this work. The detail about the preparation of testing bars and heat treatment

performed on experimental alloys as well as the detail about tensile test can be found in

Chapter 3. Besides, OM, DSC, SEM were used in this chapter to analyze the microstructure

in as-cast and heat treated conditions as well as the fracture surface. The details of these

methods were shown in Chapter 3.

Table 7.2 Heat treatment used in this work

Condition	Solution treatment	Aging treatment
T4	505°C @ 2h+520°C @ 8h	7 days at room temperature
T7	505°C @ 2h+520°C @ 8h	185°C @ 5h

7.2   Microstructures in the as-cast and T7 conditions

The microstructure of a typical Alloy 333in the as-cast and T7 conditions is shown in

Fig. 7.1 (due to the similarity in the iron-rich intermetallics in both T4 and T7 conditions,

the results in T7 are mainly presented here). The Al_2Cu and Chinese script α-Fe are found

to be the two dominant intermetallics in the as-cast condition while platelet β-Fe phase is

seldom observed due to the combined addition of both Mn and Si [4, 5, 8]. However,

almost all the Al_2Cu particles are dissolved into the matrix in the T7 condition (Fig. 7.1b),

which is also confirmed by the DSC heating curves as shown in Fig. 7.1c. In addition to the

peak of Al, four extra peaks for Al_2CuMg/Mg_2Si, Al_2Cu, β-Fe and α-Fe are also detected in

the as-cast condition (Fig. 7.1c). The peak intensity of the β-Fe is very weak due to its low volume fraction. In the T7 condition, the peaks of Al_2CuMg/Mg_2Si and Al_2Cu disappear and only those for β-Fe and α-Fe are still present, which is consistent with the microstructure as observed in Fig. 7.1a. Furthermore, it is noted that some fine β-Fe platelets are observed on Chinese script α-Fe, as shown in Fig. 7.1b. These fine β-Fe platelets are obtained during the solution heat treatment and thus termed solid-state transformed β-Fe (STed β-Fe).These fine β-Fe platelets have similar compositions to the β-Fe that precipitated during casting process (solidification). The formation of the STed β-Fe is also evidenced in the higher peak intensity for the β-Fe in the T7 condition than in the as-cast condition. Detail of the formation mechanism for the STed β-Fe phase was discussed in another paper [19]. However, the fine STed β-Fe is assumed to have less damaging influence on the mechanical properties due to the fine size and low volume fraction under the performed heat treatment [19].
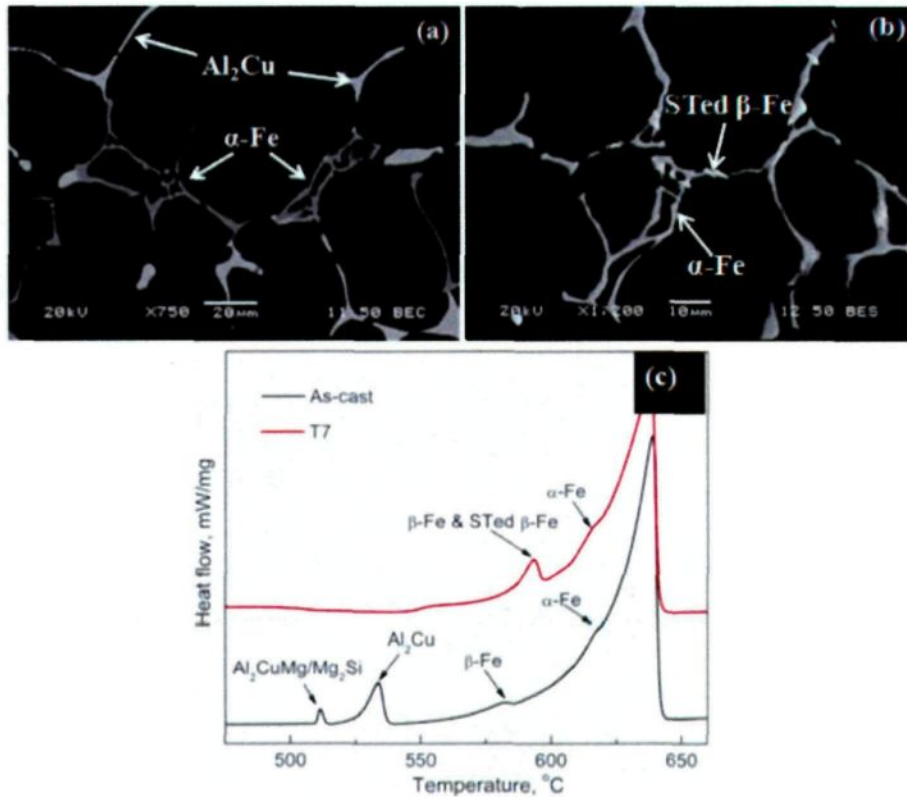
Fig. 7.1 Microstructures in the as-cast (a) and T7 (b) conditions,
and DSC heating curves (c) for Alloy 333 (0.29Fe+0.29Si+0.33Mn)

Figs. 7.2 and 7.3 show the microstructures for all other experimental alloys in the

as-cast and T7 conditions, respectively. In the as-cast condition, it can be found that the

dominant iron-rich intermetallics are platelet β-Fe for Alloys B11 and 311 while the

Chinese script α-Fe becomes the dominant iron-rich intermetallics in Alloys B33 and 333,

which is in consistent agreement with the literatures [4-6, 8]. However, the dominant

iron-rich intermetallics are all Chinese script for Alloys 511, 515 and 533 with 0.5% Fe, as

shown in Figs. 7.2d-7.2f. According to the literature [9, 11] and the EBSD results (they are

not shown here), the Chinese script iron-rich intermetallic are $Al_mFe/Al_m(FeMn)$ in Alloys

511 and 515 but α-Fe in Alloy 533.
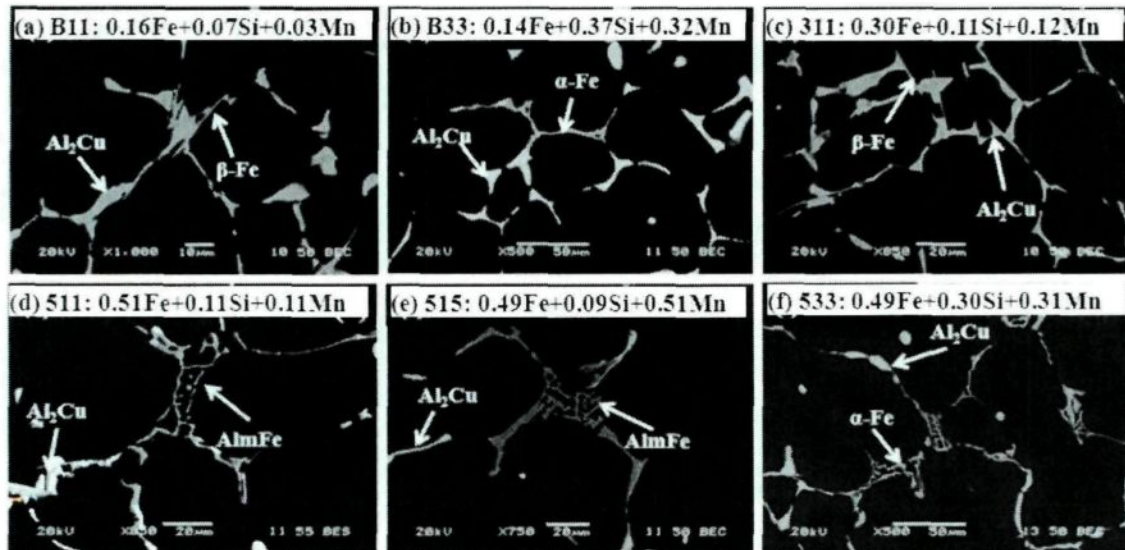
Fig. 7.2 As-cast microstructures of the experimental alloys

As shown in Fig. 7.3, almost all Al_2Cu particles are observed to be dissolved into the

matrix but the iron-rich intermetallics are still present after the T7 heat treatment. In the T7

heat treatment condition, it is noted that the dominant iron-rich intermetallics are platelet

β-Fe in Alloys B11 and 311 but the β-Fe platelets have smaller size and lower volume

fraction in Alloy B11 than in Alloy 311, which can be clearly observed in Fig. 7.3a and

7.3c. In contrast, the dominant iron-rich intermetallics are Chinese script α-Fe in Alloys

B33 and 533, and Chinese script $Al_m(FeMn)$ in Alloys 511 and 515. In addition, some fine

STed β-Fe platelets are also observed around Chinese script $Al_mFe/Al_m(FeMn)$ and α-Fe, as

shown in Fig. 7.3b, 7.3d-7.3f. However, no solid-state transformation has been observed for

platelet β-Fe in Alloys B11 and 311 after the T7 as compared with the as-cast condition, indicating that β-Fe cannot dissolve during the solution treatment.
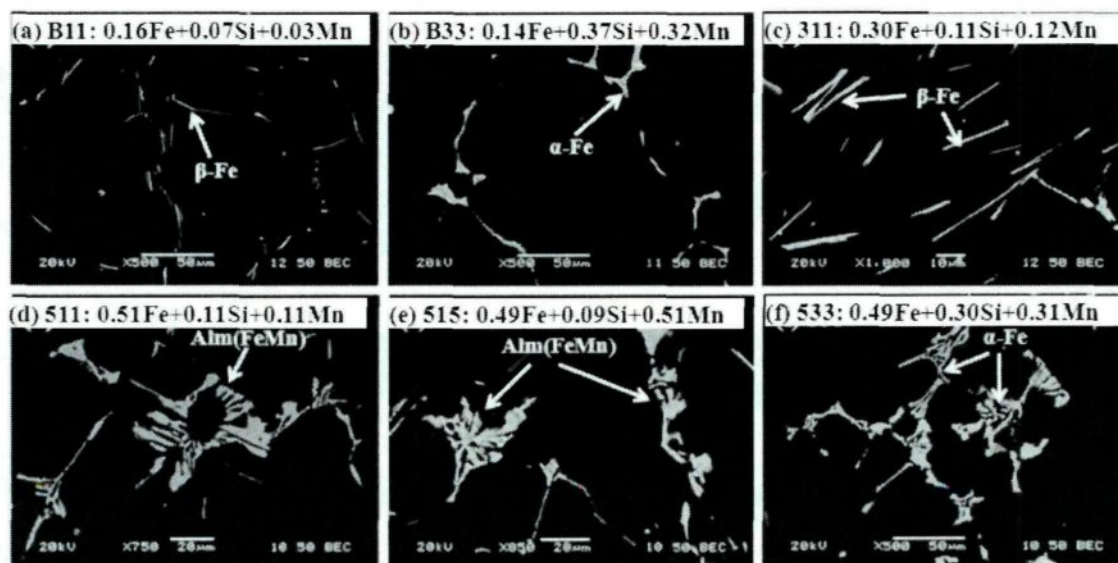
Fig. 7.3 Microstructures of the experimental alloys in the T7 conditions

Based on the microstructures in the as-cast and T7 conditions, it can be concluded that the type of iron-rich intermetallics varies with alloy compositions and the iron-rich intermetallics are difficult to dissolve during the solution treatment. Table 7.3 summarizes the dominant iron-rich intermetallics in the T7 condition for all the experimental alloys.

Table 7.3 Dominant iron-rich phases in the T7 condition

Alloys	B11	B33	311	333	511	515	533
Dominant iron-rich phases	platelet β-Fe	Chinese script α-Fe	platelet β-Fe	Chinese script α-Fe	Chinese script $Al_m(FeMn)$	Chinese script $Al_m(FeMn)$	Chinese script α-Fe

Not only the type of the dominant iron-rich intermetallics but also the volume fraction of the iron-rich intermetallics significantly depended on the alloy composition. Fig. 7.4 shows the volume percent (Vol. %) of the iron-rich intermetallics obtained in all the experimental alloys in the T7 condition.
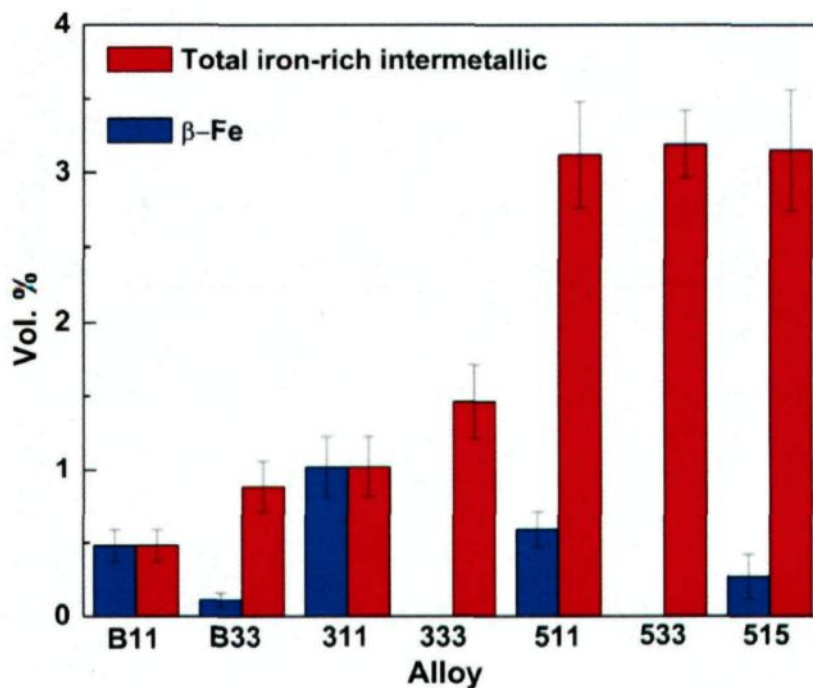
Fig. 7.4 Volume percent (Vol. %) of the iron-rich intermetallics in the T7 condition

Generally, the Vol. % of the total iron-rich intermetallics increases with increasing iron contents, as shown in Fig. 7.4. Similarly to the results shown in Table 7.3 and reported in literatures [5, 8, 11], the image analysis results further show that dominant β-Fe platelets are obtained for Alloys B11 and 311, dominant Chinese script α-Fe for Alloys B33 and 333,

and dominant Chinese script $Al_m(FeMn)/\alpha$-Fe for Alloys 511, 515 and 533. Compared Alloy B11 with Alloy B33, and Alloy 311 with Alloy 333, it can be clearly found that the alloys with dominant Chinese script iron-rich phases have higher Vol. % of the total iron-rich intermetallics than those with dominant platelet iron-rich intermetallics at a given iron level.

7.3   Effect of iron-rich intermetallics on the tensile properties

In this work, both natural aging (T4) and artificial overaging (T7) treatments were performed for the experimental alloys after the solution heat treatment. Fig. 7.5 shows the typical strain-stress curves and the failed samples of Alloy 333 in both the T4 and T7 conditions. It can be found that both the YS and UTS in the T7 are much higher but the elongation is lower than those in the T4 (Fig. 7.5a). The failed tensile samples in the T4 condition have smaller diameters at the fracture location within the gauge length region and thus are much more ductile than those in the T7 condition, as shown in Figs. 7.5b and 7.5c. These differences can be attributed to different precipitation kinetics in the T4 and T7 conditions [20]. Generally, the GP zone (Cu atom-rich clusters) is the dominant precipitates in the T4 condition [20, 21], which is coherent with the matrix and is uniformly distributed with a high volume fraction, leading to higher ductility. In the T7 condition, however, the

GP zone changes to θ′ (Al_2Cu) [20, 21] which is semi-coherent with the matrix and has the highest strengthening effect, leading to higher strength but lower ductility in the T7 condition.
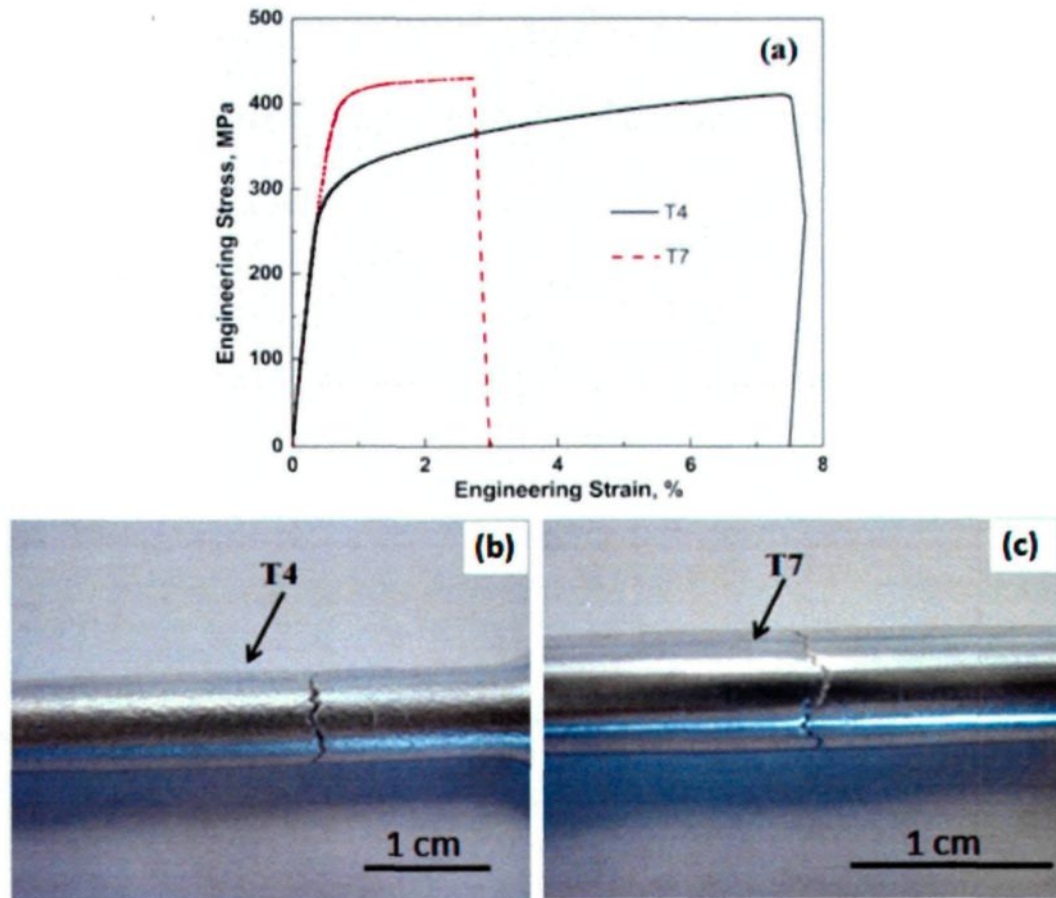
Fig. 7.5 Engineering stress-stain curves (a), and failed samples
in T4 (b) and T7 (c) conditions for Alloy 333

Fig. 7.6 shows the tensile properties, including the strengths (YS and UTS) and El of Alloys B11, 311 and 511 with various iron contents but similar low Si and low Mn additions in both the T4 and T7 conditions. It can be found that all the tensile properties

(YS, UTS and El) decrease with increasing iron content, which is in consistent with the literatures [4, 7, 22]. However, the YS in T4 condition decreases very slightly with increasing iron content, which can be resulted from the similar Cu contents in experimental alloys. It is reported that the YS is greatly related to the dendrite structure, where the iron content is negligible while Cu content is similar [17]. The significant decreases in UTS, YS and El with increasing iron content can mainly be attributed to (i) increasing volume fraction and (ii) larger size of the iron-rich intermetallics, and (iii) associated decreasing Cu available for aging strengthening during the later heat treatment. As indicated in Fig. 7.4, the Vol. % of the total iron-rich intermetallics is only about 0.5% for Alloy B11, 1% for Alloy 311 but 3% for Alloy 511. Platelet β-Fe is the dominant iron-rich phase for both Alloys B11 and 311 but the larger size (length and width) and higher volume fraction lead to the decrease in the tensile properties for Alloy 311 compared to Alloy B11. Compared with Alloys B11 and 311, Alloy 511 has much more iron-rich intermetallics (with dominant Chinese script $Al_m(FeMn)$ and some β-Fe platelets),resulting in the further decrease in the tensile properties.
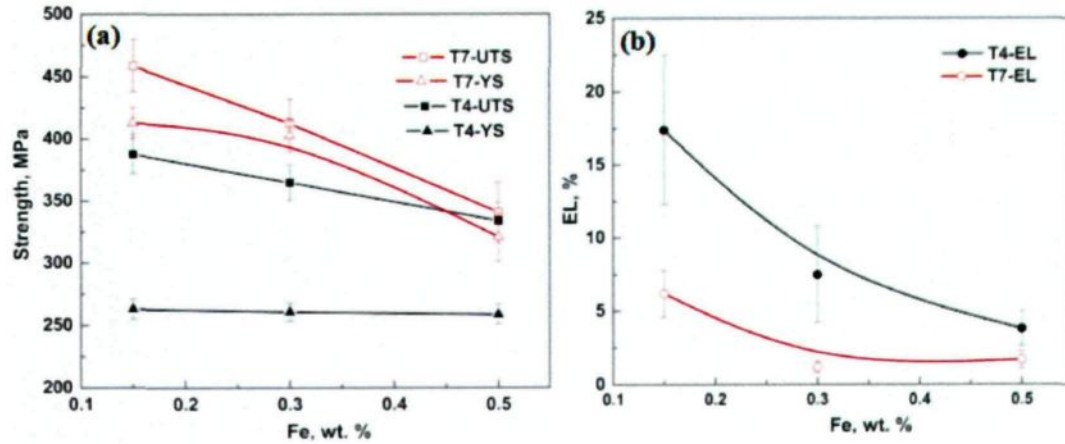
Fig. 7.6 Tensile properties of Alloys B11, 311 and 511in T4 and T7 conditions

Tseng *et al.* [7] reported that the relationship between tensile strength (YS and UTS) and iron content in the T71 condition for 206 cast alloys can be described as:

$$\sigma = a \times (\text{wt. \%Fe}) + b \ (0.05\% \leq \text{Fe} \leq 0.25\%) \tag{1}$$

Similarly, the liner relationship between YS, UTS and iron content is also found in the present study and the upper limitation of the iron content can be extended to 0.5% despite different *a* and *b* values. Table 7.4 shows the *a* and *b* values from the fitting curves of the strength shown in Fig. 7.6 in the present work and those from the literature [7].

Table 7. 4 Constant values for *a* and *b* in Equation 1 obtained
in the present work and from literature [7]

Alloys	Iron contents	YS T4		YS T7		UTS T4		UTS T4	
		a	b	a	b	a	b	a	b
Tseng et al. [7]	0.05-0.25%			-137	359			-160	434
Present work	0.15-0.5%	-14	265	-241	458	-153	411	-214	487

As shown in Figs. 7.1-7.4, Alloys B11 and 311 have dominant platelet β-Fe while the dominant iron-rich intermetallics in Alloys B33, 333, 511 and 533 are nearly all Chinese script $Al_m(FeMn)/\alpha$-Fe. Fig. 7.7 shows the tensile strength (YS and UTS) of these experimental alloys in the T7 condition. It can be found that the both the YS and UTS are improved with the transformation of dominant iron-rich intermetallics from the platelet β-Fe to the Chinese script α-Fe.
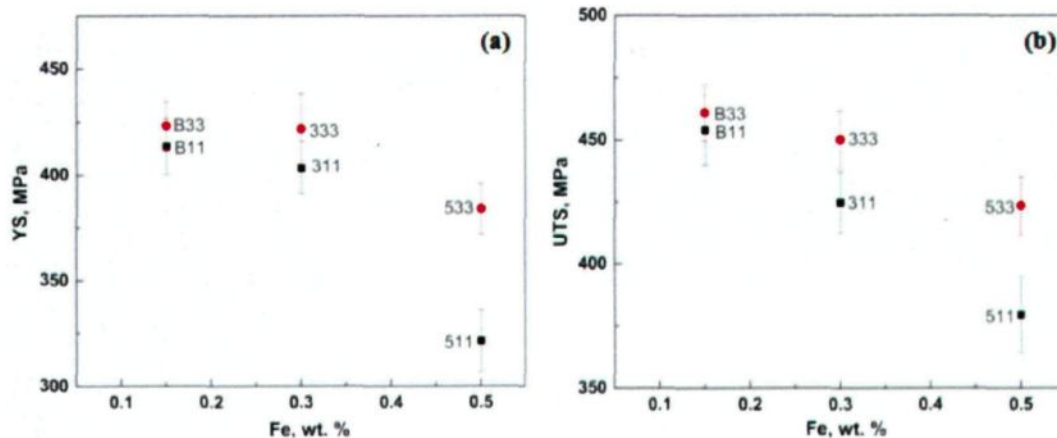
Fig. 7.7 Tensile strengths of Alloys B11, B33, 311, 333, 511 and 533 in T7condition

With the transformation of dominant iron-rich intermetallics from the platelet β-Fe to the Chinese script α-Fe/Al$_m$(FeMn), the improvement of the YS and UTS increases with increasing iron content. For example, the increase in UTS is only 13 MPa from B11 to B33 but 30 MPa from 311 to 333. This can be attributed to the change of the morphology and the Vol. % of the iron-rich intermetallics. Compared with Alloy B11, the dominant iron-rich intermetallics in Alloy B33 have been transferred from the platelet β-Fe to the Chinese script α-Fe although the Vol. % of the total iron-rich intermetallics has almost been doubled (from 0.5% to 0.9% as indicated in Fig. 7.4). This increase in UTS (13 MPa) is small but it is clearly demonstrated that the transformation of the iron-rich phase shape is effective to improve the tensile strength. For both Alloys 311 and 333, the Vol. % of the total iron-rich intermetallics is similar (1-1.5%) but the dominant iron-rich intermetallics are Chinese script α-Fe for Alloy 333 and platelet β-Fe for Alloy 311, resulting in a significant improvement in UTS (30 MPa) [4, 20]. In addition, the Cu content in α-Fe (5 at. %) is much lower than that in β-Fe (20 at. %) [5, 6], indicating that more Cu is available for the aging strengthening of the matrix when the α-Fe is mainly presented. As a result, the improvement in UTS between Alloy 311 and Alloy 333 is much larger than that in the Alloys at 0.15% Fe. An improvement in both YS and UTS between Alloy 511 and 533 is also shown in Fig. 7.7 though the dominant iron-rich intermetallics are both Chinese script

(Al_m(FeMn) for Alloy 511 and α-Fe for 533). This difference is probably due to the presence of platelet β-Fe in Alloy 511 (0.5 Vol. %), leading to the lower strength for Alloy 511. In addition, it is reported that α-Fe is more branched that Al_m(FeMn) [9], which is beneficial to improve the tensile strength due to higher resistance to the tensile stress [18, 23, 24].

7.4 Fracture analyses

To further explain the tensile properties, the fracture surfaces were observed by using SEM. Alloys 311 and 333 are selected as the typical materials to disclose the failure mechanisms in the present work.

As is well known, oxide films are most damaging to the mechanical properties due to their crack nature [25-27]. Fig. 7.8 shows some oxide films taken from Alloys 311 and 333. It can be observed that cracking is along the oxide film as shown in Figs. 7.8a, 7.8c and 7.8d, confirming the detrimental effect of the oxide films on the tensile properties. In addition, α-Fe is found to be adjacent with an oxide film in Fig. 7.8e, indicating the nucleation of α-Fe on oxide films [5, 28, 29].
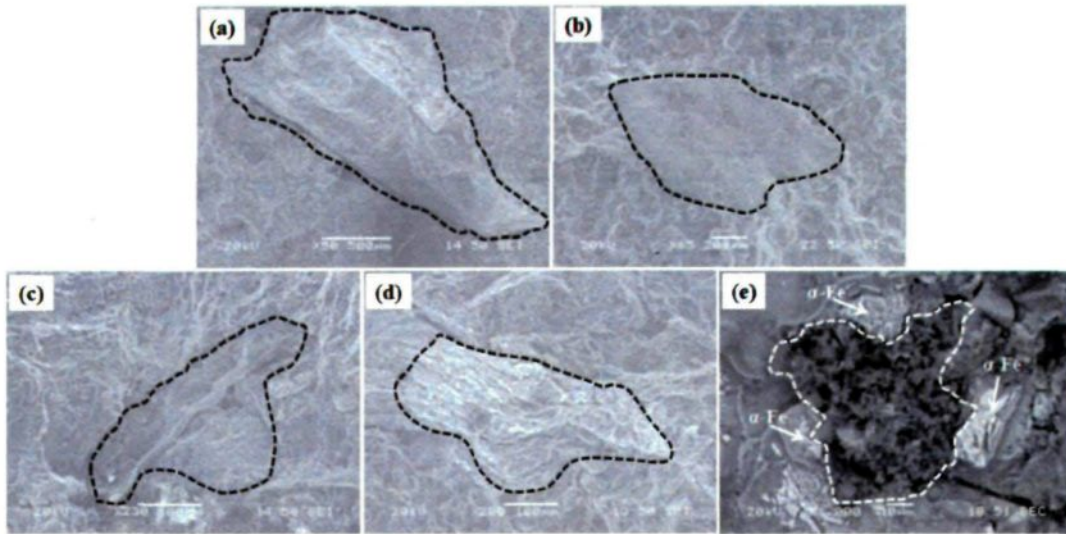
Fig. 7.8 Oxide films observed in Alloy 311 (a, b) and Alloy 333 (c-e)

As shown in Fig. 7.8, it can be found that the surface area of the oxide films in Figs. 9a and 9b are much larger than those in Figs. 7.8c-e. However, they all are identified to be "old" alumina or spinel oxide films originated from the original master alloys or formed during the melting from the EDS results [25]. Fig. 7.9 shows two typical SEM-EDS results of Fig. 7.8b as old alumina and Fig. 7.8d as old spinel.
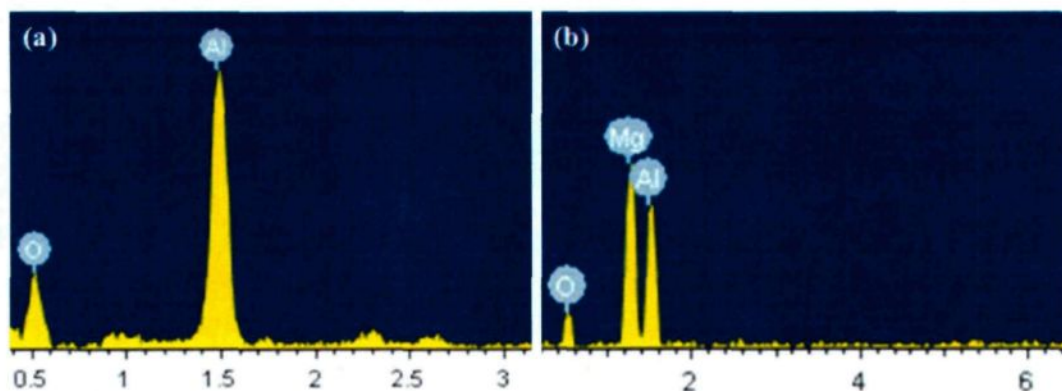
Fig. 7.9 SEM-EDS results of the oxide films
(a) old alumina in Fig. 7.8b and (b) old spinel in Fig. 7.8d

Due to the similarity in melting and casting processes and the Mg content, the characters and volume fractions of the oxide films in the experimental alloys are assumed to be similar and thus the iron-rich intermetallics may govern the tensile properties of the experimental alloys.

Fig. 7.10 shows the SEM secondary electron images obtained on the fracture surfaces of Alloys 311 and 333 in the T7 condition. The mixed ductile dimples and brittle cleavage surfaces can be observed in the two alloys but more ductile dimples are found in Alloy 333 (Figs. 7.10a and 7.10c), explaining the higher YS, UTS and El [15, 20, 30]. It is found that some β-Fe platelets are present between two adjacent dimples along the crack propagation direction for Alloy 311 (Fig. 7.10b), leading to the easy propagation of the crack. However, the presence of Chinese script α-Fe in Alloy 333 induces an effective deflection of the cracking paths along its arms and thus the cracks seem difficult to propagate along one

direction [24], as shown in Fig. 7.10d, further confirming the less-damaging effect of the Chinese script α-Fe on the tensile properties and thus explaining the improved YS, UTS and El in Alloy 333 over Alloy 311.
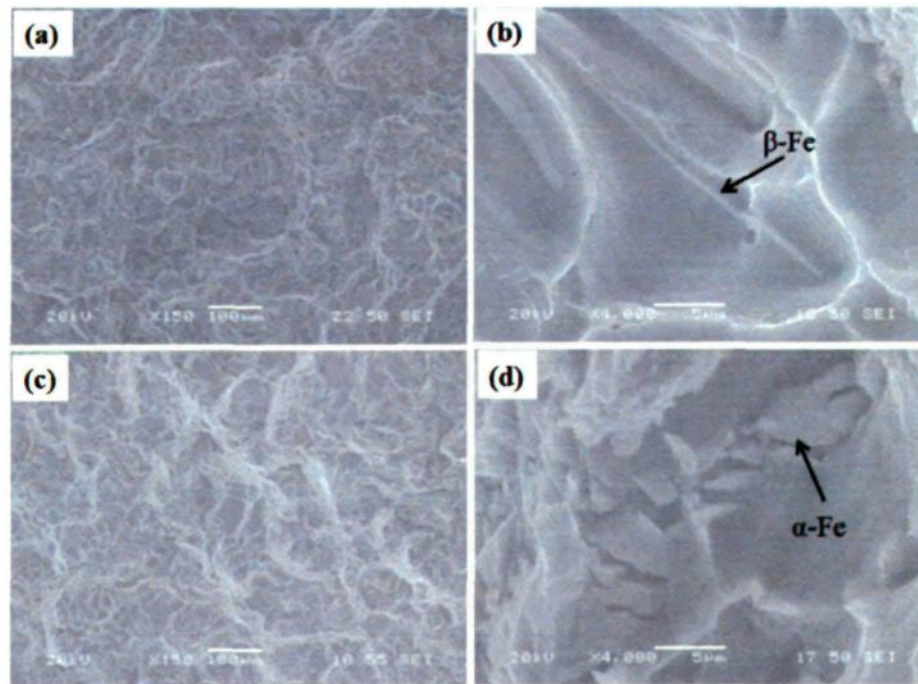
Fig. 7.10 Fracture surfaces of Alloys 311 (a-b) and 333 (c-d) in the T7 condition

The longitudinal sections towards the fracture surface of Alloys 311 and333 are shown in Fig. 7.11. The crack is clearly propagated along the β-Fe platelets for either the primary crack on the fracture surface (Fig. 7.11a) or the secondary crack in the matrix (Fig. 7.11b). However, the crack is deflected along the arms of the Chinese script α-Fe in Alloy 333 (Fig. 7.11c) and thus small cracks with different orientations are observed on the branches of the

Chinese script α-Fe (Fig. 7.11d). As a result, the crack is more difficult to propagate towards the fracture surface during the tensile testing, leading to less damaging effect of the Chinese script α-Fe on the tensile properties than the platelet β-Fe [24, 31].
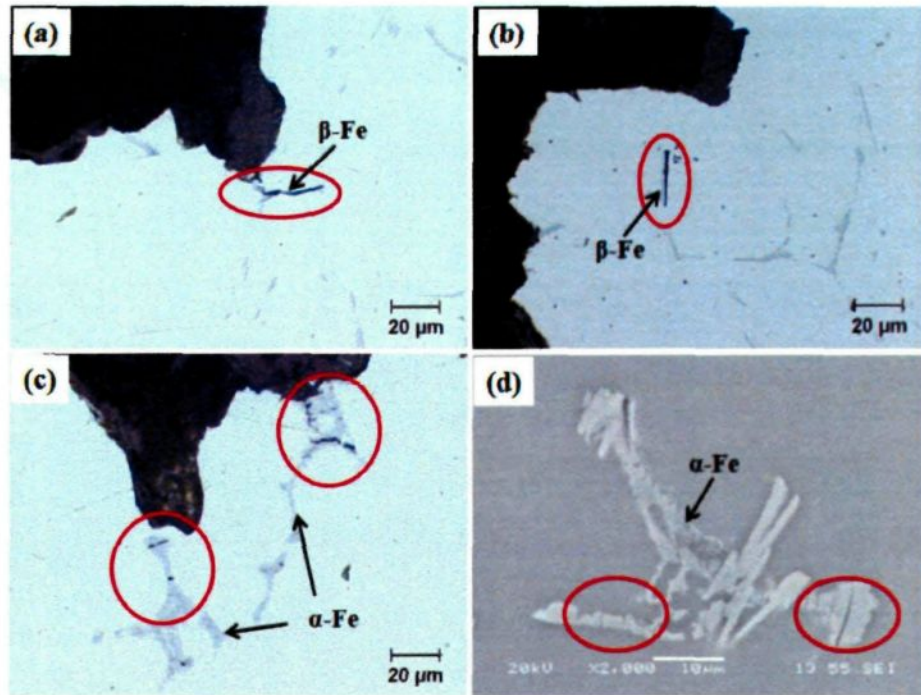
Fig. 7.11 Longitudinal sections towards the fracture surfaces
of Alloys 311 (a-b) and 333 (c-d) in the T7 condition

7.5 Quality index

The quality index (QI) is an effective indicative of the casting quality which has combined both the tensile strength and ductility. It can be used to characterize the influence of alloy chemistry and heat treatment on the combined tensile properties [32, 33]. The

quality index of the experimental alloys can be calculated using the following equation [1, 34, 35] and the results are shown in Table 7.5.

$$QI = UTS + d\log E \tag{2}$$

Where, QI and UTS are given in MPa and d is the material constant (270 for the 206 cast alloys [1]) while E is the El at fracture.

Table 7.5 Quality index of all the experimental alloys used in this work

Alloys		B11	B33	311	333	511	515	533
Quality index	T4	722	660	565	686	491	603	609
QI (MPa)	T7	668	492	446	583	442	489	545

Generally, the QI values in the T4 condition are higher than those in the T7 condition due to the higher elongation [1]. In addition, the QI varies with alloy compositions. It can be found that the QI decreases with increasing iron contents and thus the best combination of the tensile properties is obtained in alloys at low iron contents. For the alloys at a similar iron content, QI is higher in the presence of the dominant iron-rich intermetallics in Chinese script than in platelet such as Alloys 333 and 311, Alloys 533 and 511. However, Alloys B33 and B11 are off this tendency, probably due to the excessive presence of the oxide film, leading to the low elongation for Alloy B33.

For 206 cast alloys at lower iron contents, Sigworth *et al.* [1] calculated the QI at various chemical compositions. In their work, QI was reported to be about 730 MPa with an elongation of 17% in T4 while 675 MPa with an elongation of 6% in T7 conditions when the iron ranged from 0.05% to 0.25%, which is similar to the QI obtained in the present work for Alloy B11 at 0.15% Fe that 722 MPa with an elongation of 17.4% in T4 and 668 MPa with an elongation of 6.2% in T7 condition, confirming the reliability of the methodology used in the present work.

Compared with the QI at low iron contents, it seems that the QI of the alloys at high iron contents with dominant Chinese script α-Fe, such as Alloy 333 (686 MPa in T4 condition) and Alloy 533 (609 MPa in T4 condition) is still very high, indicating the great potential of developing new high iron 206 cast alloys under well controlled alloy chemistry, casting and hear treatment processes.

7.6   Prospect of high iron 206 cast alloys

The tensile properties of all the experimental alloys in both T7 and T4 conditions are shown in Fig. 7.12. Although the tensile strength decreases with increasing iron content, the declining extent is only about 15-25%. For instance, the YS and UTS decrease from maximum 400 and 460 MPa for Alloy B33 to minimum 314 and 380 MPa for Alloy 511,

respectively, over Fe contents ranging from 0.15% to 0.5%. These lowest strengths still are even higher than majority of other cast aluminum alloys [36]. The requirements of the tensile properties for the 206 cast alloys depend on their applications, e.g. high strength and moderate ductility (3-5%) for aerospace but moderate strength and high elongation (>7%) for safety-critical suspension components in the automobile industries [1]. As shown in Fig. 7.12, it can be found that the best combination of both the tensile strength and the elongation can be obtained at lower iron levels with lower volume fractions of the iron-rich intermetallics in T7 or T4 conditions. However, the elongation of all the experimental alloys in the T7 is found to be lower than the minimum 7% requirement for the automotive applications (Fig. 7.12b). In contrast, the elongation values of the experimental alloys except for Alloys 311 and 511 are all higher than 7% in the T4 condition in spite of slightly lower strength (Fig. 7.12a). For instance, the elongation of Alloy 333 increases from 3% in the T7 to 12% in the T4 while the UTS decreases from 450 MPa in theT7 to 395 MPa in the T4 conditions. In addition, it is interesting to note that Alloys 515 and 533 with 0.5%Fe in the T4 condition have quite similar combined properties (370 MPa and 7.5%, 365 MPa and 7.8%, respectively) to Alloy 333 with 0.3% Fe.
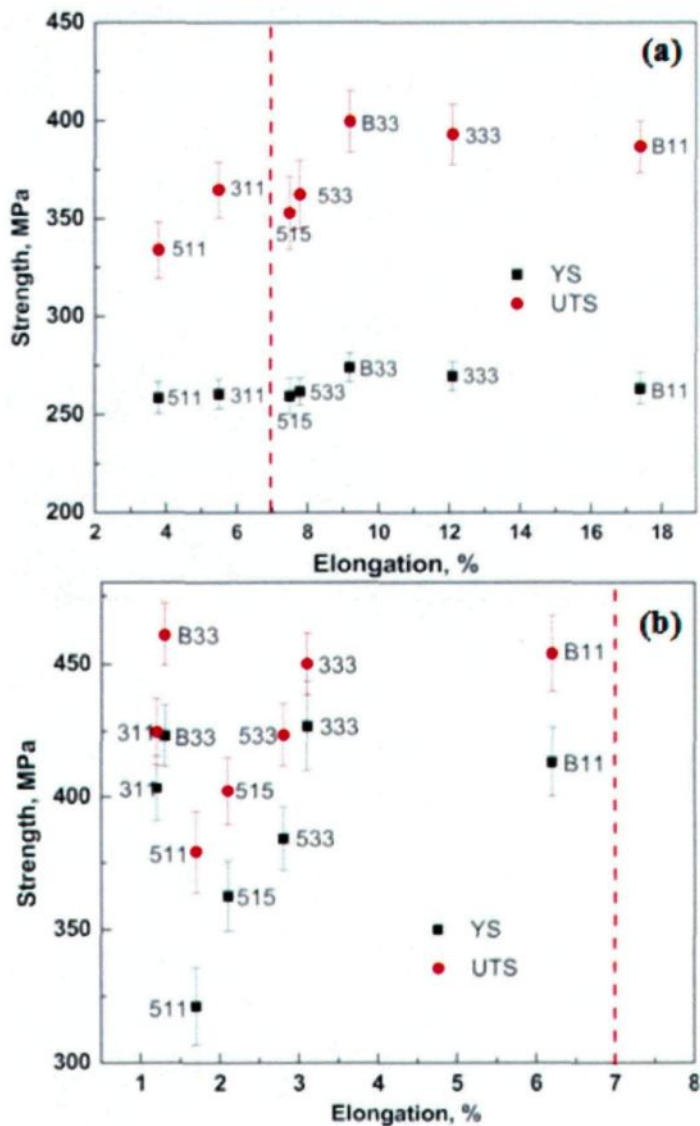
Fig. 7.12 Tensile properties for all the experiment alloys
in the T4 (a) and T7 (b) conditions

Kamga *et al.* [17] reported that the minimum requirement of elongation (7%) is

difficult to meet in the T7 condition but possible in the T4 conditions at 0.1-0.3% Fe with a

Fe/Si ratio close to 1. In the present work, it is found that the elongation is still higher than

7% despite slightly reduced strength at 0.5% Fe for Alloys 533 and 515 and hence the upper limitation of the iron content can be extended up to 0.5%. In addition, it is found that the Fe/Si ratio to obtain the premium mechanical properties is not a constant but varies with iron level. For instance, the mechanical properties of Alloys B33, 333 and 533 are found to be better than the other experimental alloys at a similar iron level. However, the Fe/Si ratios are 0.5 for Alloy B33, 1 for Alloy 333 and 1.7 for Alloy 533 indicating a wide tolerance of the Si contents [5, 6, 11]. In addition, it is found that not only Fe/Si but also Fe/Mn ratio can influence the mechanical properties. In Alloy 515 with a Fe/Si ratio of 5 and a Mn/Fe ratio of 1, the mechanical properties are also found to meet the industrial requirements.

Table 7.6 shows the mechanical properties of Al-Si-Cu alloys with various iron contents [36] as compared to some typical alloys used in the present work. It can be found that some 206 cast alloys developed in the present work have much higher strength but similar ductility in spite of higher iron content, indicating the more compatible combination of 206 alloys between strength and elongation in either T4 or T7 condition. For instance, despite similar elongation for Alloy 333 and Alloy 356.0, the tensile strengths (UTS, YS) of Alloy 333 at 0.29% Fe are 393 MPa and 270 MPa, which are much higher than 285 MPa and 205 MPa for Alloy A356.0 at 0.2% Fe. Furthermore, it can be found that the tensile properties (UTS, YS and El) of Alloy 533 at 0.5%Fe in T4 condition are much higher than

those for Alloy 357.0 with only 0.15%Fe and 359.0 with 0.2%, as shown in Table 7.6

indicating the great potential of developing new high iron 206 cast alloys since the wider

applications of the 206 Al-Cu cast alloys have mainly been limited by the extremely low

iron content presently. Moreover, it is also possible to cast 206 alloys using recycled

aluminum alloys to reduce the manufacturing costs. In the future, more investigations will

be carried out to evaluate other properties such as fatigue and corrosion for the high-iron

206 cast alloys.

Table 7.6 Tensile properties of Al-Si-Cu alloys in literature [36]
and Al-Cu alloys used in the present work

Source	Alloy	Fe (wt. %)	Condition	UTS (MPa)	YS (MPa)	El (%)
Literature[36]	357.0	0.15*	T7	260	205	5
	A356.0	0.20*	T6	285	205	12
	359.0	0.20*	T6	330	255	6
Present work	333	0.29**	T4	393	270	12
			T7	450	427	3
	533	0.49**	T4	362	262	8
			T7	424	384	3

Note: *Nominal iron content in Al-Si-Cu alloys; **Actual iron content in Al-Cu alloys

7.7 Summary

(1) Both tensile strength and elongation decrease with increasing iron content, due to the increasing volume fraction of the iron-rich intermetallics and decreasing Cu available for the precipitation-hardening effect.

(2) Similar to the tensile properties, quality index (QI) decreases also with increasing iron content. Higher QI can be obtained in the alloys dominantly with Chinese script iron-rich intermetallics than platelet Fe-rich phases at a similar iron content.

(3) At a similar iron level, Chinese script iron-rich intermetallics ($Al_m(FeMn)$ and α-Fe) are less damaging to the tensile properties than a platelet iron-rich phase β-Fe. During the tensile testing, the crack is deflected along the branches/arms of the Chinese script iron-rich intermetallics, making it more resistant to propagate while the crack is much more easily propagated along the platelet iron-rich intermetallics.

(4) For the 206 cast alloys at higher than 0.15% Fe in the T7 condition, it is difficult to meet the minimum requirement of the elongation (7%) for the automotive application due to the rapid drops of the tensile properties at high iron contents. However, the upper iron limitation can be extended to 0.3%, or even 0.5% to meet the 7% elongation in the T4 condition under well controlled alloy chemistry, casting and heat treatment processes, indicating the great potential of developing new high iron 206 cast alloys.

References

[1] G.K. Sigworth, J. Fred Major, in: T.J. Galloway (Ed.) Light Metals, Minerals, Metals & Materials Soc (TMS), San Antonio, TX, 2006, pp. 795-799.

[2] V.S. Zolotorevsky, N.A. Belov, M.V. Glazoff, Casting aluminum alloys, Elsevier Science, Oxford, 2007.

[3] N.A. Belov, A.A. Aksenov, D.G. Eskin, Iron in aluminum alloys: impurity and alloying element, Taylor & Francis, London, 2002.

[4] H. Kamguo Kamga, D. Larouche, M. Bournane, A. Rahem, Metall. Mater. Trans. A, 41 (2010) 2844-2855.

[5] K. Liu, X. Cao, X.G. Chen, Metall. Mater. Trans. A, 42 (2011) 2004-2016.

[6] K. Liu, X. Cao, X.G. Chen, Metall. Mater. Trans. B, 43B (2012) 1231-1240.

[7] C.J. Tseng, S.L. Lee, T.F. Wu, J.C. Lin, Mater. Trans., JIM, 41 (2000) 708-713.

[8] K. Liu, X. Cao, X.G. Chen, in: D.Gallienne, M. Bilodeau (Eds.) Light Metal – Advances in Materials and Processes, Met. Soc, Vancouver, BC, Canada, 2010, pp. 113-120.

[9] K. Liu, X. Cao, X.G. Chen, Metall. Mater. Trans. A, 43 (2012) 1097-1101.

[10] K. Liu, X. Cao, X.G. Chen, J. Mater. Sci. , 47 (2012) 4290-4298.

[11] K. Liu, X. Cao, X.G. Chen, Metall. Mater. Trans. A, online published, DOI:10.1007/s11661-012-1419-7, (2012).

[12] S. Seifeddine, S. Johansson, I.L. Svensson, Mater. Sci. Eng., A, 490 (2008) 385-390.

[13] S.G. Shabestari, Mater. Sci. Eng., A, 383 (2004) 289-298.

[14] S.S. Sreeja Kumari, R.M. Pillai, T.P.D. Rajan, B.C. Pai, Mater. Sci. Eng., A, 460-461 (2007) 561-573.

[15] C.J. Tseng, S.L. Lee, S.C. Tsai, C.J. Cheng, J. Mater. Res., 17 (2002) 2243-2250.

[16] L. Zhang, W.L. Jiao, H.J. Yu, G.C. Yao, Chin. J. Nonferrous Met., 15 (2005) 368-373.

[17] H.K. Kamga, D. Larouche, M. Bournane, A. Rahem, Int. J. Cast Met. Res., 25 (2012) 15-25.

[18] J.Y. Hwang, H.W. Doty, M.J. Kaufman, Mater. Sci. Eng., A, 488 (2008) 496-504.

[19] K. Liu, X. Cao, X.G. Chen, submitted to Metall. Mater. Trans. A ,(2012).

[20] C.J. Tseng, Ph. D Thesis, Engeering college, National Central University, Taiwan, China, 2003.

[21] S.K. Son, M. Takeda, M. Mitome, Y. Bando, T. Endo, Mater. Lett., 59 (2005) 629-632.

[22] A. Couture, Int. Cast Met. J., 6 (1981) 9-17.

[23] L. Ceschini, I. Boromei, A. Morri, S. Seifeddine, I.L. Svensson, J. Mater. Process. Technol., 209 (2009) 5669-5679.

[24] L. Ceschini, I. Boromei, A. Morri, S. Seifeddine, I.L. Svensson, Mater. Des. , 36 (2012) 522-528.

[25] X. Cao, J. Campbell, Can. Metall. Q., 44 (2005) 435-448.

[26] X. Cao, J. Campbell, Int. J. Cast Met. Res., 17 (2004) 1-11.

[27] X. Cao, J. Campbell, AFS Trans., 108 (2000) 391-400.

[28] X. Cao, J. Campbell, Metall. Mater. Trans. A, 34 (2003) 1409-1420.

[29] X. Cao, J. Campbell, Metall. Mater. Trans. A, 35 A (2004) 1425-1435.

[30] M. Warmuzek, in, ASM International, Materials Park, OH, 2004.

[31] J. Lapin, T. Pelachova, Microstructure and mechanical properties of wrought aluminium alloy prepared by recycling of aluminium matrix composites reinforced with Inconel 601 fibres, Elsevier, Kidlington, ROYAUME-UNI, 1999.

[32] M. Tiryakioğlu, J. Campbell, N.D. Alexopoulos, Metall. Mater. Trans. B, 40 (2009) 802-811.

[33] N.D. Alexopoulos, J. Mater. Eng. Perform., 15 (2006) 59-66.

[34] C.H. Cáceres, Int. J. Cast Met. Res., 10 (1998) 293-299.

[35] C.H. Cáceres, J. Mater. Eng. Perform., 9 (2000) 215-221.

[36] J.G. Kaufman, E.L. Rooy, American Foundry Society, in, ASM International, Materials Park, OH, 2004.

Chapter 8

CONCLUSIONS AND FUTURE WORK

Chapter 8

Conclusions and future work

8.1 Conclusions

In this work, systematical experimental investigations were carried out for a series of 206 Al-Cu cast alloys at various iron contents (0.15%, 0.3% and 0.5%) with regard to the solidification behaviors of the iron-rich intermetallic phases. The main factors influencing the iron-rich intermetallics were studied, such as the addition of Mn and/or Si, and cooling rate. In addition, the effects of the alloy compositions and the associated iron-rich intermetallics on the tensile properties of the 206 cast alloys were evaluated at various iron contents. Based on this study, the following conclusions can be drawn:

(1) Both Chinese script α-Fe and platelet-like β-Fe phases are observed to be the two main iron-rich phases and can coexist in the finally solidified 206 at an iron content up to 0.3%. In addition to the Chinese script α-Fe and platelet β-Fe, however, two new iron-rich phases, i.e. Chinese script $Al_mFe/Al_m(FeMn)$ and platelet $Al_3(FeMn)$ are experimentally observed, for the first time, in the 206 cast alloys at 0.5% Fe.

(2) The full solidification sequences and reactions of all the iron-rich intermetallics in the 206 cast alloys at iron contents of 0.15%, 0.3% and 0.5% have been systematically established.

(3) All the iron-rich intermetallics can nucleate on the oxide films but the intermetallic phases precipitated later can also nucleate on those formed earlier. For example, β-Fe is observed to nucleate on the earlier formed α-Fe or $Al_3(FeMn)$ while α-Fe may nucleate on $Al_6(FeMn)$ or $Al_m(FeMn)$.

(4) For the two iron-rich intermetallic phases (i.e. Chinese script α-Fe and platelet-like β-Fe) at an iron content of up to 0.3%, it is found that the individual addition of either Mn or Si promotes the formation of α-Fe and hinders the occurrence of β-Fe. However, the combined addition of both Mn and Si has a synergistic effect on the transformation from platelet β-Fe to Chinese script α-Fe phase.

(5) For the four iron-rich intermetallic phases (i.e. Chinese script α-Fe and $Al_m(FeMn)$, platelet-like β-Fe and $Al_3(FeMn)$) as obtained at 0.5% Fe, it is found that $Al_m(FeMn)$ preferably precipitates at low Si and Mn levels. The individual addition of Si favors the formation of α-Fe but inhibits the precipitation of β-Fe while the individual addition of a high Mn level promotes the formation of $Al_3(FeMn)$. The combined addition of both Si and Mn enhances the formation of predominate α-Fe.

(6) The volume fraction and formation temperature increase for α-Fe but decrease for β-Fe with increasing cooling rate at an iron content of up to 0.3%. At 0.5% Fe, the formation of $Al_m(FeMn)$, α-Fe, $Al_3(FeMn)$ and $Al_6(FeMn)$ is also related to the cooling rate. $Al_3(FeMn)$ is generally considered to be stable but $Al_6(FeMn)$ and $Al_m(FeMn)$ are metastable iron-rich intermetallics. At high Mn (0.53%) and low Si, however, $Al_6(FeMn)$ becomes stable, and $Al_3(FeMn)$ and $Al_m(FeMn)$ are metastable phases. With increasing cooling rate, the formation temperature of each iron-rich intermetallic phase decreases and the stable iron-rich intermetallic is gradually replaced by the metastable phases.

(7) There exists a critical cooling rate which depends on the alloy composition to effectively suppress the formation of β-Fe to obtain the dominant Chinese script iron-rich intermetallics but a lower threshold is obtained at higher Mn/Fe and Si/Fe ratios. For a given composition of the 206 cast alloys with addition of 0.2% Si and 0.2% Mn, the critical cooling rate is about 1.5 K/s at 0.15% Fe, 1 K/s at 0.3% Fe and 0.2 K/s at 0.5% Fe, which is lower than those used in industrial permanent mold casting condition (2-3 K/s). Therefore, the 206 alloys can be cast with dominant Chinese script iron-rich intermetallics in normal industrial casting conditions under well controlled alloy compositions and cooling rate.

(8) During the solution heat treatment, Al_2Cu is observed to dissolve into the matrix while little change is observed for platelet β-Fe but the solid-state phase transformation

from α-Fe into β-Fe is found as evidenced by the appearance of some newly formed fine β-Fe platelets which can nucleate on and grow from the Chinese script α-Fe.

(9) Similar to the tensile properties, quality index (QI) decreases also with increasing iron content. Higher QI can be obtained in the alloys dominantly with Chinese script iron-rich intermetallics than platelet Fe-rich phases at a similar iron content.

(10) At a similar iron level, Chinese script iron-rich intermetallics (Al_m(FeMn) and α-Fe) are less damaging to the tensile properties than a platelet iron-rich phase β-Fe During the tensile testing, the crack is deflected along the branches/arms of the Chinese script iron-rich intermetallics, making it more resistant to propagate while the crack is much more easily propagated along the platelet iron-rich intermetallics.

(11) For the 206 cast alloys at higher than 0.15% Fe in the T7 condition, it is difficult to meet the minimum requirement of the elongation (7%) for the automotive application due to the rapid drops of the tensile properties at high iron contents. However, the upper iron limitation can be extended to 0.3%, or even 0.5% to meet the 7% elongation in the T4 condition under well controlled alloy chemistry (Fe, Mn and Si contents), casting and heat treatment processes, indicating the great potential of developing new high iron 206 cast alloys.

8.2 Future work

The iron-rich intermetallics have been systematically investigated in the 206 cast alloys with iron contents ranging from 0.15% to 0.5% and some significant progresses have already been obtained. To further develop high-iron 206 cast alloys, there is still some important work to be done in the future:

(1) Sr is reported to have an important influence on the modification of the iron-rich intermetallics in Al-Si cast alloys. Therefore, the systematical study on the effect of Sr on the formation and transformation of iron-rich intermetallics in Al-Cu 206 cast alloys should be performed.

(2) Hot tearing is always a main challenge as encountered in the 206 cast alloys. Therefore, a study on the castability, especially the hot tearing at high iron levels should be performed.

(3) A comprehensive study of iron level and iron-rich intermetallics on the quality index of 206 alloys should be deeply performed. Besides, other physical and mechanical properties such as corrosion resistance and fatigue properties should be investigated to evaluate the overall properties of the 206 cast alloys at high iron levels.

(4) In this study, T4 and T7 have been performed on 206 cast alloys with various iron contents. However, a study on the effect of heat treatment on the mechanical properties is

needed to further optimize the heat treatment procedures, such as retrogressing and re-aging (RAA) treatments to further improve the mechanical properties of the 206 cast alloy at a high level of iron.

(5) A detailed study on fractography by using SEM, specially the observation of the cast defects such as oxide films is needed to better understand the failure mechanisms during the tensile testing.

(6) The precipitation behavior of the 206 cast alloys will be influenced by the variation of the compositions, such as Mn and Si additions and the solidified cooling rate. Therefore, a study on the precipitation kinetics of the 206 cast alloys at high iron contents should be carried out to investigate the effect of the addition of Fe, Mn and Si on the precipitation behavior.